



저작자표시-비영리-변경금지 2.0 대한민국

이용자는 아래의 조건을 따르는 경우에 한하여 자유롭게

- 이 저작물을 복제, 배포, 전송, 전시, 공연 및 방송할 수 있습니다.

다음과 같은 조건을 따라야 합니다:



저작자표시. 귀하는 원저작자를 표시하여야 합니다.



비영리. 귀하는 이 저작물을 영리 목적으로 이용할 수 없습니다.



변경금지. 귀하는 이 저작물을 개작, 변형 또는 가공할 수 없습니다.

- 귀하는, 이 저작물의 재이용이나 배포의 경우, 이 저작물에 적용된 이용허락조건을 명확하게 나타내어야 합니다.
- 저작권자로부터 별도의 허가를 받으면 이러한 조건들은 적용되지 않습니다.

저작권법에 따른 이용자의 권리는 위의 내용에 의하여 영향을 받지 않습니다.

이것은 [이용허락규약\(Legal Code\)](#)을 이해하기 쉽게 요약한 것입니다.

[Disclaimer](#)

Doctoral Thesis

**Self-Consistent Mean Field Theory
for Polymeric Nanomaterials**

So Jung Park

Department of Physics

Graduate School of UNIST

2019

Self-Consistent Mean Field Theory for Polymeric Nanomaterials

So Jung Park

Department of Physics

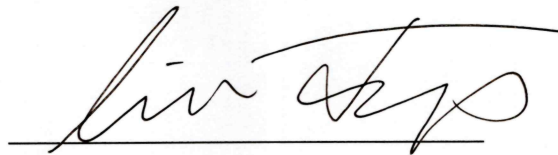
Graduate School of UNIST

Self-Consistent Mean Field Theory for Polymeric Nanomaterials

A thesis
submitted to the Graduate School of UNIST
in partial fulfillment of the
requirements for the degree of
Doctor of Philosophy

So Jung Park

6. 7. 2019
Approved by




Advisor
Jaeup Kim

Self-Consistent Mean Field Theory for Polymeric Nanomaterials

So Jung Park

This certifies that the thesis of So Jung Park is approved.

6. 7. 2019


Thesis Supervisor : Jaeup Kim


Hyuk Kyu Pak : Thesis Committee Member #1


Kyujin Kwak : Thesis Committee Member #2


Chunggi Baig : Thesis Committee Member #3


YongSeok Jho : Thesis Committee Member #4

To Jesus Christ
who died on the cross for me
and was risen from the dead.

Abstract

Polymeric materials have a wide range of scientific and technological applications especially in the field of nanoscience. For example, in the design of well-arranged nanostructures, block copolymers are popular for the control of various material properties because they can phase-separate and self-assemble into periodic structures on nanoscale due to the connectivity and incompatibility of the blocks. In past decades, the major principles of polymer physics have been established, and many theoretical tools investigating the polymeric system have been developed. One of the most successful theoretical tools to describe polymer behavior is self-consistent field theory (SCFT). The theory calculates mean field solutions of polymer statistics under self-consistently determined potential fields, and the phase diagram for self-assembly of block copolymers has been successfully obtained by this tool.

In standard SCFT simulation, it is important to improve numerical algorithms for exploring wide ranges of polymeric systems. When investigating some polymeric systems related with interesting physical problems, there remains the SCFT problems waiting for development of numerical method to accurately solve the target system. On the other hand, there are some cases when standard SCFT is inappropriate to apply because of its fundamental assumption of polymer modeling. While a new group of SCFT method with alternative polymer models has been introduced recently, there are many numerical issues to be solved for practical implementation of this SCFT method due to its limitation in applicability and speed. Regarding those numerical challenges of SCFT, I conducted two independent studies of SCFT, and this thesis consists of two parts.

The first part of this thesis is about two particle interaction in long homopolymer melts [1]. It has been well known that efficient dispersion of the nanoparticles (NPs) in polymer melts is an important factor in yielding high performance nanocomposites. One of the strategies to achieve good dispersion of the NPs is grafting the nanoparticle surface with stretched brush polymers which is chemically identical to the matrix.

According to the scaling analysis made by Leibler, when the matrix homopolymers are relatively short, the free homopolymers penetrate and wet the brush by maximizing the translational entropy. This favorable interaction promotes stable

dispersion of NPs. In contrast, when the matrix chains are relatively long, there is additional entropy loss associated with deep penetration of free homopolymers into the brush. This effect results in aggregation of NPs, and it is well known as autophobic dewetting behavior. Many experimental and theoretical studies confirmed that the entropically driven wetting/dewetting transition is not only dependent on α (the length ratio of free to grafted chains), but also on particle curvature. In addition, it has been reported that autophobic dewetting can be suppressed by using polydisperse grafted chains, which means that higher value of α may be necessary to observe autophobic dewetting phenomenon.

Most theoretical studies about the effect of polydisperse brush on the NP dispersion are limited at a moderate length ratio α less than 4. It is usually hard for most simulation methods to achieve high grafting density of brush and large α at the same time because increase of simulation components results in high computational demand. Because of the problem, no theoretical research has been conducted for the direct comparison of monodisperse and polydisperse brush behaviors especially in completely autophobic dewetting regime with $\alpha = 8$ or beyond.

In order to theoretically investigate the autophobic dewetting phenomenon, I calculate two particle interaction using SCFT with the newly developed numerical scheme, adopting two-dimensional finite volume method (FVM) and multi-coordinate-system (MCS) scheme which makes use of the reflection symmetry between the two NPs. By calculating the polymer density profile and interparticle potential, I identify the effects of parameters such as brush thickness, particle radius, α , brush chain polydispersity, and chain end mobility. It was found that increasing α is the most efficient method for promoting autophobic dewetting phenomenon, and the attraction keeps increasing up to $\alpha = 20$. At small α values, high polydispersity in brush may completely nullify the autophobic dewetting, while at intermediate α values, its effect is still significant in that the interparticle attractions are heavily reduced. The calculation also revealed that the grafting type is not a significant factor affecting the NP aggregation behavior.

The second part of this thesis concerns implementation of discrete chain SCFT for low molecular weight polymers [2]. In recent nanoscience, block copolymers with low molecular weight and high interaction parameter are known as promising material for the creation of nanostructure with domain of sub-10 nm period. In the standard SCFT, however, the most widely used polymer model is the Gaussian chain model in which a long polymer is approximated as an infinitely flexible chain. In the formulation of SCFT, the partition function of polymer chain is calculated by solving a partial differential equation in the form of modified diffusion equation. One of the

limitations of Gaussian chain model is that it is only applicable to long enough polymer chain, and it may produce unphysical results when applied to the calculation of the mean field statistics of short polymer chains.

Recently, the discrete chain SCFT has been suggested as an alternative method. In this formulation, discrete segment chain model is adopted, and the partition functions are obtained through successive integrals calculating the probability distribution. However, the shape of the partition function integral makes the calculation of this method much slower than the standard SCFT when calculated in the real space. Even though the formulation of the discrete chain SCFT has been already established, the numerical implementation of the method is still in the developing stage.

In this study, I implement the pseudo-spectral method for the discrete chain SCFT adopting bead-spring or freely-jointed chain (FJC) model, and a few issues such as the accurate discretization of the FJC bond function are settled in this process. With the adoption of the pseudo-spectral method, the calculation becomes as fast as that of the standard SCFT. The integral equation introduces a new boundary condition, the neutral boundary, which is not available in the standard SCFT solving the differential equation. This interesting physical situation is combined with the finite-range interaction model for the study of symmetric block copolymers within thin films. I find that the surface-perpendicular block copolymer lamellar phase becomes preferable to the surface-parallel one when both the top and bottom surfaces are neutral.

Contents

List of Figures	vi
I Interaction Between Brush-Grafted Nanoparticles in Chemically Identical Homopolymer Melts	1
1 Introduction	2
2 Theory and Numerical Method	8
2.1 SCFT for Two Particle System	8
2.2 Numerical Implementation of MCS	13
3 Result	15
3.1 Brush Morphology of Isolated Particle	15
3.2 Interaction Between Two Particles	22
3.3 Effect of Brush Polydispersity	29
3.4 Effect of Chain End Mobility	33
4 Conclusion	36
II Numerical Implementation of Pseudo-spectral Method in Discrete Chain Self-consistent Mean Field Theory	39
5 Introduction	40
6 Theory of Discrete Chain SCFT	44
6.1 Background	44
6.2 Chain Models	46
6.3 Algebraic Formulation	48
7 Pseudo-spectral Method	55
7.1 Introduction	55
7.2 Implementation in Discrete Chain SCFT	56

8 Numerical Implementation	58
8.1 Bond Function Discretization	58
8.2 Three-dimensional FJC Model	60
8.3 Boundary Condition Issues	64
9 Result	66
9.1 Discrete Chain Behavior in Lamellar Morphology	66
9.2 Diblock Copolymers in Thin Film	70
10 Conclusion	75
Appendix A Mean Field Density and Free Energy of the Two Particle System	78
Appendix B SCFT of End-fixed Brushes	81
Appendix C Contour Plots for Chain End Types	82
Appendix D Recursive Integral Equation of Partition Function	83
Appendix E Total Partition Function and Segment Density in Discrete Chain SCFT	84
Appendix F Calculation of FJC \tilde{g}_i using Sampling Theory of DTFT	86
Appendix G Interfacial Energy Analysis	88
References	89

List of Figures

- Figure 2-1** Schematic diagram of two spherical nanoparticles of radius R covered with end-grafted polymers (red color) in chemically identical homopolymer melts (orange color). The particles (gray color) are separated by a distance D and the plane of reflection symmetry (mirror plane) is drawn by dashed lines. For the implementation of the multi-coordinate-system (MCS) scheme, two spherical coordinate systems, $\mathbf{r} = (r, \theta, \varphi)$ and $\bar{\mathbf{r}} = (\bar{r}, \bar{\theta}, \bar{\varphi})$, centered on particles 1 and 2, respectively, are introduced. Since there is angular symmetry along the azimuthal directions, the third directions are omitted. 8
- Figure 3-1** (a) Segment density profiles of grafted polymers (ϕ_g , solid lines), and free polymers (ϕ_f , dashed lines), and (b) corresponding interfacial width w_I , for a particle with radius $R = 2aN^{1/2}$ at various brush thicknesses H_{brush} . The length of the two types of polymers are the same ($\alpha = 1$). . . 17
- Figure 3-2** (a) Density profiles of grafted (solid lines) and free (dashed lines) polymers for the system of different particle radii $R/aN^{1/2}=1, 2, 4$, and ∞ (flat brush) at fixed brush thickness $H_{\text{brush}} = 2aN^{1/2}$ and $\alpha = 1$. The colored lines are difficult to distinguish because the convergence to the flat brush case is rapid. As seen in the inset, the lines are closely placed in the order of $R/aN^{1/2}=1, 2, 4$, and ∞ . (b) Interfacial width w_I plotted as a function of R . The converging value corresponding to the flat brush case is denoted by a dashed arrow. 19
- Figure 3-3** (a) Density profiles of grafted polymers (ϕ_g , solid lines) and free polymers (ϕ_f , dashed lines) for the standard system geometry with $R = 2aN^{1/2}$ and $H_{\text{brush}} = 2aN^{1/2}$ at α values from 0.2 to infinity. (b) Interfacial width w_I plotted as a function of α in a logarithmic scale. The converging value for the $\alpha \rightarrow \infty$ case is denoted by a dashed arrow. 21

- Figure 3-4** Contour plots of grafted polymer segment density, ϕ_g , of typical (a) wetting ($\alpha = 0.2$) and monodisperse (PDI = 1.00), (b) dewetting ($\alpha = 10$) and monodisperse (PDI = 1.00), and (c) dewetting ($\alpha = 10$) and polydisperse (PDI = 1.40) brushes calculated for two identical particles (gray circles) of radius $R = 2aN^{1/2}$ and brush thickness $H_{\text{brush}} = 2aN^{1/2}$, separated by various interparticle distances D . Ten curvilinear contour lines are drawn at each plot to represent grafted polymer density from 0 (blue) to 0.9 (red). 23
- Figure 3-5** Interaction potential of two monodisperse-brush-grafted particles with radius $R = 2aN^{1/2}$ and brush thickness $H_{\text{brush}} = 2aN^{1/2}$ at various α values, as a function of the normalized interparticle distance D/H_{brush} . The cases of figure 3-4 (a) ($\alpha = 0.2$) and figure 3-4 (b) ($\alpha = 10$) correspond to the black and red lines, respectively. 25
- Figure 3-6** The interaction potential between two monodisperse-brush-coated particles at various brush thicknesses at (a) $\alpha = 4$ and (b) $\alpha = 10$. The case with radius $R = 2aN^{1/2}$ and brush thickness $H_{\text{brush}} = 2aN^{1/2}$ at $\alpha = 10$ is plotted with a thick red line on plot (b). 27
- Figure 3-7** The interaction potential between two monodisperse-brush-coated particles at various particle radii at (a) $\alpha = 4$ and (b) $\alpha = 10$. The case with radius $R = 2aN^{1/2}$ and brush thickness $H_{\text{brush}} = 2aN^{1/2}$ at $\alpha = 10$ is plotted with a thick red line on plot (b). 28
- Figure 3-8** (a) Density profiles of grafted polydisperse polymers (ϕ_g , solid lines) and free homopolymers (ϕ_f , dashed lines) for the system geometry with $R = 2aN^{1/2}$, $H_{\text{brush}} = 2aN^{1/2}$ and $\alpha = 2$ at PDI values from 1.00 to 1.40. (b) The interaction potential between brush-coated particles at PDI values corresponding to (a). (c) and (d) are corresponding plots at $\alpha = 10$ 30
- Figure 3-9** The depth of the potential plotted as a function of PDI at various α values with the system geometry of $R = 2aN^{1/2}$ and $H_{\text{brush}} = 2aN^{1/2}$. . . 31
- Figure 3-10** Contour plots of grafted polymer segment density, ϕ_g , of (a) $\alpha = 4.0$ and monodisperse (PDI = 1.00), and (c) $\alpha = 4.0$ and polydisperse (PDI = 1.40) brushes calculated for two identical particles (gray circles) of radius $R = 2aN^{1/2}$ and brush thickness $H_{\text{brush}} = 2aN^{1/2}$, separated by various interparticle distances D . Ten curvilinear contour lines are drawn at each plot to represent grafted polymer density from 0 (blue) to 0.9 (red). . . . 32

Figure 3-11	(a) Equilibrium grafting density at various interparticle distances, for the case of two end-mobile brush-covered particles with $R = 2aN^{1/2}$, $H_{\text{brush}} = aN^{1/2}$ and $\alpha = 10$. The inset magnifies the grafting density near $\theta = 0$. (b) Interaction potential graph for various system geometries and α values showing the difference of end-mobile (solid line) and end-fixed (dashed line) brushes. The thick solid green line corresponds to the system discussed in (a).	35
Figure 5-1	Example of polymer abstraction and segment modeling of a linear PS chain with n styrene units. Each small blue bead represents one PS monomer. The collection of a few monomer units forms a coarse-grained segment, and the linear polymer chain is modeled by many segments connected by bonds. The coarse-grained segment and bond represent the microscopic degree of freedom of the polymer chain.	41
Figure 6-1	The polymer chain parametrization of the (a) Gaussian chain model, (b) N bond model, and (c) $N - 1$ bond model. For the Gaussian chain model, the curve $\mathbf{r}_\alpha(s)$ is defined at all s in $[0, 1]$, but the function is defined only at discrete points with intervals $\Delta s \equiv 1/N$ and $\Delta s \equiv 1/(N - 1)$ for the cases of N bond model and $N - 1$ bond model, respectively.	44
Figure 6-2	(a) Symmetric ($f = 0.5$) diblock copolymer with N beads and $N - 1$ bonds. (b) Symmetric diblock copolymer with N beads and N bonds.	46
Figure 6-3	(a) Schematic description of the partition function calculation for the positions $1 \rightarrow 2 \rightarrow 3 \rightarrow 4$. At position 3, $s = f$ and the segment type switches from A(blue) to B(red). Description of (b) A evolution and (c) B evolution required for the process of (a). (d) A possible alternative choice, half-A and half-B evolution.	51
Figure 6-4	Problem solving strategy of the discrete chain SCFT adopting $N - 1$ bond model.	53
Figure 8-1	(a) $g_{i,j,0}$ and (b) $g_{i,j,8}$ of the FJC model obtained by Eq. (8.5) for the case of $\Delta x = \Delta y = \Delta z = a/10$. (c) $g_{i,j,0}$ and (d) $g_{i,j,8}$ obtained by Eq. (8.8) after using only $n_x = n_y = n_z = 0$. (e) and (f) are the results with the summation up to $n_x = n_y = n_z = \pm 5$	61
Figure 9-1	(a) Lamellar period D and (b) interfacial width w_I for the discrete chain SCFT of symmetric ($f=0.5$) AB block copolymers with $\chi N = 50$ and 100, as functions of N . The dashed lines are the standard SCFT results using the Gaussian chain model.	67

Figure 9-2 Discrete chain SCFT (a) lamellar period D and (b) interfacial width w_I as functions of χN . The dashed lines are the standard SCFT results using the Gaussian chain model.	69
Figure 9-3 (a) Schematic diagram of freely jointed AB block copolymers confined by the two neutral walls. (b) The free energy comparison between the surface-perpendicular (black lines, \perp) and surface-parallel (colored lines, \parallel) morphologies with n_l periods at $\chi N = 20$, $f = 0.5$, and $N = 20$. Dashed lines are for the N bond model, and real lines are for the $N - 1$ bond model. (c) and (d) are the free energy comparison plot at $N = 100$ and $N = 500$, respectively.	72
Figure 9-4 (a) Schematic diagram of AB block copolymers with BS model. (b) The free energy comparison between the surface-perpendicular (black lines, \perp) and surface-parallel (colored lines, \parallel) morphologies with n_l periods at $\chi N = 20$, $f = 0.5$, and $N = 20$. Dashed lines are for the N bond model, and real lines are for the $N - 1$ bond model. (c) and (d) are the free energy comparison plot at $N = 100$ and $N = 500$, respectively.	73
Figure A.1 Contour plots of grafted polymer segment density, ϕ_g , of (a) end-mobile and (b) end-fixed brushes at various interparticle distances D with the system geometry $R = 2aN^{1/2}$, $H_{\text{brush}} = aN^{1/2}$ and $\alpha = 10$ which corresponds to the green line in figure 3-11 (b).	82
Figure A.2 Interfacial energy plot as a function of segment number N with $N - 1$ bond freely-jointed chain (FJC) model at $\chi N = 50$ (blue solid line in figure 9-1). For a fair comparison between systems with different N , dimensionless interfacial energies per unit area a^2 are plotted. The black line shows the total interfacial tension γ_{total} . The blue line represents γ_{stret} coming from the stretching free energy, and the red line represents γ_{int} coming from the interaction free energy.	88

Part I

**Interaction Between Brush-Grafted
Nanoparticles in Chemically
Identical Homopolymer Melts**

1

Introduction

The addition of nanoparticles (NPs) in polymer templates can create materials with significantly improved mechanical, electrical or optical properties [3–8], and the composite materials have various potential industrial applications such as display panels, photonic crystals, and memory devices with magnetic nanocomposite multilayers [9–11]. Over the past few decades, many theoretical and experimental studies have revealed that microscopic morphology of the constituent NPs strongly influences the macroscopic properties of polymer nanocomposites [12–16], and in particular, efficient dispersion of NPs in polymer matrix has known to be an important factor for the production of high-performance composites [17–21].

However, it is difficult to mix immiscible inorganic NPs in organic polymer melts. Various strategies have been suggested for the control of spatial distribution of nanofillers. One popular method is to functionalize the NP surface with ligands including anionic or cationic oligomeric surfactants, homopolymers and selective copolymers [22–26]. When the NPs are surrounded by homopolymer matrix and the aim is to achieve good dispersion of NPs, it is natural to graft the surface with polymers chemically identical to the matrix.

Even though the chemical similarity between the grafted chains and the matrix makes one to expect an improved miscibility of the fillers within the matrix, it is often observed that the NPs self-assemble into clusters with various shapes [15, 17, 19, 20, 27–34]. For example, Akcora *et al.* has explored the phase behavior of polystyrene-grafted silica NPs in polystyrene (PS) matrix [17]. In their work, the grafting density ($\sigma = 0.01 \sim 0.1$ chains/nm²) was low enough that the core-core attraction of particles competes with the elasticity of the grafted layers, leading to anisotropic structures such as spherical aggregates, sheets and strings. This behavior was also confirmed by an analytical theory and Monte Carlo (MC) simulation.

Such anisotropic structures are formed because the particle cores and grafted polymers are immiscible. Similarly to the case of block copolymer microphase separation, the chain connectivity restricts their phase separation. As a consequence, the polymer chains redistribute on the particle surface, resulting in various shapes of particle aggregates. This type of partial phase separation usually occurs when the grafting density is too low and the grafted chains fail to

wet the surface completely due to insufficient attraction between them. This phenomenon is called allophobic dewetting [35, 36], and in this regime, the incomplete screening between the particle surfaces magnifies the core-core van der Waals attractions. For example, Green and coworkers experimentally demonstrated that particles aggregate due to allophobic dewetting when the matrix chain was longer than the grafted chain and the grafting density σ was below 0.1 chains/nm² [37–39]. Increase of the grafted polymer density removes this partial wetting behavior, and allophobic dewetting disappears for thick layers of grafted polymers. In this wetting regime, the core-core enthalpic attraction is shielded and the miscibility of NPs enhances. They also observed reappearance of the aggregation at high grafting density, which I will explain later.

In addition to the increase of the grafting density, use of the bimodal grafted chains is known to be an effective strategy to suppress allophobic dewetting and achieve good dispersion of NPs. In a series of experiments, Schadler, Benicewicz and coworkers [8, 40, 41] have shown that particles with monomodal grafted chains easily aggregate, but by mixing sparsely grafted long chains with short grafted chains, the interparticle attraction is screened enough to achieve good dispersion of NPs, which greatly improves the thermomechanical property of the nanocomposites. Shi *et al.* observed similar results using dissipative particle dynamics simulation [33]. In their study, various anisotropic self-assembly structures of grafted NPs are found when the grafted chain length and grafting density are moderate, and bimodal grafted chain layer produces better wetting surface favoring enhanced dispersion of NPs in the matrix.

When the density of grafted chains is high enough ($\sigma N^{1/2} > 1$), where σ is the dimensionless grafting density and N is the degree of polymerization of the chain, the grafted polymers stretch outwards and form a brush. In this regime, the brushes completely wet the particle surface and the NP core-core interaction is strongly screened. As a consequence, the dispersion characteristics of NPs mainly depend on the entropic effects of the polymers, and the system experiences another well known wetting/dewetting transition which strongly depends on α , the length ratio of free to grafted chains. When the melt homopolymers are shorter than the grafted polymers, there exists a regime that the free homopolymers easily penetrate and wet the brush in order to maximize the translational entropy. This effect creates attractive interaction between the melt chains and the brush so that stable dispersion of NPs becomes favorable. On the other hand, when the matrix chains are relatively long, deep penetration of free homopolymers into the brush costs conformational entropy loss, and the free chains are expelled from the brush. This behavior is well understood in many theoretical and experimental studies, and it is referred to as autophobic dewetting [35, 36, 42–45]. This phenomenon creates an unfavorable interaction between the brush and matrix, and it may be responsible for the aggregation of NPs observed in many experiments, though the distinction between allophobic and autophobic dewetting is not a trivial task.

According to the scaling analysis by Leibler and coworkers [42], transition from wetting to autophobic dewetting on stretched flat brushes ($\sigma N^{1/2} > 1$) occurs when $\alpha > \sigma^{-1/2} N^{-1/4}$. Even though many theorists and experimentalists present this scaling relation as the guide of the dewetting transition, quantitative calculation by Matsen and Gardiner [43] using self-consistent field theory (SCFT) suggests that somewhat higher α is necessary to observe a meaningful level of autophobic dewetting on a flat brush. For the practical parameters they tested, finite amount of surface tension between the brush and homopolymers becomes observable only when α is 1 or above.

Note that these theoretical predictions are valid for flat brushes, and it is natural to expect some deviations when they are applied to curvilinear systems such as spherical NPs and cylindrical nanofillers. Many experimental and theoretical studies confirmed that autophobic dewetting is dependent on both the grafting density and particle curvature [46–48], and it has been suggested that the onset α for the aggregation of spherical NPs is somewhat higher than 1 [29], especially when the NP size is small. For example, Kim and Green studied nanocomposites of PS homopolymers and PS brush-coated spherical Au NPs with 2.4 nm of approximate core radius [49]. In their work, the spatial distribution of NPs in thin film nanocomposites was controllable by the variation of α . At α below 3, they found well-mixed nanocomposites, and transition from miscibility to immiscibility occurred in the range $3 < \alpha < 8$. At high enough α , preferential NP segregation to the interfaces initiated structural instability. A similar trend was found in other researches using spherical NPs. The aggregation transition was observed at $\alpha = 5 \sim 6$ in the experiment by Archer’s group with NPs of radius ~ 5 nm [48], and slightly different onset value, $\alpha = 4$, was observed in an experiment by Chevigny *et al.* with NPs of ~ 13.4 nm radius [50].

Similar experimental and theoretical researches using cylinder-shaped nanorods suggested that the boundary between aggregated and dispersed states is around $\alpha = 1.5 \sim 2$, which is somewhat below the onset of the spherical particle aggregation, but it is still above the prediction using flat brushes [51–53]. In a theoretical research using density functional theory, Frischknecht investigated the interaction between two aligned polymer-coated nanorods in melts of the same polymers [51]. She found that weak attractive interaction due to autophobic dewetting becomes visible at $\alpha = 1.5$, and the depth of the attractive well becomes deeper at increasing α .

These observations can be explained by the fact that chains are more densely distributed on flatter surfaces compared to the curvilinear surfaces. As the curvature of the surface increases, the free ends of grafted chains acquire more space to explore, which promotes the interpenetration of matrix chains into the brush [48, 54, 55]. As a result, autophobic dewetting is lessened at $\alpha \gtrsim 1$ and a high miscibility of the fillers can be found beyond the boundary predicted by flat brush theories. In spite of such differences, all the aforementioned systems claim that as long as brushes are well-stretched, the autophobic dewetting eventually becomes dominant and nanofillers aggregate at high enough α values.

I earlier explained the possible use of bimodal grafted chains for the suppression of allophobic dewetting. Bidisperse brushes can also be adopted to suppress autophobic dewetting. In an SCFT research by Matsen's group [56], it was shown that highly bidisperse flat brush can significantly broaden the brush/homopolymer interface even at very large α , which results in the reduction of the autophobic dewetting and effective surface tension. Applying this idea to the curvilinear surfaces, it is expected that bidisperse brush on NP surface can suppress autophobic dewetting, and the clumping of NPs are delayed at intermediate values of α where monodisperse brush results in aggregated phase.

Note that large α value is not the sufficient condition to observe the autophobic dewetting. The chains must also be densely grafted to avoid allophobic dewetting, and for most experiments using bimodal brushes, the grafting density is too low ($\sigma N^{1/2} < 1$) or at most at the borderline of the allophobic dewetting so that the two types of brushes are just enough to screen the NP core-core attraction. There exist a few theoretical studies conducted about the effect of polydispersity on the NP dispersion, in which the brushes are grafted densely enough to observe entropically driven wetting/dewetting transition and NP aggregation. Using Polymer Reference Interaction Site Model-MC simulation, Jayaraman and coworkers confirmed that polydisperse brush is more effective for NP dispersion compared to the monodisperse brush [57, 58]. They assumed athermal interaction to mimic experimental systems with negligible core-core interaction, and the effective interaction between two NPs was calculated as a function of brush polydispersity. The simulation was conducted up to $\alpha = 4$, and weak attractive well of $\sim 0.1k_B T$ observed for monodisperse system disappeared at polydispersity index (PDI) over 1.5, and purely repulsive interaction remained.

Even though the above result indicates that the effect of the polydisperse brush is significant enough to nullify the interparticle attraction due to autophobic dewetting at a moderate length ratio α , the extent to which the polydispersity affects the nature of the interaction is poorly understood for a wide range of α . Most simulation methods have trouble achieving high σ and large α at the same time due to high computational demand associated with the increase of simulation components; thus it remains as an open question if NP dispersion can always be achieved by means of polydispersity under the condition that NPs would otherwise be aggregated by autophobic dewetting. As far as I know, no systematic theoretical test has been conducted for the direct comparison of polydisperse and monodisperse brush behaviors in completely autophobic dewetting regime with $\alpha = 8$ or beyond. As mentioned earlier, particles with high curvature have a tendency to move the dewetting boundary towards larger α , which provides another reason to make an intense study on this large α regime. This subject also has an industrial importance because some functional hybrid materials require high molecular weight matrix polymer for achieving sufficient mechanical integrity, while dispersion of NPs are still preferable.

My interest is especially on the investigation of the stabilization mechanism of NPs in the long homopolymer matrix with α up to 20 where autophobic dewetting is supposed to be significant. In this part of thesis, the systems are limited to densely grafted brushes ($\sigma N^{1/2} > 1$) to ensure that the system is not in the allophobic regime and the interparticle interaction and phase transition are determined purely by entropic effect. One major theoretical tool for this subject is the SCFT which provides an accurate mean field solution of the polymer nanocomposite system [22, 46, 47, 54, 59–61]. Increase of grafting density and grafted chain length is a relatively easy task in SCFT, but achieving large α can still be an issue in the actual implementation of the SCFT in a finite size of system.

For the numerical SCFT analysis of an isolated polymer-grafted particle, the spherical coordinate system may be useful, but difficulties arise when focuses are on the interaction between two polymer-grafted NPs. One possible choice is to use the cylindrical coordinate system with its z axis on the line connecting the two particles and impose boundary conditions to make the partition functions vanish inside the particles [46]. However, the cylindrical coordinate system inevitably hosts cylinder-shaped grids which do not follow the surface of spherical NPs, and one cannot avoid adopting variable distances from the grafting points to the particle surface. Considering that logarithm of this small distance influences the free energy of the system, [62] the cylindrical coordinate system is not ideal for the accurate calculation of this type of problem, especially when one wants to identify subtle free energy differences.

A more sophisticated approach is to use the bispherical coordinate system following the geometry of two particles [47, 63]. Trombly and Ganesan investigated the interaction between brush-grafted particles immersed in chemically identical homopolymer melts by solving SCFT equations in bispherical coordinates [47]. The interpenetration width between the melt and brush chains [64, 65] was one of their major subjects. They calculated it as a function of α to determine the onset of wetting and dewetting transitions. In their study with α up to 4, the attraction between two particles started to emerge with increasing α , and the depth of attractive interparticle potential was quantitatively correlated with the interpenetration width.

The bispherical coordinate system allows one to use Neumann boundary on the particle surfaces, and the grafting points can be positioned on spherically shaped grids. However, the intrinsic complexity of the coordinate system makes it difficult to perform fast and accurate numerical calculations. In addition, the prefactor of the delta function initial conditions required for the control of the grafted polymer density now has subtle angular and interparticle distance dependences, which adds difficulty in the free energy calculation with higher precision.

Due to the aforementioned problems, even though there exist experimental works on NPs mixed with high molecular weight polymers, quantitative theoretical research for such long polymer chains has not been available. Multi-coordinate-system (MCS) scheme using two spherical coordinate systems each centered on one particle is one attractive suggestion to overcome these problems and perform fast and accurate SCFT calculations [60]. In the previously developed

MCS scheme, each polymer must be associated with one coordinate system, and thus it is not applicable to the current problem with freely floating matrix chains. In the current work, by upgrading the MCS scheme to handle the partition function calculation of the matrix chains, a numerical method to solve the aforementioned problems has been successfully established. For the spatial discretization, I adopt a finite volume method (FVM) for both numerical efficiency and mass preservation [66]. Such a combination allows exploring a very wide range of parameters while keeping high numerical accuracy.

In this part of thesis, I investigate the interaction between two polymer-grafted particles in chemically identical homopolymer melts through SCFT theory. In chapter 2, I introduce the theory and numerical method for analyzing the two particle system. The results obtained by performing accurate SCFT calculation adopting MCS and FVM are provided in the following chapter. Finally, I conclude with a brief summary in chapter 4.

2

Theory and Numerical Method

2.1 SCFT for Two Particle System

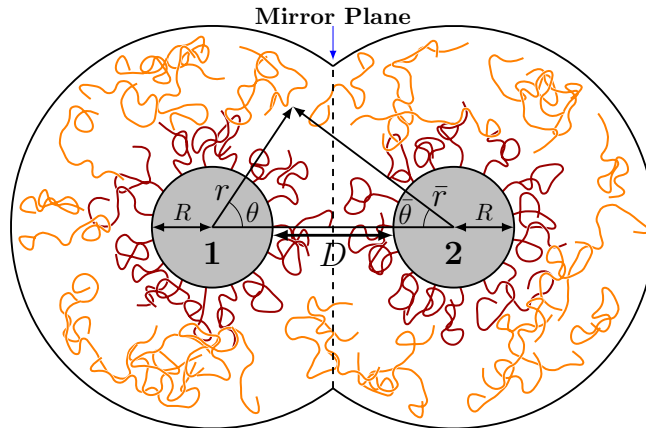


Figure 2-1: Schematic diagram of two spherical nanoparticles of radius R covered with end-grafted polymers (red color) in chemically identical homopolymer melts (orange color). The particles (gray color) are separated by a distance D and the plane of reflection symmetry (mirror plane) is drawn by dashed lines. For the implementation of the multi-coordinate-system (MCS) scheme, two spherical coordinate systems, $\mathbf{r} = (r, \theta, \varphi)$ and $\bar{\mathbf{r}} = (\bar{r}, \bar{\theta}, \bar{\varphi})$, centered on particles 1 and 2, respectively, are introduced. Since there is angular symmetry along the azimuthal directions, the third directions are omitted.

I first concentrate on two particle problem because such an approach can provide a simple but efficient analysis of the interparticle interaction. It is natural to assume that the three-body or higher order interaction is important only when the particle density is very high. In this model, I consider a system of two identical spherical particles each covered with $n_g/2$ end-grafted polymers of polymerization index N , and the interparticle distance is D as defined in figure 2-1. The two particles are surrounded by n_f homopolymers each with length αN , and they are chemically identical to the grafted polymers. The polymers are in an incompressible melt state so that the system volume is the total volume occupied by the polymers, $V = (n_g + \alpha n_f)N/\rho_0$, where ρ_0^{-1} is the volume of each segment. Later $V_g \equiv n_g N/\rho_0$ and $V_f \equiv \alpha n_f N/\rho_0$ will be used

as the grafted and free chain volumes, respectively.

When describing one particle system, it is natural to use the spherical coordinate system. However, for the case of the two particle system, there should be special considerations in choosing an appropriate coordinate system describing both particles equally. Especially, for the brush system with delta function initial condition at the grafting points, it is extremely important to position the discretized grid points on the grafting surface at the system boundary or at a constant distance away from it [60]. As mentioned in the introduction chapter 1, one attractive choice is the bispherical coordinates [47, 63] whose spherically positioned grid points can fit on the curved grafting surfaces of both particles. However, such a non-traditional choice of the coordinate system is penalized by high computational demand, and thus simulations in extreme conditions such as large particles, thick brushes, and long polymers are difficult to perform. As explained in the introduction chapter, it is necessary to study such limiting cases for the full understanding of the interparticle interaction, and it is especially important to perform simulations at $\alpha > 10$.

In this research, I upgrade the multi-coordinate-system (MCS) scheme which was introduced by Kim and Matsen [22, 60]. It has been successful in achieving both accuracy and speed for the polymeric systems with multiple core parts. In this approach, two spherical coordinate systems, $\mathbf{r} = (r, \theta, \varphi)$ and $\bar{\mathbf{r}} = (\bar{r}, \bar{\theta}, \bar{\varphi})$, whose origins locate at the center of each particle are used (see figure 2-1). The angles are chosen such that $\theta = 0$ line points towards the center of particle 2, and $\bar{\theta} = 0$ line points towards the center of particle 1. Since there is an angular symmetry along the φ and $\bar{\varphi}$ directions, the full analysis can be reduced to two-dimensional calculation, which is very important for fast calculation.

In order to model impenetrability of particles, reflecting boundaries are used on the surfaces of the two particles, $r = R$ and $\bar{r} = R$. Because the particles are surrounded by homopolymer melts, there is no officially accepted outer boundary. For accurate modeling, peanut-shaped domain (see figure 2-1) is used which is large enough that physical properties at the outer boundary converge to those of homopolymer melts at infinity, and reflecting boundary is imposed there. From now on, the SCFT formalism for the polymer melts in this peanut-shaped region is described. MCS in the peanut-shaped region surrounded by solvents has been reported earlier [60], but the current system includes freely floating matrix polymers which do not belong to a certain spherical coordinate system. In this and the next sections, I will explain how the MCS is upgraded to properly calculate the free chain partition function.

All the polymers in the system are modeled as infinitely flexible Gaussian chains with statistical segment length a . The conformation of the i 'th grafted polymer is described by a space curve $\mathbf{r}_{g,i}(s)$ with continuous parameter $s \in [0, 1]$ increasing from the free end ($s = 0$) to the grafted end ($s = 1$). Space curves $\mathbf{r}_{f,j}(s)$ are used for the description of free homopolymer chains with j from 1 to n_f . Be careful that the length of each free chain is αN , making $s \in [0, \alpha]$ the correct range for the free chains.

2.1 SCFT for Two Particle System

For each grafted chain conformation, $\mathbf{r}_{g,i}(s)$, an unnormalized probability function representing its internal entropy loss can be assigned as follows:

$$P[\mathbf{r}_{g,i}(s)] \equiv \exp\left(-\frac{3}{2a^2N} \int_0^1 ds |\mathbf{r}'_{g,i}(s)|^2\right) \quad (2.1)$$

Similar functions can be assigned to the free polymer conformations, $\mathbf{r}_{f,j}(s)$, just by modifying the upper limit to α in the integration. Using these expressions, the canonical partition function of the system can be formally written as the following equation,

$$Z \propto \frac{1}{n_g!n_f!} \int \prod_{i=1}^{n_g} \mathcal{D}\mathbf{r}_{g,i} P[\mathbf{r}_{g,i}] \prod_{j=1}^{n_f} \mathcal{D}\mathbf{r}_{f,j} P[\mathbf{r}_{f,j}] \\ \times (\delta(r_{g,i}(1) - R) + \delta(\bar{r}_{g,i}(1) - R)) \delta[1 - \hat{\phi}_g(\mathbf{r}) - \hat{\phi}_f(\mathbf{r})] \quad (2.2)$$

where factorial factors are introduced to represent indistinguishability of n_g grafted chains and n_f free chains, and all possible conformations of the polymer chains are counted by the functional integrals. The first two delta functions restrict the grafted chain ends on the surfaces of the two particles with radius R . Note that the ends are in fact mobile on the two particle surfaces with this formulation. Incompressibility condition for the polymer melts is represented by the last delta function where $\hat{\phi}_g(\mathbf{r})$ and $\hat{\phi}_f(\mathbf{r})$ are the densities of grafted and free chains, respectively, and they are given by

$$\hat{\phi}_g(\mathbf{r}) = \frac{N}{\rho_0} \sum_{i=1}^{n_g} \int_0^1 ds \delta(\mathbf{r} - \mathbf{r}_{g,i}(s)) \quad (2.3)$$

$$\hat{\phi}_f(\mathbf{r}) = \frac{N}{\rho_0} \sum_{j=1}^{n_f} \int_0^\alpha ds \delta(\mathbf{r} - \mathbf{r}_{f,j}(s)) \quad (2.4)$$

Using Hubbard-Stratonovich transformation, segment-position-dependent terms can be replaced by fields, W_g , W_f and Φ_f , so that the original segment-position-based equation (2.2) is now transformed into a field-based equation,

$$Z \propto \int \mathcal{D}W_g \mathcal{D}W_f \mathcal{D}\Phi_f \exp\left(-\frac{F[W_g, W_f, \Phi_f]}{k_B T}\right) \quad (2.5)$$

where k_B is the Boltzmann factor and T is the system temperature. A detailed discussion of F and its relation with each field term are provided in appendix A. In the standard SCFT approach, after applying the saddle-point approximation, F becomes the mean field free energy,

$$\frac{F}{k_B T} = n_g \ln\left(\frac{V_g}{Q_g[w_g]}\right) + n_f \ln\left(\frac{V_f}{Q_f[w_f]}\right) \\ - \frac{\rho_0}{N} \int d\mathbf{r} (w_g(\mathbf{r})\phi_g(\mathbf{r}) + w_f(\mathbf{r})\phi_f(\mathbf{r})) \quad (2.6)$$

where Q_g and Q_f are total partition functions which will be explained later, and $w_g(\mathbf{r})$ and

2.1 SCFT for Two Particle System

$w_f(\mathbf{r})$ are interaction potentials acting on the segments of grafted and free chains positioned at \mathbf{r} , respectively. Also, $\phi_g = \langle \hat{\phi}_g \rangle$ and $\phi_f = \langle \hat{\phi}_f \rangle$ are the ensemble average segment densities at the mean field solution. Note that there are some issues regarding the zero point of the free energy. I choose this shape of free energy which converges to a certain finite number as the system size diverges by adding infinitely many free chains. With this choice of free energy, direct comparison of energies between systems with various interparticle distances becomes meaningful.

Mean fields $w_g(\mathbf{r})$ and $w_f(\mathbf{r})$ become the same in the mean field theory, and thus subscripts will be omitted from now on. For the calculation of the segment concentrations and free energy, the single chain partition functions $Q_\kappa[w]$ for both grafted polymer ($\kappa = g$) and free polymer ($\kappa = f$) subjected to the mean field potential $w(\mathbf{r})$ are required. In the actual SCFT calculation, it is obtained by

$$Q_\kappa[w] = \int d\mathbf{r} q_\kappa(\mathbf{r}, s) q_\kappa^\dagger(\mathbf{r}, s) \quad (2.7)$$

where $q_g(\mathbf{r}, s)$ is defined as the partial partition function of the sN segments of grafted chains whose first segment is free and the last segment position is fixed at \mathbf{r} . For the $(1-s)N$ segments starting from the grafted end, the conjugate partial partition function is defined as $q_g^\dagger(\mathbf{r}, s)$. Similar definitions are used for the partial partition functions of the free polymer except that the total chain length is now changed to αN . Under the given mean field potential $w(\mathbf{r})$, the partial partition functions $q_\kappa(\mathbf{r}, s)$ are known to satisfy the following modified diffusion equation,

$$\frac{\partial}{\partial s} q_\kappa(\mathbf{r}, s) = \left(\frac{a^2 N}{6} \nabla^2 - w(\mathbf{r}) \right) q_\kappa(\mathbf{r}, s) \quad (2.8)$$

and $q_\kappa^\dagger(\mathbf{r}, s)$ also satisfy similar modified diffusion equation obtained by multiplying the left-hand side of Eq. (2.8) by -1 . For the case of the grafted polymers, initial conditions corresponding to the free ends ($s = 0$) and ends grafted on the two particle surfaces ($s = 1$) are,

$$q_g(\mathbf{r}, 0) = 1 \quad (2.9)$$

$$q_g^\dagger(\mathbf{r}, 1) = \delta(r - R) a N^{1/2} + \delta(\bar{r} - R) a N^{1/2} \quad (2.10)$$

respectively, while for the homopolymers,

$$q_f(\mathbf{r}, 0) = q_f^\dagger(\mathbf{r}, \alpha) = 1 \quad (2.11)$$

because both ends are free to move in the system. Note that one homopolymer end is at $s = \alpha$, not at $s = 1$. The numerical evaluation of the partition functions using MCS scheme will be explained in the next section.

In order to obtain the complete mean field solution, the calculation of the segment densities, $\phi_g(\mathbf{r})$ and $\phi_f(\mathbf{r})$, is required. In SCFT, minimizing the exponent in Eq. (2.5) with respect to field

2.1 SCFT for Two Particle System

variables W_g and W_f by functional derivative leads to the following self-consistency equation,

$$\phi_g(\mathbf{r}) + \phi_f(\mathbf{r}) = 1 \quad (2.12)$$

where ϕ_g and ϕ_f are obtained by (see appendix A for proof)

$$\phi_g(\mathbf{r}) = \frac{V_g}{Q_g} \int_0^1 ds q_g(\mathbf{r}, s) q_g^\dagger(\mathbf{r}, s) \quad (2.13)$$

$$\phi_f(\mathbf{r}) = \frac{V_f}{\alpha Q_f} \int_0^\alpha ds q_f(\mathbf{r}, s) q_f^\dagger(\mathbf{r}, s) \quad (2.14)$$

Once the field $w(\mathbf{r})$ is given, the partition functions are obtained by Eqs. (2.7) and (2.8), and the segment densities can be calculated by Eqs. (2.13) and (2.14). However, there is no guarantee that the self-consistency equation (2.12) is satisfied for the arbitrarily given $w(\mathbf{r})$. The mean field potential must be determined self-consistently to satisfy Eq. (2.12) which enforces incompressibility for the polymer melt system.

In most SCFT calculations, the adjustment is performed by an iteration method. For each iteration, output field is created by adding $\Lambda (\phi_g(\mathbf{r}) + \phi_f(\mathbf{r}) - 1)$ to the trial input field, where Λ is a constant. The input and output fields are mixed to create a new trial field, and the iteration continues until the field converges. In this calculation, $\Lambda = 5.0$ is used and to speed up the convergence, Anderson mixing [67–69] is often used when the field convergence error defined by $\left(\int d\mathbf{r} (w^{\text{out}} - w^{\text{in}})^2 / \int d\mathbf{r} (w^{\text{in}})^2 \right)^{1/2}$ is about 0.05. The iteration stops when the field convergence error is below 10^{-10} .

After finding the self-consistent solution, I calculate $F(D)$, the free energy of the two particle system with interparticle distance D , using Eq. (2.6). The difference of the free energy with respect to the case $D = \infty$ is the effective interaction potential $U(D)$ between the two particles,

$$U(D) = F(D) - F(\infty) \quad (2.15)$$

2.2 Numerical Implementation of MCS

By taking advantage of the reflection symmetry of the two particle system, the computational demand for numerical calculations can be reduced using MCS scheme to be explained in this section. Lets first consider the calculation of the grafted polymer density. Total grafted polymer density is the sum of the contributions from the first particle, $\phi_{g1}(\mathbf{r})$, and the second particle, $\phi_{g2}(\mathbf{r})$. The reflection symmetry makes it possible to obtain both functions in one calculation; once $\phi_{g1}(\mathbf{r})$ is calculated for the entire space, $\phi_{g2}(\mathbf{r})$ can be simultaneously obtained by the following equation,

$$\phi_{g2}(\mathbf{r}) = \phi_{g1}(\bar{\mathbf{r}}) \quad (2.16)$$

where the coordinate $\bar{\mathbf{r}} = (\bar{r}, \bar{\theta}, \bar{\varphi})$ can be calculated from \mathbf{r} by the following transformation equation,

$$\bar{r} = \sqrt{r^2 + (2R + D)^2 - 2r(2R + D) \cos \theta} \quad (2.17)$$

$$\bar{\theta} = \tan^{-1} \left(\frac{r \sin \theta}{2R + D - r \cos \theta} \right) \quad (2.18)$$

$$\bar{\varphi} = \varphi \quad (2.19)$$

For the calculation of $\phi_{g1}(\mathbf{r})$, it is required to calculate the partial partition functions of the grafted chains pertaining to particle one with the initial conditions $q_{g1}(\mathbf{r}, 0) = 1$ and $q_{g1}^\dagger(\mathbf{r}, 1) = \delta(r - R)aN^{1/2}$. The segment density is calculated by

$$\phi_{g1}(\mathbf{r}) = \frac{V_{g1}}{Q_{g1}} \int_0^1 ds q_{g1}(\mathbf{r}, s) q_{g1}^\dagger(\mathbf{r}, s) \quad (2.20)$$

where $V_{g1} = V_g/2$, since only half of the grafted polymers belong to the first particle. The partition function for the polymers grafted to particle one, Q_{g1} , can be easily obtained by using Eq. (2.7), and it is exactly half of the total partition function Q_g defined for polymers grafted to both particles. Because of this, V_{g1} and Q_{g1} can replace V_g and Q_g in most places, respectively, considering that their ratio is usually used. After calculating ϕ_{g1} for the entire space, the total grafted polymer density ϕ_g can be easily calculated by just obtaining ϕ_{g2} using Eqs. (2.16) and $\phi_g = \phi_{g1} + \phi_{g2}$. Note that in principle the entire space must be considered, but ϕ_{g1} far away from the surface of particle one must vanish, and thus q_{g1} and q_{g1}^\dagger are calculated only in the first spherical coordinate system.

On the other hand, the density of free polymers in the entire peanut-shaped space is obtained in a slightly different way, because free polymers do not formally belong to a specific particle, and this is the crucial difference from the earlier MCS scheme developed for brushes in solvents [60]. After simply setting $q_f(\mathbf{r}, 0) = q_f^\dagger(\mathbf{r}, \alpha) = 1$, the diffusion equations are solved in the first spherical coordinate system. Such a method will at least provide accurate partial partition functions and free polymer density at the left-hand side of the mirror plane, and it is possible

to calculate the segment density in that region using Eq. (2.14). Note that the total partition function for the free polymers, Q_f , is calculated by performing the integration in Eq. (2.7) only at the left-hand side of the mirror plane and multiplying the result by two, considering the reflection symmetry. The free chain density at the right-hand side of the mirror plane is also obtained by the reflection of the density profile.

In the actual implementation of MCS SCFT, I perform the numerical calculation using grid points discretized within the spherical coordinate system. The SCFT calculation is conducted by adopting a fine mesh as explained below. For the spherical coordinate system pertaining to particle one, grids are regularly spaced by $\Delta\theta = 0.01\pi$ from $\theta = 0$ to π and $\Delta r = 0.04aN^{1/2}$ from $r = R$ to $r = R_{\max}$. The outer boundary value, R_{\max} , is chosen to be $5R$ at small α , but larger values of R_{\max} are necessary when the free polymers are long. At $\alpha = 10$, I use $R_{\max} = 7R$ and sometimes $R_{\max} = 9R$ is used at the highest α values. Equivalent meshes are used for the coordinate system $\bar{\mathbf{r}}$ centered on particle two. When reflecting density or field between the two coordinate systems, there are nontrivial issues regarding the coordinate transformation using Eqs. (2.17)–(2.19), because the reflected points are usually located in between grid points of the other coordinate system. I carefully handle this problem by using linear interpolation of the function values at nearest neighbors as suggested in ref. [60].

In order to solve the diffusion equation (2.8), I apply Crank-Nicolson algorithm for differentiation in the s direction with $\Delta s = 0.005$. To reduce the computation time and improve the stability of calculation, modified Douglas-Gunn alternating-direction implicit (ADI) method [66, 69–72] is adopted. For the approximation of the spatial differentiation in the spherical coordinate system, finite difference method (FDM) is a simple choice. I instead adopt the finite volume method (FVM) [66, 73] which is based on the idea of flux conservation, and it provides an additional advantage of reducing the material conservation error especially when curvilinear coordinate system is adopted. The implementation of FVM requires an additional consideration for the determination of numerical coefficients, which is a one-time upgrade from FDM after the required equations are derived [66]. As is customary for the FVM, volume integral is evaluated by weighting integrand with each cell volume, while for the integration over cells divided by the mirror plane, each integrand is weighted with the cell volume cut off by the mirror plane.

With the combination of FVM and ADI, I manage to make a fast and accurate SCFT calculation. In one example, for the system with $H = 2aN^{1/2}$, $R = 2aN^{1/2}$, $R_{\max} = 14aN^{1/2}$ and $\alpha = 10$, I use a spatial grid of 300×100 and $\Delta s = 0.005$. The calculation usually takes less than a second per iteration when using 12 cores of Xeon Gold 6132 CPUs and OpenMP library. When α is large, thousands of iterations are necessary for the accurate solution even with the adoption of Anderson mixing; for the given parameter set, it takes approximately 25 minutes to finish the whole calculation.

3

Result

For the preparation of the two-particle system analysis, I first perform various tests identifying wetting and dewetting regimes of the single particle system, which is presented in section 3.1. In the following sections, I study the interaction between two particles immersed in chemically identical homopolymer melts, and I theoretically investigate the effects of parameters such as particle radius, brush thickness, molecular weight ratio of free to grafted polymers, brush chain polydispersity and brush grafting types.

3.1 Brush Morphology of Isolated Particle

For the preparation of the study of the two-particle interaction, I present the analysis of an isolated particle system (i.e., $D \rightarrow \infty$) in this section. When there is no chemical distinction between the polymer chains, the interaction between two particles purely originates from entropic contributions of the polymer chains. There are two main entropic contributions; one is the conformational entropy of brush polymers and the other is the translational entropy of free polymers. Competition between these two types of entropic effects determines the morphology of the system. I begin the analysis by examining the segment density profile, and my focus is on how parameters such as particle radius R , brush thickness H_{brush} and chain length ratio α affect the properties of the interface between the brush and the free chains.

3.1 Brush Morphology of Isolated Particle

In figure 3-1 (a), I display density profiles of the grafted and free polymers on an isolated particle of radius $R = 2aN^{1/2}$ at various H_{brush} values. The brush height, H_{brush} , is defined as the thickness of the brush layer in the absence of the free polymer penetration. Sparsely grafted brush is represented by a small H_{brush} , and its value increases as the grafting density increases. In order to focus on the geometrical effect, I fix $\alpha = 1$ for this and the next figure. As shown in figure 3-1 (a), at increasing r , the brush-rich phase changes to the free polymer-rich phase, and the interface locates around $r = R + H_{\text{brush}}$ as expected. In order to quantify the degree of polymer interpenetration, I define the interfacial width as

$$w_I = -\frac{\phi_g(0)}{\phi'_g(r_{1/2})} \quad (3.1)$$

which is the brush density at the grafting surface, $\phi_g(0)$, divided by minus of the slope at $r_{1/2}$ where the brush density is $\phi_g(0)/2$ [64, 65, 74].

Interfacial widths corresponding to the cases of figure 3-1 (a) are shown in figure 3-1 (b). For the thinnest brush case, at $H_{\text{brush}}/aN^{1/2} = 1$, the density profile of grafted polymers exhibits a slow decay over a relatively long radial distance from the particle surface. As the brush becomes thicker, the density slope becomes steeper and the interfacial width decreases. For the case of the very thick brush ($H_{\text{brush}}/aN^{1/2} = 10$), the interpenetration region becomes considerably narrow.

In general, it is advantageous for the free chains to penetrate into the brush to increase their translational entropy, and such behaviors are observed for spherical wet brushes [60]. For the case of polymer melt system, however, significant stretching entropy cost is imposed when the free chain penetration depth is comparable to the brush thickness, and the balance between these two effects determines the interfacial width. When the brush is sparsely grafted, and its thickness is comparable to $aN^{1/2}$, free polymers can penetrate into the sparsely grafted brush in order to maximize the translational entropy of both types of polymers, and the resulting interfacial width becomes large. On the other hand, for a thick brush with a high grafting density, it is difficult for free polymers to penetrate into the highly stretched brush, and thus free polymers are expelled to reduce the conformational entropy cost, which results in a narrow interfacial width.

3.1 Brush Morphology of Isolated Particle

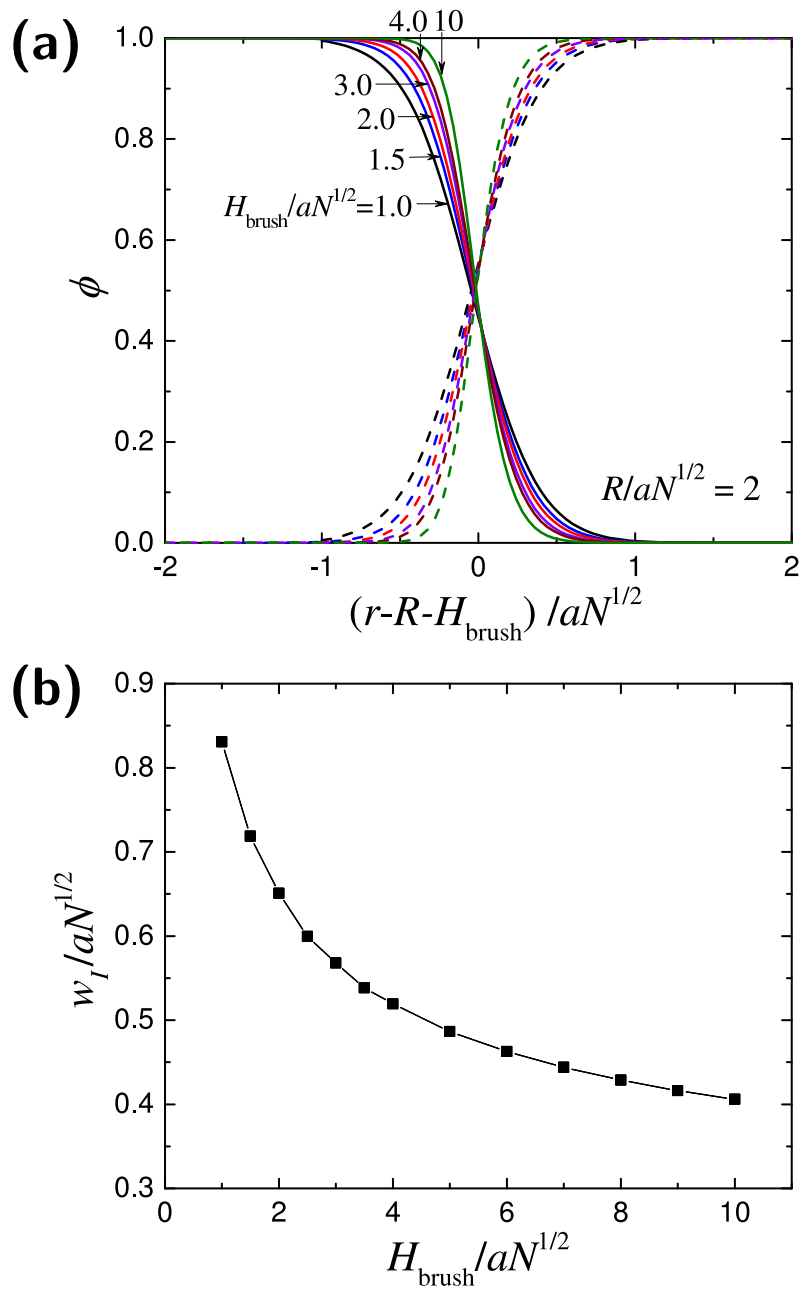


Figure 3-1: (a) Segment density profiles of grafted polymers (ϕ_g , solid lines), and free polymers (ϕ_f , dashed lines), and (b) corresponding interfacial width w_I , for a particle with radius $R = 2aN^{1/2}$ at various brush thicknesses H_{brush} . The length of the two types of polymers are the same ($\alpha = 1$).

3.1 Brush Morphology of Isolated Particle

Figure 3-2 exhibits similar plots to those of figure 3-1, but for different particle radii at fixed brush thickness $H_{\text{brush}} = 2aN^{1/2}$. It shows that unless the particle is extremely small, the effect of the particle size, or curvature, is not significant, as shown from density profiles and interfacial width. I expect that brushes on smaller particles behave as if the effective brush thickness is smaller than its actual value because, at fixed brush thickness, systems with higher curvature (or small particle size) provide extra space for grafted polymers to swell. It means smaller particles have more rooms to reduce the stretching entropy cost of the grafted chains when penetration of free chains occurs. As a consequence, the interfacial width must increase as the particle size decreases. Even though figure 3-2 (b) exhibits such a trend, the particle size must be extremely small ($R < aN^{1/2}$) in order to observe a significant effect. At reasonable R values, the difference is very difficult to observe, and the convergence to the flat brush case ($R = \infty$) is very rapid.

3.1 Brush Morphology of Isolated Particle

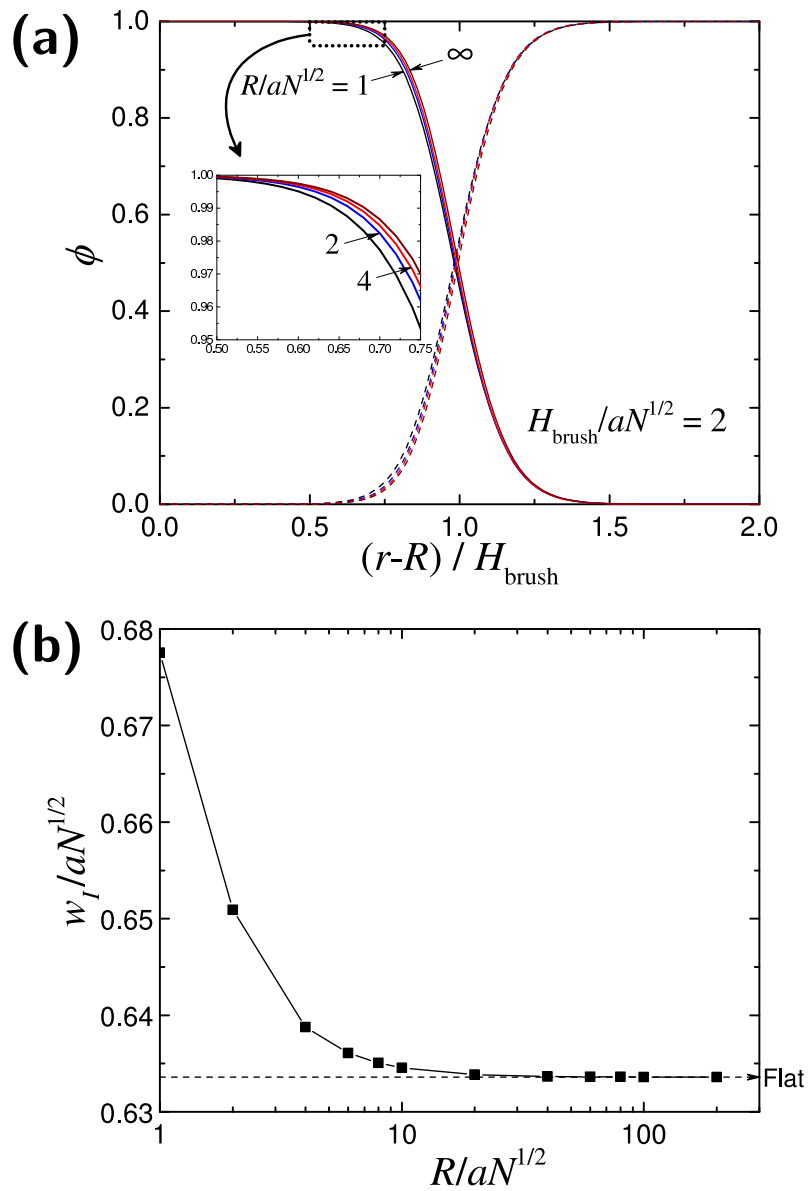


Figure 3-2: (a) Density profiles of grafted (solid lines) and free (dashed lines) polymers for the system of different particle radii $R/aN^{1/2}=1, 2, 4,$ and ∞ (flat brush) at fixed brush thickness $H_{\text{brush}} = 2aN^{1/2}$ and $\alpha = 1$. The colored lines are difficult to distinguish because the convergence to the flat brush case is rapid. As seen in the inset, the lines are closely placed in the order of $R/aN^{1/2}=1, 2, 4,$ and ∞ . (b) Interfacial width w_I plotted as a function of R . The converging value corresponding to the flat brush case is denoted by a dashed arrow.

3.1 Brush Morphology of Isolated Particle

The morphology of the brush is determined not only by the system geometry but also by α , the molecular weight ratio of polymers. It is expected that for the mixture of grafted chains of length N and free chains of length αN , α is the most dominant factor determining the interpenetration of the polymer chains [43, 74, 75]. In order to examine this effect, radius $R = 2aN^{1/2}$ and brush thickness $H_{\text{brush}} = 2aN^{1/2}$ are chosen as the standard geometric parameters in this thesis, and the density profiles at various α values are plotted in figure 3-3 (a). Also, the interfacial width is plotted as a function of α in figure 3-3 (b).

The extreme case, $\alpha = 0.2$, is close to a brush in solvents, and the density profile of grafted polymers exhibits a slow decay over a long radial distance from the particle surface. It implies that at small α , the translational entropy of free polymers prevails conformational entropy of brush polymers, and thus free polymers penetrate deep into the brush and essentially form a brush in the wetting regime. As α increases, the translational entropy of free polymers reduces and segregation of the brush and free chains becomes more prominent. At larger α , the brush essentially goes into a dewetting brush regime, but the conformational entropy of the free chains remains finite and interpenetration of free chains never vanishes. Rather, the density profile approaches to a hyperbolic tangent like shape in the limit α goes to infinity. Convergence to the dewetting brush regime is so fast that above $\alpha = 2$, it almost converges to the limiting case of infinitely long homopolymers. Lines are very closely spaced, and the $\alpha = 15$ line is practically within the line width of the limiting curve.

According to the interfacial width plot (figure 3-3 (b)), transition from wetting (e.g., $\alpha = 0.2$) to dewetting (e.g., $\alpha = 4$) brush is accompanied by the decrease of the interfacial width as expected. In experiments, molecular weight ratio α is more easily controllable than the geometry, and it is notable that starting from the standard parameters of $R = 2aN^{1/2}$, $H_{\text{brush}} = 2aN^{1/2}$ and $\alpha = 1$, the change of parameter α induces most dramatic interfacial width change. At high enough α , above 4, penetration of polymers seems less dependent on the α value, converging to the infinite α case.

3.1 Brush Morphology of Isolated Particle

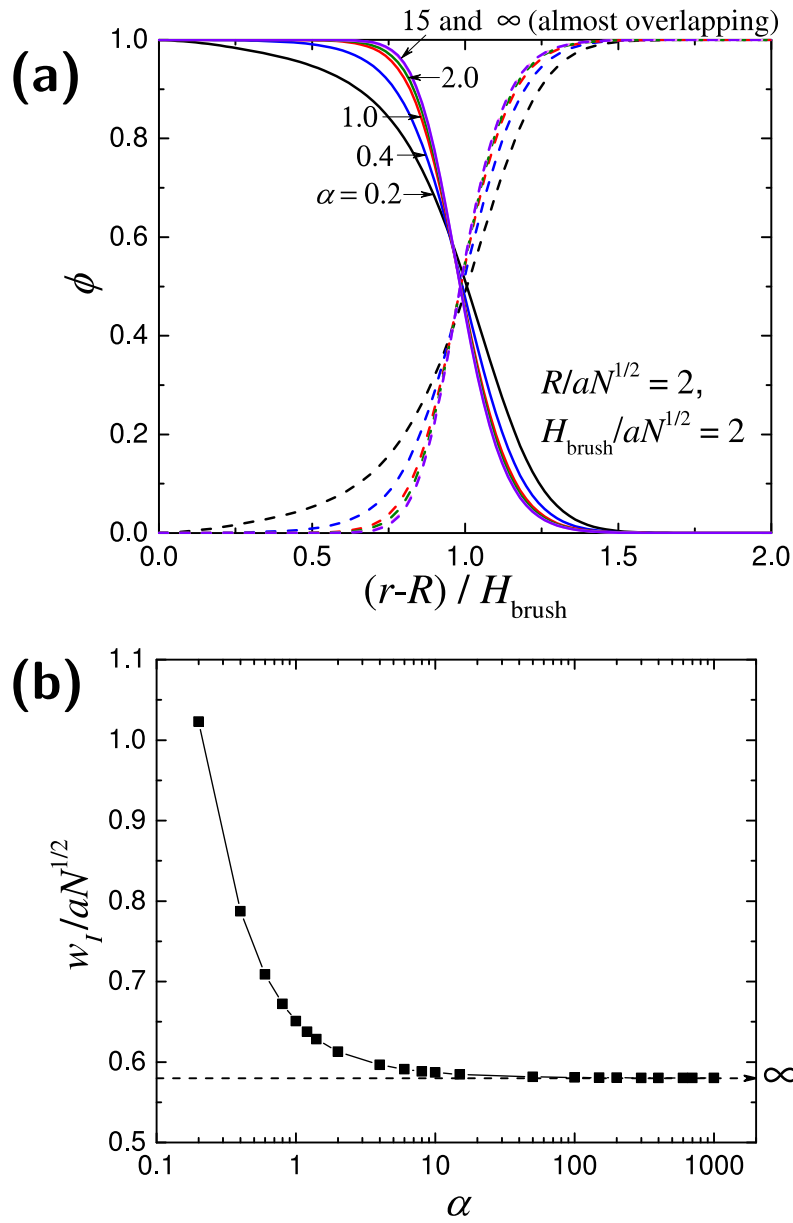


Figure 3-3: (a) Density profiles of grafted polymers (ϕ_g , solid lines) and free polymers (ϕ_f , dashed lines) for the standard system geometry with $R = 2aN^{1/2}$ and $H_{\text{brush}} = 2aN^{1/2}$ at α values from 0.2 to infinity. (b) Interfacial width w_I plotted as a function of α in a logarithmic scale. The converging value for the $\alpha \rightarrow \infty$ case is denoted by a dashed arrow.

3.2 Interaction Between Two Particles

If two brush-coated particles stay close to each other, their brush structure will be deformed and the interaction between the two particles can be significant. One may intuitively guess that the interaction must be repulsive because the brushes are compressed as the particles approach. However, as explained in the introduction chapter, due to the autophobic dewetting phenomenon and the resulting effective surface tension, I expect that a transition towards attraction occurs when α is large enough. In this section, I focus on the difference between wetting and dewetting brushes and their effects on the attractive or repulsive nature of the interaction. I then examine how parameters such as the polymer length ratio and particle geometry affect the interparticle interaction.

Lets first examine how the brush shapes are deformed as the interparticle distance changes. Figure 3-4 (a) shows the density profile change of typical brushes in the wetting regime formed by particles of radius $R = 2aN^{1/2}$ and brush thickness $H_{\text{brush}} = 2aN^{1/2}$, surrounded by short homopolymers with $\alpha = 0.2$. From the top to the bottom figures, the interparticle distance D changes from $6aN^{1/2}$ to $3aN^{1/2}$. Figure 3-4 (b) shows the corresponding brush morphologies for the typical monodisperse (PDI = 1.0) brush in the strong dewetting regime, $\alpha = 10$. For both cases, when $D \gg 2H_{\text{brush}}$ (upper figures), it can be regarded that two particles are separated far apart and they do not affect each other. Homopolymer melts occupy the space between them and the density contours are essentially spherical. As D decreases and two particles approach to each other, homopolymers between them start to be expelled, but this does not significantly change the brush structure until two brushes make contact at a distance just above $2H_{\text{brush}}$.

When brushes are compressed at smaller interparticle distances ($D < 2H_{\text{brush}}$), it is interesting that the deformation patterns are notably different for the two cases. For the monodisperse dewetting brushes ($\alpha = 10$ and PDI = 1.0), grafted polymers and free polymers are not well mixed; there is an effective surface tension at the boundary between them. In order to reduce this surface tension, two brush-homopolymer boundaries merge while most homopolymers are expelled out. As a result, $\phi_f(\mathbf{r})$ nearly vanishes in the area between two particles facing each other. On the other hand, in the wetting regime ($\alpha = 0.2$ and PDI = 1.0), brushes and homopolymers mix well, and a wide region in which the two types of polymers coexist can be found. Because of this, the spherical brush structures are less deformed compared to the brush in the dewetting regime and this tendency is notable when two particles are very close ($D = 3aN^{1/2}$). The density profile of the polydisperse dewetting brushes (figure 3-4 (c), $\alpha = 10$ and PDI = 1.4) is somewhat different from the monodisperse case, and it will be discussed in the next section. When the interparticle distance is very short, two brushes have a large contact area. It is notable that the density profile quickly recovers to the unperturbed state ($D = \infty$) at an angle just outside the contact area. Beyond that point, the density profile seems to have little

dependence on θ direction, and the brush shapes are almost spherical. This observation is valid for the brushes in both regimes.

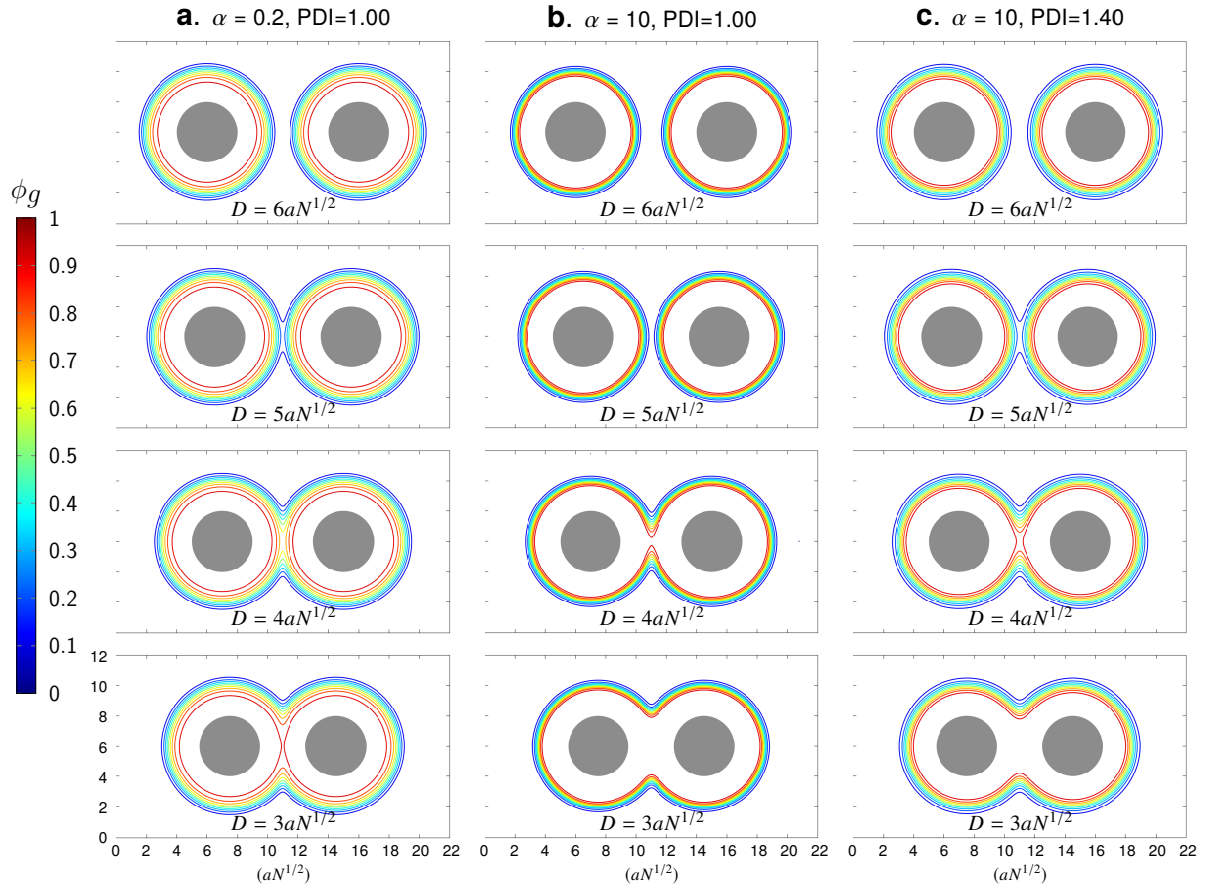


Figure 3-4: Contour plots of grafted polymer segment density, ϕ_g , of typical (a) wetting ($\alpha = 0.2$) and monodisperse (PDI = 1.00), (b) dewetting ($\alpha = 10$) and monodisperse (PDI = 1.00), and (c) dewetting ($\alpha = 10$) and polydisperse (PDI = 1.40) brushes calculated for two identical particles (gray circles) of radius $R = 2aN^{1/2}$ and brush thickness $H_{\text{brush}} = 2aN^{1/2}$, separated by various interparticle distances D . Ten curvilinear contour lines are drawn at each plot to represent grafted polymer density from 0 (blue) to 0.9 (red).

Now let me analyze the interaction between two standard particles of radius $R = 2aN^{1/2}$ and brush thickness $H_{\text{brush}} = 2aN^{1/2}$, in terms of the interparticle potential energy defined by Eq. (2.15). In figure 3-5, I show the interaction potential as a function of the interparticle distance D normalized by the brush height H_{brush} for different molecular weight ratios. In this theoretical analysis, I choose a wide range of parameter from $\alpha = 0.2$ to 20. Simulations with such long homopolymers have not been available before the adoption of the upgraded MCS scheme, and they are necessary to cover the two extreme cases, the wetting and dewetting regimes.

When α is very small, only repulsive interaction exists over all interparticle distances. At around $\alpha = 1$, repulsive interaction is always observed. As α increases, the situation changes and the free energy curve starts to develop an attractive well. Because the change is gradual, it is unclear exactly when the attraction becomes notable, and considering the particle size and grafting density dependence, it is practically impossible to present a single transition α value. For the standard system, with $R = 2aN^{1/2}$ and $H_{\text{brush}} = 2aN^{1/2}$, attractive interaction starts to compete with the thermal energy, $k_{\text{B}}T$, at around $\alpha = 2$. Attractive well becomes deeper at increasing α , and at above $\alpha = 4$, attraction strength can be significantly larger than the thermal energy. This observation confirms the idea that at large enough α , particles can form stable aggregations, despite that all the polymers are of the same type. The attraction keeps increasing at α above 10, but the potential becomes less dependent on α , and the potential depth may approach a limit at $\alpha = 20$ or above.

It is generally regarded that the sharpening of the interfacial width is the indicator of the autophobic dewetting. For example, in an SCFT research using α up to 4, Trombly and Ganesan reported quantitative correlation between the interfacial width and the interparticle potential [47]. The calculation shown figure 3-3 confirms such a trend at small α , but it is notable that the sharpening of interfacial width quickly converges at α above 2. It is interesting that the potential depth keeps increasing by a few factors in the regime where the interfacial width is practically invariant. Similar observations were reported earlier in simulations using molecular dynamics (MD) and MC methods [44, 76]. In one such work, Meng *et al.* found that density distributions of the brush and matrix chains around an isolated NP are very similar for two systems with different α , even when the interparticle potential changes from purely repulsive ($\alpha = 1$) to attractive ($\alpha = 7$) ones.

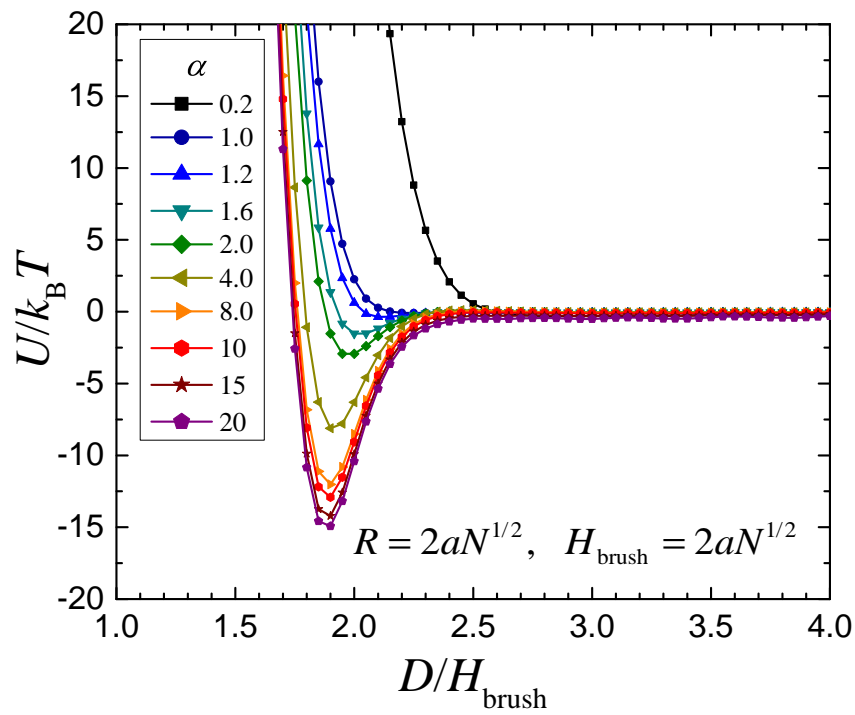


Figure 3-5: Interaction potential of two monodisperse-brush-grafted particles with radius $R = 2aN^{1/2}$ and brush thickness $H_{\text{brush}} = 2aN^{1/2}$ at various α values, as a function of the normalized interparticle distance D/H_{brush} . The cases of figure 3-4 (a) ($\alpha = 0.2$) and figure 3-4 (b) ($\alpha = 10$) correspond to the black and red lines, respectively.

I now present how the attraction between two particles in the dewetting brush regime is affected by the change of geometry and α . Figure 3-5 suggests that for the standard system ($R = 2aN^{1/2}$, $H_{\text{brush}} = 2aN^{1/2}$ and $\text{PDI} = 1.0$), matrix homopolymers with $\alpha = 4$ are just enough to initiate attraction between the particles, and thus let me first consider this case. Figure 3-6 (a) shows the shape of the interaction potential at various brush thicknesses. Attractive interaction is observed for stretched brushes, and the minimum of the interaction potential exists at a distance just below the brush contact point, $D = 2H_{\text{brush}}$. It is notable that for the brush with $H_{\text{brush}} = 1.0aN^{1/2}$, the interaction starts noticeably earlier at about $D = 2.5H_{\text{brush}}$ and the depth of the potential is difficult to identify in this graph. The brush is not well stretched in this case, and the autophobic dewetting behavior discussed earlier is not strong enough to create a clear attraction between the particles at $\alpha = 4$. As H_{brush} increases, autophobic dewetting becomes dominant, and the contact area between the particles also increases. Because of these effects, the depth of the attractive potential well keeps increasing. Figure 3-6 (b) shows the case with $\alpha = 10$. Compared to figure 3-6 (a), autophobic dewetting of the extremely long homopolymers exhibits a clear attraction even when the brush is not well stretched ($H_{\text{brush}} = 1.0aN^{1/2}$). The general trends of the interaction potential at increasing H_{brush} are similar except that the potential depth is noticeably larger at $\alpha = 10$. For the standard monodisperse brush system, a potential well depth of approximately $8k_{\text{B}}T$ and $13k_{\text{B}}T$ are observed at $\alpha = 4$ and 10, respectively.

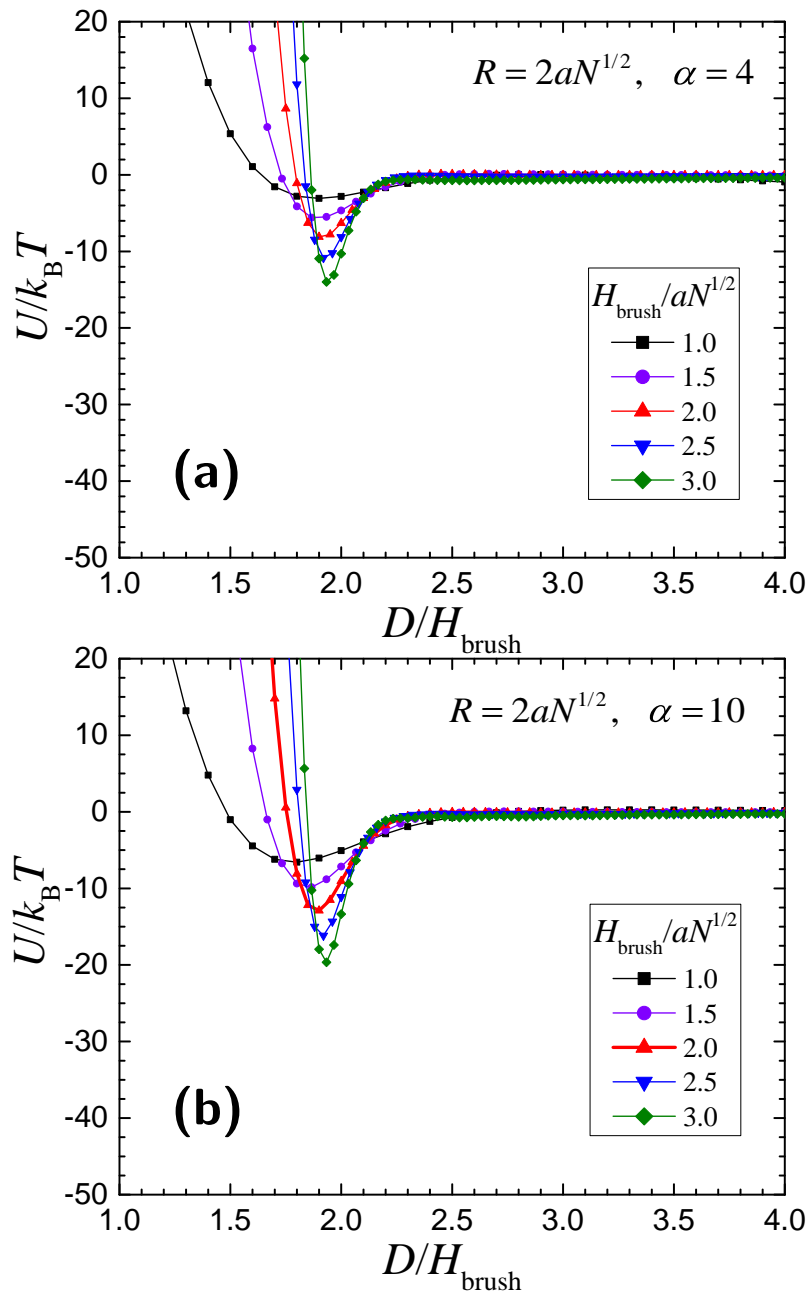


Figure 3-6: The interaction potential between two monodisperse-brush-coated particles at various brush thicknesses at (a) $\alpha = 4$ and (b) $\alpha = 10$. The case with radius $R = 2aN^{1/2}$ and brush thickness $H_{\text{brush}} = 2aN^{1/2}$ at $\alpha = 10$ is plotted with a thick red line on plot (b).

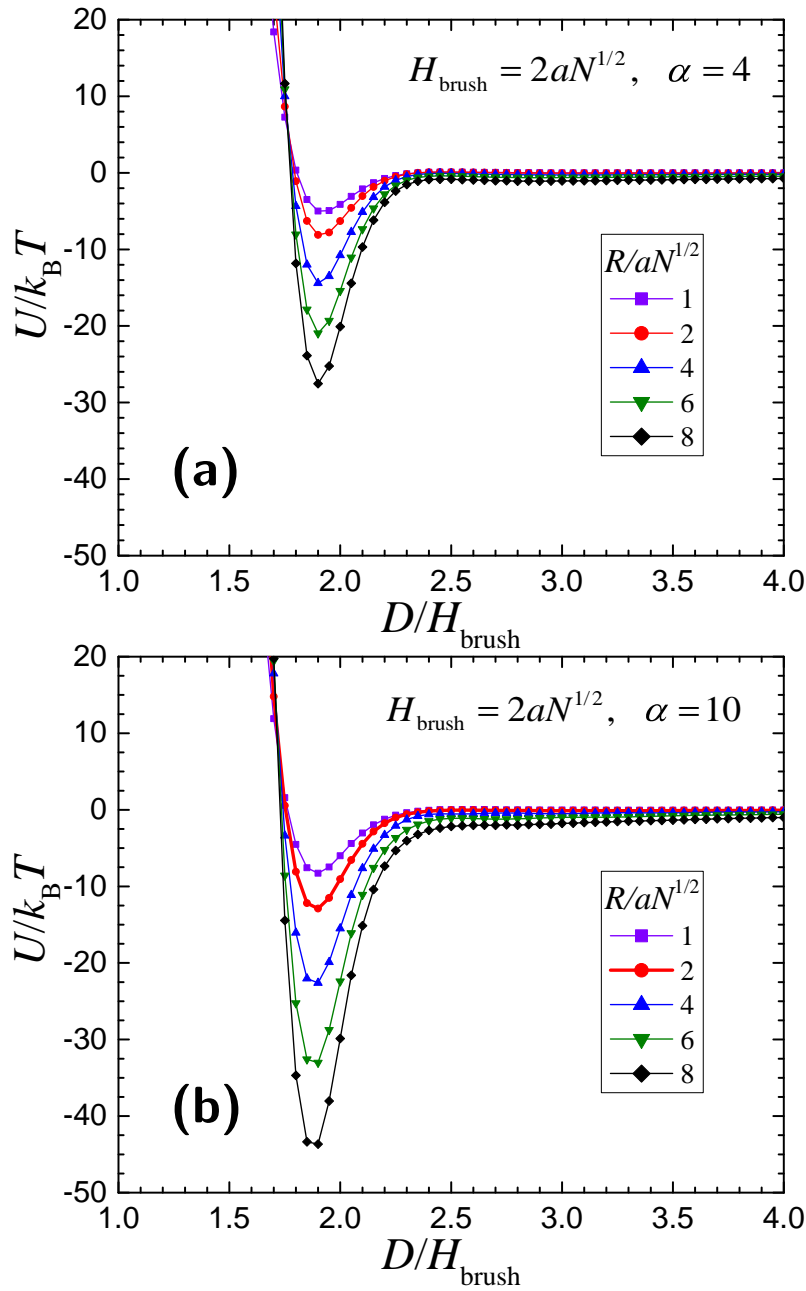


Figure 3-7: The interaction potential between two monodisperse-brush-coated particles at various particle radii at (a) $\alpha = 4$ and (b) $\alpha = 10$. The case with radius $R = 2aN^{1/2}$ and brush thickness $H_{\text{brush}} = 2aN^{1/2}$ at $\alpha = 10$ is plotted with a thick red line on plot (b).

Figure 3-7 (a) exhibits interaction between particles with sizes of $aN^{1/2}$, $2aN^{1/2}$, $4aN^{1/2}$, $6aN^{1/2}$ and $8aN^{1/2}$ at $H_{\text{brush}} = 2aN^{1/2}$, $\alpha = 4$ and PDI = 1.0, and figure 3-7 (b) shows the corresponding plot at $\alpha = 10$. As the particle size increases, potential well becomes deeper, and the largest particle, $R = 8aN^{1/2}$, shows $28k_B T$ ($\alpha = 4$) and $44k_B T$ ($\alpha = 10$) of potential well depth. The reduction of curvature provides one explanation to the increase of the potential depth, but a more crucial factor is that larger particles have more brush contact area, and more chains are affected by the approach of two spherical brushes.

3.3 Effect of Brush Polydispersity

The result of the previous section suggests that the autophobic dewetting effect is dominant when i) the brushes become thicker and ii) the free homopolymer length increases. From the former observation, one is tempted to reduce the brush grafting density to suppress dewetting of homopolymers on brushes and make well-dispersed NPs. Reduction of grafting density, however, is usually not a good strategy in the actual experiment because the system may easily fall into the allophobic regime as explained in the introduction, and particle aggregation due to van der Waals interaction between particle cores cannot be avoided [17, 19, 20, 77]. In this regard, the control of the free homopolymer length is a more promising approach. However, for some functional hybrid nanocomposites, long homopolymers with sufficient mechanical integrity are required for the application, and this limits the range of the homopolymer length [24]. As suggested earlier in this part of thesis, combination of short and long brush chains is expected to suppress autophobic dewetting and stabilize NP dispersion in a polymer matrix when compared to the monodisperse brush case.

Autophobic dewetting effect is related to the conformational entropy penalty of the same types of polymers in the process of matrix polymer penetration into the brush. In this context, I explore the effect of polydisperse brushes on autophobic dewetting in terms of their penetrating behavior and free energy depth. Figure 3-8 (a) shows profiles of grafted polymer density, ϕ_g , and free homopolymer density, ϕ_f , for different bidisperse brushes grafted on isolated particles with $R = 2aN^{1/2}$. The result of the monodisperse brush (PDI = 1.00) is included in the graph as red lines. The grafting density is chosen so that the brush thickness H_{brush} is fixed to $2aN^{1/2}$, and the monodisperse free homopolymers are 2 times longer than the number average length of grafted polymers, i.e., $\alpha = 2$. All the bidisperse brushes are prepared to have the same number-averaged molecular weight (M_n), and they consist of equal numbers of long and short chains. Specifically, when the average segment number is 200, the segment numbers of short polymers are 160, 143, 111 and 74 for polydispersity indices of 1.04, 1.08, 1.20 and 1.40, respectively. The corresponding long polymer segment numbers are 240, 257, 289 and 326, respectively.

The short grafted polymers have a tendency to stay near the particle surface, and the majority of the long grafted polymers naturally stretch beyond them. Because of this spreading effect, the polydisperse brush must have broader interface compared to the monodisperse one, and the penetration of free homopolymers occurs more easily as shown in figure 3-8 (a) in which the slope of density profiles becomes gradual as PDI increases. This observation is consistent with the idea that polydispersity suppresses the transition from wetting to autophobic dewetting [56]. In order to investigate the influence of polydispersity on the attractive interaction between two particles, I present in figure 3-8 (b) the interaction potential at $\alpha = 2$, which shows that the depth of the potential well is about $3k_B T$ for the monodisperse brush. As PDI increases, the

3.3 Effect of Brush Polydispersity

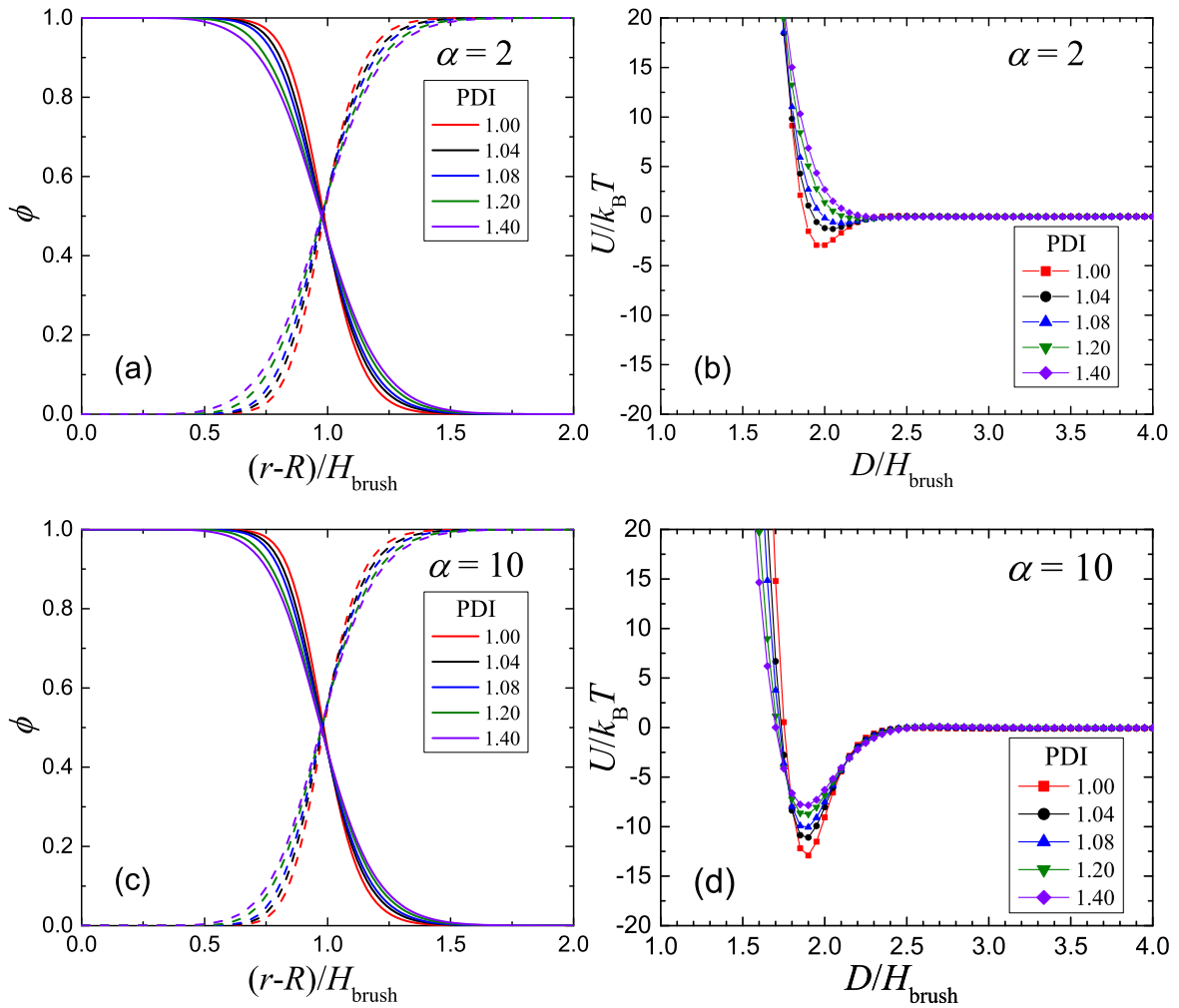


Figure 3-8: (a) Density profiles of grafted polydisperse polymers (ϕ_g , solid lines) and free homopolymers (ϕ_f , dashed lines) for the system geometry with $R = 2aN^{1/2}$, $H_{\text{brush}} = 2aN^{1/2}$ and $\alpha = 2$ at PDI values from 1.00 to 1.40. (b) The interaction potential between brush-coated particles at PDI values corresponding to (a). (c) and (d) are corresponding plots at $\alpha = 10$.

small attraction quickly diminishes. At above 1.08 of PDI, practically no attraction remains and the particles are expected to be well-dispersed.

It is interesting that the corresponding density plot at $\alpha = 10$ shown in figure 3-8 (c) is not so different from the $\alpha = 2$ case. Even though a much higher autophobic dewetting is expected, the difference of the density slope is barely noticeable at PDI = 1.0. At higher PDI, a slightly more pronounced slope difference is observed. However, the interparticle potential plotted in figure 3-8 (d) is completely different from the $\alpha = 2$ case. For the monodisperse brush, the depth of the potential well is about $13k_B T$ for the monodisperse brush which is more than fourfold increase from the $\alpha = 2$ case. The decrease of the potential depth at increasing PDI is not negligible, but at a reasonable PDI value of 1.4, $8k_B T$ of potential depth is still observed.

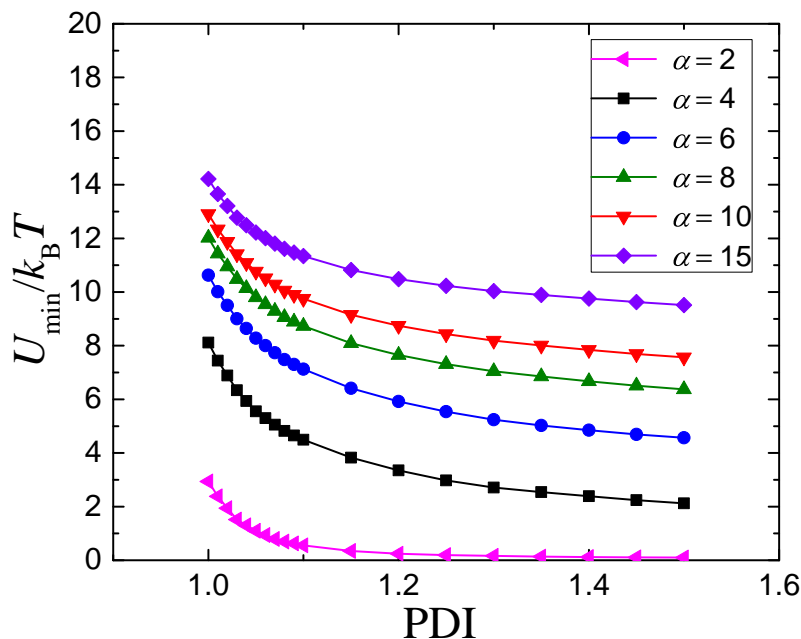


Figure 3-9: The depth of the potential plotted as a function of PDI at various α values with the system geometry of $R = 2aN^{1/2}$ and $H_{\text{brush}} = 2aN^{1/2}$.

Figure 3-9 summarizes the reduction of the potential depth. The attraction at $\alpha = 2$ quickly disappears at small PDI. At $\alpha = 4$, the starting point is $8k_B T$, but it halves at PDI 1.1. At high PDI, the attractive force may end up competing with the thermal energy. In a situation where particle aggregation is preferred, adoption of homopolymers longer than $\alpha = 4$ is the safe strategy, considering that maintaining low PDI for brush chains is usually a difficult task, and the potential depth can be much lower than these values for smaller particles.

The density contours of the polydisperse brushes for the case of particle radius $R = 2aN^{1/2}$, brush thickness $H_{\text{brush}} = 2aN^{1/2}$, $\alpha = 10$ and PDI = 1.4 are shown in figure 3-4 (c). Interestingly, at a larger interparticle distance ($D = 5aN^{1/2}$), the density profile is close to the wetting brush case (figure 3-4 (a)), and at a small distance ($D = 3aN^{1/2}$), it looks closer to the monodisperse dewetting brush case (figure 3-4 (b)). At an intermediate distance ($D = 4aN^{1/2}$), the profile positions somewhere between the two cases. The corresponding density contours for the case of $\alpha = 4$ are shown in figure 3-10. Even though the reduction of potential depth due to polydispersity is significant for $\alpha = 4$, figure 3-4 (c) and figure 3-10 (b) are not easily distinguishable. Even though the autophobic dewetting is the direct consequence of the entropy loss due to chain penetration, however, it is not easily predictable just from the density profile, which can also be confirmed by the similarity of figures 3-8 (a) and 3-8 (c).

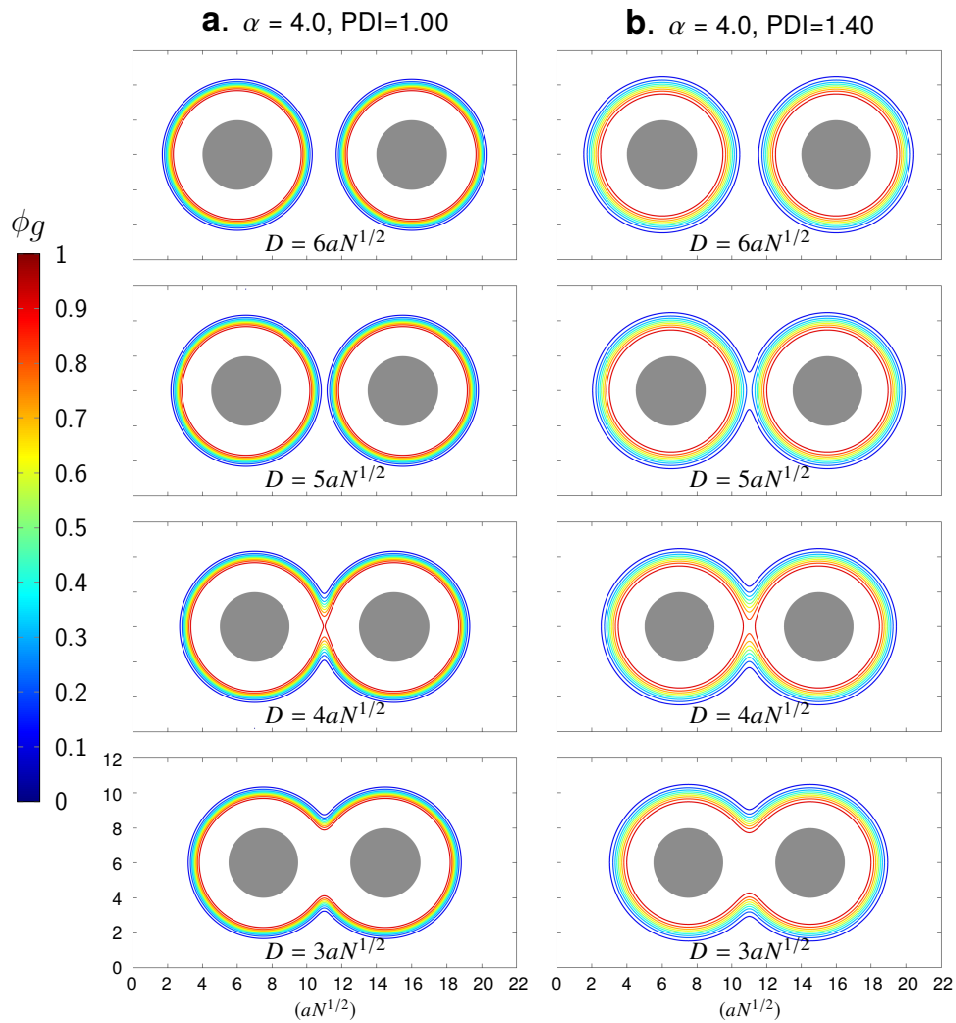


Figure 3-10: Contour plots of grafted polymer segment density, ϕ_g , of (a) $\alpha = 4.0$ and monodisperse (PDI = 1.00), and (c) $\alpha = 4.0$ and polydisperse (PDI = 1.40) brushes calculated for two identical particles (gray circles) of radius $R = 2aN^{1/2}$ and brush thickness $H_{\text{brush}} = 2aN^{1/2}$, separated by various interparticle distances D . Ten curvilinear contour lines are drawn at each plot to represent grafted polymer density from 0 (blue) to 0.9 (red).

3.4 Effect of Chain End Mobility

In the description of SCFT, two delta functions in Eq. (2.2) restrict the position of grafted chain ends on the spherical surfaces of the two particles. With the current formulation, however, the grafted chain ends still have the mobility to float on the surface laterally. This formalism is appropriate for the modeling of brushes formed by physically adsorbed chains because the functionalized chain ends can diffuse significant distances along the particle surface via thermal agitation in a realistic timescale [78]. Regardless of this degree of freedom, the grafting density must be a constant for an isolated particle due to the spherical symmetry. When two particles are close, however, high compression of brushes occurs and it is natural for the grafted chains to move away from the crowded region between the particles and lower the interaction energy [60].

In SCFT, the distribution of the grafted chain ends can be calculated by

$$\frac{\sigma(\theta)}{\sigma_0} = \frac{4\pi \int_R^\infty dr r^2 q_g(r, \theta, 1) q_g^\dagger(r, \theta, 1)}{\int d\mathbf{r}' q_g(r', \theta', 1) q_g^\dagger(r', \theta', 1)} \quad (3.2)$$

where σ 's in this section have the dimension of length^{-2} , and $\sigma_0 \equiv n_g/8\pi R^2$ is the average number of grafting points per unit surface area of NP [22, 46, 60]. Figure 3-11 (a) shows the equilibrium distribution of mobile chain ends at various interparticle distances for the case of $R = 2aN^{1/2}$, $H_{\text{brush}} = aN^{1/2}$ and $\alpha = 10$, which corresponds to the black line in figure 3-6 (b). When the particles are separated far enough ($D/H_{\text{brush}} = 4$), they are essentially two isolated particles and the grafted ends are uniformly distributed. As the interparticle distance decreases, θ dependence starts to be observed, and it explains the result of figure 3-6 (b) in which the interaction is noticeable at a little above $D/H_{\text{brush}} = 2$ for this parameter set.

In naïve expectation, the grafting density at the approaching pole, $\sigma(0)$, must decrease as the two particles approach. However, it is interesting that at about $D/H_{\text{brush}} = 3$, $\sigma(0)$ starts to exceed the average, σ_0 , and it keeps increasing until $D/H_{\text{brush}} = 2.2$ at which $\sigma(0)$ is about 2 percent higher than σ_0 . This phenomenon is a unique characteristic of dry brushes because it has not been observed for brush-coated particles in solvent [60]. Autophobic dewetting phenomenon provides one possible explanation for this observation. The effective surface tension prefers the reduction of free homopolymers in the region between the NPs, and the increase of $\sigma(0)$ helps the system to achieve it by increasing the brush chains in that region. When the two particles are closer, below $D/H_{\text{brush}} = 2$, the two brushes are clearly compressed, and depletion of grafting points is observed around the approaching pole (small θ). It is likely that the redistribution of grafted chain ends reduces conformational entropy loss due to the crowding of brushes at the compressed region. At larger θ , the grafting density reaches a plateau at a level slightly higher than σ_0 .

If the particle surfaces are prepared with fixed initiators and the brush chains are polymerized from the surface [29], the chains are chemically attached to specific sites on the spherical

surfaces. As shown in figure 3-11 (a), aforementioned modeling of brushes generates a non-uniform distribution of chain ends over the surface especially when the two interacting particles are very close, and it may be inappropriate for the study of the interaction between particles with end-fixed brushes. Slight modification to the theory is required for the analysis of the end-fixed brushes. Most SCFT equations introduced earlier are invariant. One exception is the initial condition equation (2.10), which now changes to $q_{g1}^\dagger(\mathbf{r}, 1) = (V_{g1}/4\pi R^2)\delta(r-R)/q_{g1}(\mathbf{r}, 1)$ [22,60,79]. This new initial condition guarantees that $\sigma(\theta)$ is always equal to σ_0 . For the detailed free energy expression of the end-fixed-brush SCFT and its derivation, see appendix B.

The interaction potential difference between the end-mobile and end-fixed brushes for a few parameter sets are presented in figure 3-11 (b). It is notable that when the two particles are close enough to produce high compression of polymer brushes, the interaction potentials are much steeper for the end-fixed brushes and the repulsion is much stronger. This result is natural because the redistribution of grafted ends has the effect of lowering the compression of polymer brushes. However, one must be careful in the interpretation of this data. At reasonable parameter values, with D just below the equilibrium distance, the repulsion between the two particles increases rapidly for both cases, and the region with significant force difference is practically inaccessible for real particles unless strong external forces are applied. It means that the grafting types may not be the major factor for the stabilization of brush-coated particles and the analysis of equilibrium morphologies. The contour plots of end-mobile and end-fixed brushes are provided in appendix C.

3.4 Effect of Chain End Mobility

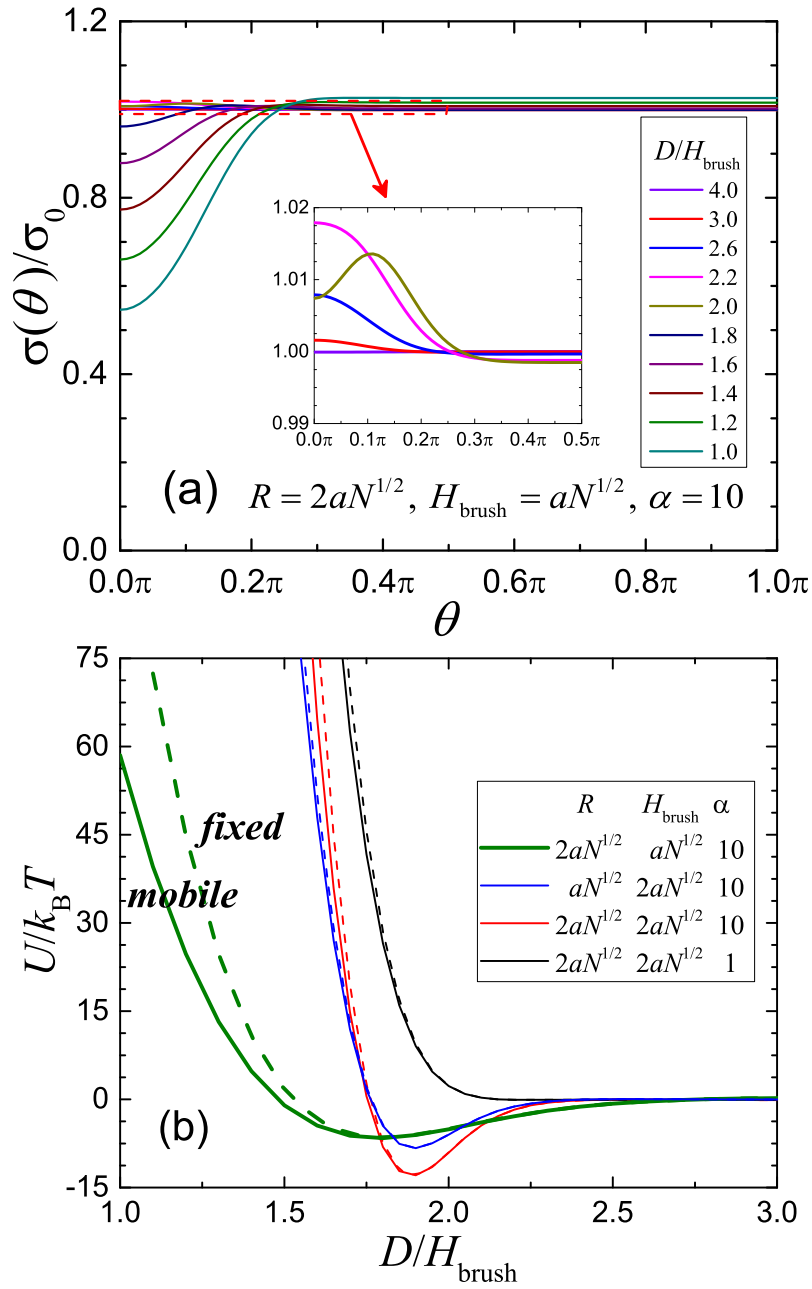


Figure 3-11: (a) Equilibrium grafting density at various interparticle distances, for the case of two end-mobile brush-covered particles with $R = 2aN^{1/2}$, $H_{\text{brush}} = aN^{1/2}$ and $\alpha = 10$. The inset magnifies the grafting density near $\theta = 0$. (b) Interaction potential graph for various system geometries and α values showing the difference of end-mobile (solid line) and end-fixed (dashed line) brushes. The thick solid green line corresponds to the system discussed in (a).

4

Conclusion

In this part of thesis, I investigated polymer-mediated interaction between brush-grafted spherical particles immersed in chemically identical homopolymer melts. The autophobic dewetting phenomenon was theoretically investigated by performing SCFT calculation of two particle system with the newly developed numerical scheme using MCS and FVM. By analyzing the interparticle interaction as functions of brush thickness H_{brush} , particle radius R , the molecular weight ratio of free to grafted polymers, α , and brush chain polydispersity, I found that the surface tension resulting from autophobic dewetting is responsible for the attractive interaction between NPs.

In order to quantify the degree of dewetting, the interfacial width was calculated from the polymer density profile and it was observed that at large α , segregation of brush and homopolymer chains is promoted. In this regime, conformational entropy of brush polymers prevails translational entropy of free polymers, and the autophobic dewetting of chemically identical polymers becomes prominent. In the analysis of the interaction potential between NPs, the transition from pure repulsion at small α to attraction at large α was clearly identified. The attraction kept increasing at α above 10, but it seemed to approach to a limit at $\alpha = 20$ or above.

The brush thickness H_{brush} and particle radius R also have some influences on the attractive nature of the particle interaction in that the depth of attractive potential well increases as H_{brush} or R increases. In addition, I investigated the effects of brush polydispersity and brush chain end mobility on the attractive nature of the interaction. As suggested earlier [56], polydisperse brush suppresses autophobic dewetting and the attractive interaction weakens compared to the monodisperse case, but the effect of polydispersity is limited in that finite attraction remains for highly polydisperse brushes. The introduction of chain end mobility induces significant brush chain redistribution, but they do not have major influence on the equilibrium nanocomposite structure experimentally attainable.

This work provides the fundamental understanding of the behavior of NPs within the polymer matrix, which is very important in the rational design of well-defined nanocomposites.

Furthermore, I anticipate that this research can be extended to more complex systems. One possible example is to use NPs grafted with brush chains that are chemically different from polymer matrix. Also, more than one type of polymers can be grafted to NPs within various surrounding matrices such as block copolymers or other heterogeneous substrates. The precise control on the dispersity and positioning of these NPs within functional materials will enable to create nonconventional, high-performance nanocomposites that have the promising potentials in various applications including electronic, optical, and magnetic devices.

Part II

Numerical Implementation of Pseudo-spectral Method in Discrete Chain Self-consistent Mean Field Theory

5

Introduction

Since polymers consist of a large number of monomers which are numerically intractable in a deterministic way, in the theoretical study of polymers, equilibrium behavior of a polymeric system is usually described by statistical approach, and coarse-graining procedure is required in the modeling of real polymer chains. Many monomers are connected by chemical bonds in a polymer chain, and one such example is shown in figure 5-1 where each monomer in a linear polystyrene (PS) chain is represented by a small blue bead. In a mesoscopic description of a polymer chain, modeling of each bead is not necessary due to the universality established by earlier polymer theories [80]. In this regard, as shown in figure 5-1, a few beads are treated as a statistical segment, and the property of the polymers is matched by controlling the property of segments and bonds connecting them. Because of this, the theory of polymer physics has been developed into a special direction. First-principles calculation [81–83], molecular dynamics (MD) simulation [84–87], and Monte Carlo (MC) simulation [88, 89] are still useful theoretical tools as in other fields, but a statistical mechanical tool known as the self-consistent field theory (SCFT) [64, 73, 90–94] has been established as a powerful alternative approach.

The SCFT was developed to predict the statistical behavior of a polymer system by converting a particle-based statistical description of polymers into a field-based one. In this approach, many body interactions between segments are replaced by the external potential field which is determined by the polymer density distribution, and free energy can be calculated along with the self-consistently determined potential field. This mean field approximation makes SCFT a suitable tool to simulate a large-scale system which is computationally demanding in a particle-based simulation, and the computational advantage makes it possible to successfully obtain the block copolymer phase diagram [64, 90, 93, 95, 96].

Many SCFT frameworks have been developed so far, but the most widely used one is the Gaussian chain model [64, 91, 93], which approximates a long polymer as a continuous elastic chain represented by a smooth curve in space. One reason for the popularity of this model is its simple formulation in the numerical calculation. In this formulation of SCFT, the partition function calculation reduces to solving a differential equation in the form of a modified diffusion

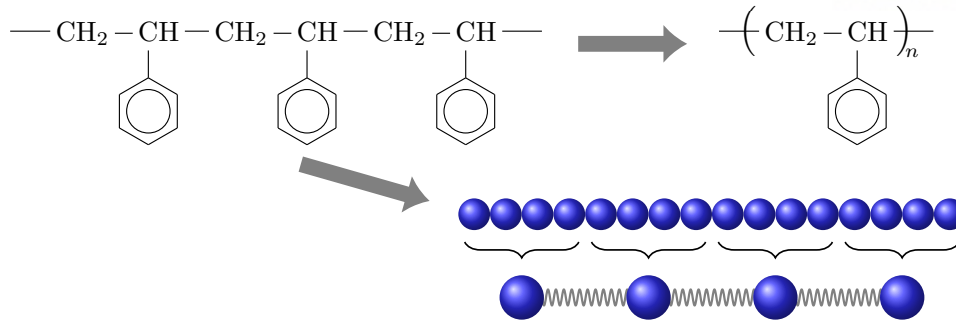


Figure 5-1: Example of polymer abstraction and segment modeling of a linear PS chain with n styrene units. Each small blue bead represents one PS monomer. The collection of a few monomer units forms a coarse-grained segment, and the linear polymer chain is modeled by many segments connected by bonds. The coarse-grained segment and bond represent the microscopic degree of freedom of the polymer chain.

equation. For the purpose of distinction, I will call this method the standard SCFT in this thesis. Because Gaussian chain model assumes that polymers are infinitely flexible, the standard SCFT is appropriate for the modeling of long polymers, and there is a limitation that it is only applicable to high molecular weight polymers whose average end-to-end length is much shorter than its contour length along the backbone.

Polymers with low molecular weights are one of the promising materials in recent nanoscience. For example, for the creation of sub-10 nm nanostructure, diblock copolymers with high Flory-Huggins interaction parameter χ and low polymerization index N have been widely studied [97–99]. However, the above discussion implies that when the standard SCFT is applied to the calculation of the mean field statistics of short polymer chains, it may sometimes produce unphysical results.

There is another limitation of the Gaussian chain model. It fails to explain some physical properties emerging from the discreteness of chains or physical phenomena originated from the atomistic scales. For example, the statistical mechanics of ideal polymer chains next to a hard wall and the effective surface tension due to entropic origin have been known to be difficult to calculate by using the Gaussian chain model [100–102], because it is plagued by unphysical effects such as the diverging entropy loss near the hard wall. These limitations require alternative chain modeling which can be incorporated with the SCFT for the investigation of statistical mechanics of discrete short polymer chains.

Alternative polymer models which may resolve these issues are indeed available. For example, lattice SCFT adopting random walks with fixed direction and length has been available from the earlier development of the SCFT [103–106], but due to its limitation in accuracy and speed, the standard SCFT has become more popular and the lattice SCFT is now used in limited situations only. An SCFT method accounting for the stiffness of chains by wormlike chain model has been suggested and recently used to solve a few problems [102, 107, 108]. However, the dimensionality of the differential equation increases when moving away from the Gaussian chain model, and

the computational demands increase dramatically for the three-dimensional problems.

Recently, there have been some attempts to apply the SCFT to discrete polymer chains consisting of a finite number of segments connected together by the freely-jointed or Hookian-spring bonds. In this discrete chain formulation, the partition functions are calculated through iterative integral equations rather than solving the diffusion equation as in the standard SCFT. For its distinction from the standard SCFT, I will call this method discrete chain SCFT in this thesis. The fundamental idea of the discrete chain SCFT is that the chain propagation is described as a stochastic process, and the partition function of each segment is recursively built up from an integral representation of the probability distribution known as Chapman-Kolmogorov equation [109]. In some polymer physics textbooks [93, 110, 111], the integral equation approach using the discrete chain model is often presented as an intermediate step for the introduction of the continuous Gaussian chain model because the discrete chain is easier to visualize and its convergence to the Gaussian chain is intuitive from the central limit theorem. In continuous limit, the integral equations for calculating the discrete chain statistics can be reduced to a linear partial differential equation which I will introduce later.

Even though the discrete chain formulation has been known from the early stage of polymer field theory, numerical implementation of the integral equation approach to the analysis of complex polymeric systems has become popular only in recent years. In 2009, Matsen, Kim, and Likhtman published a paper performing the numerical calculation of the freely-jointed chain (FJC) partition function near a neutral wall [101]. In this approach, the partition function of the polymer segments is calculated by one-dimensional spatial integrals accounting for the probability change from one segment to another. Later works extend this method for the analysis of chain end distribution of short incompressible polymers next to a surface [112–114]. Romeis et al. also adopted a similar methodology in the SCFT calculation of a brush system [115]. They used the off-lattice model for FJC, and their results were compared with the MD simulation data.

Even though the above papers successfully implemented the integral equation approach of the partition function calculation, the formulations are limited to one-dimensional systems after assuming translational invariance in the lateral direction. For a general problem with three-dimensional complexity, however, accurate calculation of the partition function in real space becomes extremely costly. As will be discussed in more detail in chapter 7, three-dimensional calculation of the discrete chain SCFT is inevitably slower than the standard SCFT.

Recently, Matsen demonstrated that this issue can be resolved by using the spectral method where all calculations are performed in Fourier space with symmetrized basis functions [116]. In his paper, the free energies of complex block copolymer morphologies are calculated using efficient numerical implementation of the discrete chain SCFT adopting the FJC model. As a result, the full phase diagram of diblock copolymers with low molecular weights is obtained, and

he found a noticeable upward shift of the order-disorder transition χN after assuming finite-range interaction between segments. This study proves that the discrete chain SCFT can be equally efficient to the standard SCFT adopting the Gaussian chain model when implementing the full-spectral approach. This efficiency comes from the symmetry in ordered periodic morphologies which reduces the number of required Fourier coefficients, but such a symmetry may not be present in many polymer science problems. In addition, there is a disadvantage in conducting some calculations in Fourier space. Simple scalar multiplications in real space would become a matrix multiplication which is computationally costly to perform in Fourier space.

This complication can be avoided by using a pseudo-spectral strategy which allows flexible switch between Fourier space and real space, and this numerical method is known to be less restrictive and more versatile compared to the full spectral method. Adoption of the pseudo-spectral method for solving the recursive integral equations of partial partition function has been suggested earlier by Fredrickson [93], and Matsen also mentioned the possibility of the pseudo-spectral method for the fast calculation of the discrete chain SCFT [116]. However, the actual implementation of the pseudo-spectral method in the calculation of the discrete chain SCFT has not been reported yet.

In the part II of this thesis, I present a generic theory of the discrete polymer chain SCFT in a form ready for the optimal implementation of the pseudo-spectral method. There are some unexpected issues one inevitably faces in the implementation of the pseudo-spectral algorithm, and the details will be discussed later. After the successful implementation, I test various properties of short polymer chains with the finite number of segments. In addition, to test the practicality of the algorithm, the fundamental problem of block copolymer morphology confined between two walls is investigated using this approach.

6

Theory of Discrete Chain SCFT

6.1 Background

The most popular version of the SCFT nowadays is based on the Gaussian chain model. It is typical to introduce the Gaussian chain model from discrete N segments as seen in figure 5-1, and by taking the long chain limit ($N \rightarrow \infty$), the chain becomes infinitely flexible. In this standard SCFT formalism, the segment position along the backbone of the polymer is specified by a continuous parameter $s \in [0, 1]$ (see figure 6-1 (a)), and this model allows the use of modified diffusion equation for the calculation of the partition function which is required for the prediction of the statistical behavior of the polymer system.

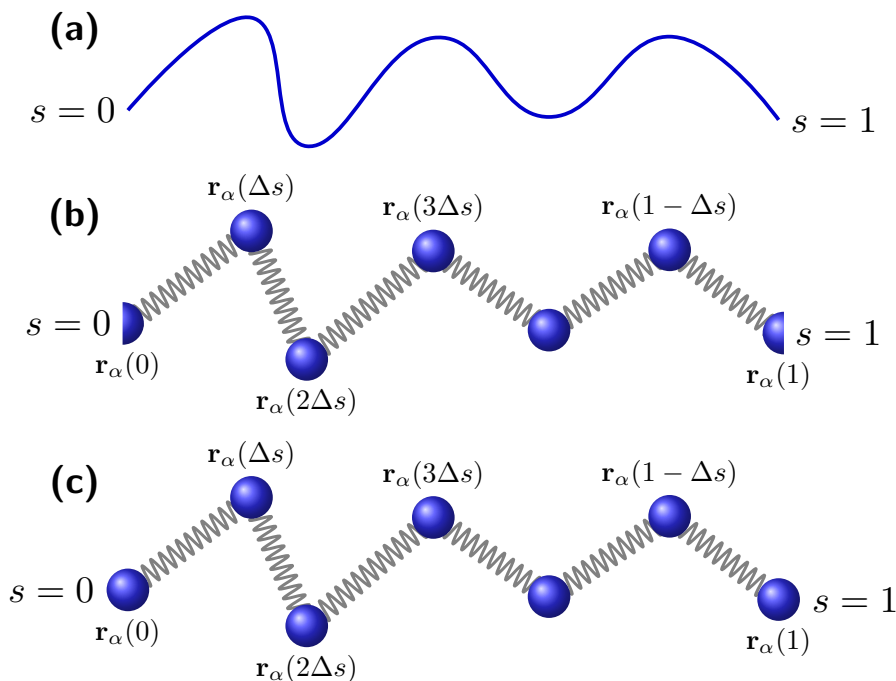


Figure 6-1: The polymer chain parametrization of the (a) Gaussian chain model, (b) N bond model, and (c) $N - 1$ bond model. For the Gaussian chain model, the curve $\mathbf{r}_\alpha(s)$ is defined at all s in $[0, 1]$, but the function is defined only at discrete points with intervals $\Delta s \equiv 1/N$ and $\Delta s \equiv 1/(N - 1)$ for the cases of N bond model and $N - 1$ bond model, respectively.

Partial partition function of sN segments starting from the $s = 0$ chain end can be written as $q(\mathbf{r}, s)$, where \mathbf{r} is the sN th segment position, and it satisfies the following modified diffusion equation,

$$\frac{\partial}{\partial s} q(\mathbf{r}, s) = \left(\frac{a^2 N}{6} \nabla^2 - w(\mathbf{r}) \right) q(\mathbf{r}, s), \quad (6.1)$$

where a is the statistical segment length and $w(\mathbf{r})$ is the self-consistently determined mean potential field acting on the segment at position \mathbf{r} [64,93]. The complementary partial partition function of $(1 - s)N$ segments starting from the $s = 1$ chain end, $q^\dagger(\mathbf{r}, s)$, satisfies the same modified diffusion equation (6.1) with the left-hand side multiplied by -1 . Using these two partial partition functions, mean field quantities such as the total partition function of the chain and the polymer density distribution can be calculated. The mean field free energy of the system is found after the self-consistent solution is obtained.

It is obvious that a real polymer is not infinitely flexible, and the Gaussian chain model inevitably fails at a small scale. As explained in the introduction chapter, this problem becomes more significant for short polymer chains, and it is required to recheck the fundamentals of the polymer statistics calculation to find a valid alternative method.

One suggestion is to directly solve the integral equations of partition functions which utilizes the theory of Markovian stochastic process [109]. This approach retains the discreteness of chain by assuming a finite number of segments, and as shown in figure 6-1 (c), the segment positions along the polymer backbone are now specified by N discrete points of $s = n\Delta s$ ($n \in \{0, 1, \dots, N - 1\}$) where $\Delta s \equiv 1/(N - 1)$. Its fundamental idea is that the probability density to observe the $(s + \Delta s)N$ th segment at position \mathbf{r} can be built up by means of a Chapman-Kolmogorov equation when the probability density distribution of the sN th segment is already known [93, 101, 110, 111].

For a noninteracting chain, random step propagation of the chain suggests that the partial partition function $q(\mathbf{r}, s + \Delta s)$ can be recursively obtained from the distribution of the sN th partial partition function, $q(\mathbf{r}, s)$,

$$q(\mathbf{r}, s + \Delta s) = \int d\mathbf{R} g(\mathbf{R}; \mathbf{r} - \mathbf{R}) q(\mathbf{r} - \mathbf{R}, s), \quad (6.2)$$

where the bond function $g(\mathbf{R}; \mathbf{r} - \mathbf{R})$ represents the conditional probability density that the bond vector from the sN th segment located at position $\mathbf{r} - \mathbf{R}$ to the $(s + \Delta s)N$ th segment assumes a displacement vector of \mathbf{R} . The partition function $q(\mathbf{r}, s)$ can be built up recursively for all segment points $s = n\Delta s$ starting from $n = 0$.

In the absence of external fields, the random walking nature of the chain shows Markov process, and the probability distribution of the bond $g(\mathbf{R}; \mathbf{r} - \mathbf{R})$ becomes independent of the starting position which allows one variable function $g(\mathbf{R})$. In the theory of statistical mechanics, statistical weight of each segment is closely related with its probability density, and thus

Eq. (6.2) corresponds to the Chapman–Kolmogorov equation in the theory of stochastic process. Considering that Eq. (6.1) is the differential form of the Chapman–Kolmogorov equation, the relation of the above equations becomes easier to understand. The solution of the partition functions obtained by this integral method reduces to the solution of the modified diffusion equations without field in the limit Δs goes to 0.

However, considering that the integral approach retains the property of discrete chains, it is an attractive idea to remain in the discrete chain model especially when investigating the behavior of short polymer chains. Previous papers adopting this model have directly borrowed the integral equations, but in the next section, I will rigorously derive the formalism of the discrete chain SCFT in an integral form, starting from the fundamental definition of the partition function and free energy. In doing so, whenever I have a choice, I will adopt a method which is optimized for the numerical implementation and which can easily visualize its convergence to the standard SCFT.

6.2 Chain Models

In this section, the basic methods of discrete polymer chain modelings are introduced. I first present the coarse-grained chain model with the most intuitive choice, and then I will move onto a different model. The discussion starts from the observation of the previously used discrete chain modeling, taking a symmetric ($f = 0.5$) diblock copolymer as an example. As depicted in figure 6-2 (a), the AB block copolymer chain consists of many A and B types of monomers.

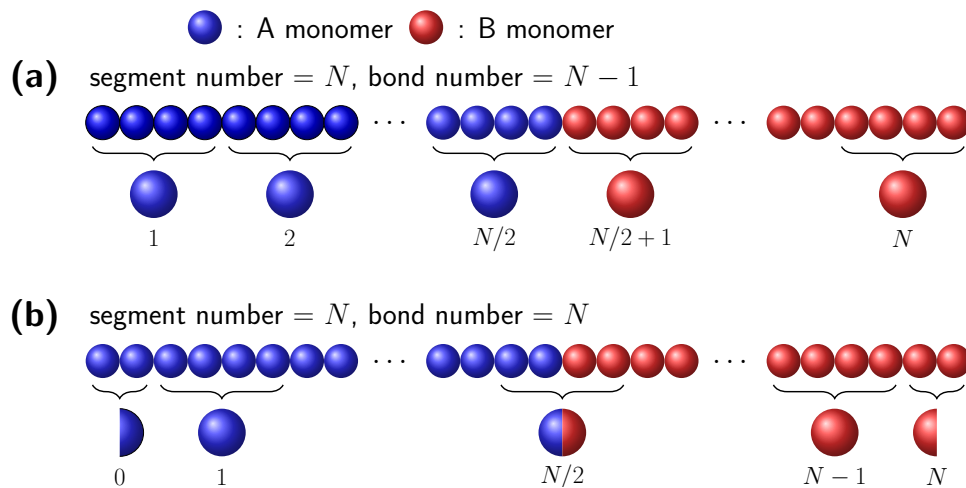


Figure 6-2: (a) Symmetric ($f = 0.5$) diblock copolymer with N beads and $N - 1$ bonds. (b) Symmetric diblock copolymer with N beads and N bonds.

In the process of chain modeling, a few monomers are coarse-grained to form a segment; in the figure, by combining four monomers in one segment, $N/2$ A segments and $N/2$ B segments are constructed. The random walking nature of the polymer chain is embedded in the bond connecting the neighboring segments, and the property of the bond depends on the actual

architecture of the chain and the scale of coarse-graining. If the chain is long enough, the central limit theorem guarantees that successive random walks produce Gaussian probability distribution, and this is the reason why the Gaussian chain model must be successful in the long chain limit.

The chain is represented by N segments in figure 6-2 (a), but the number of bonds is actually $N - 1$. In the absence of the field, the natural end-to-end distance of the chain becomes $R_0 = a(N - 1)^{1/2}$, where a is the one bond length. It is slightly shorter than the well-known expression $aN^{1/2}$, and this difference is often ignored with the justification that it is negligible in the long chain limit. However, it is not a small difference to ignore for the short and intermediate length chains. There exists another finite length effect which is often overlooked. One usually uses $R_g^2 = a^2N/6$ as the square of the radius of gyration, but calculation with the assumption that the mass is discretely concentrated at the segment position shows $R_g^2 = a^2N(N + 1)/6(N - 1)$. The required correction term is $O(1)$ and it does not vanish even in the limit $N \rightarrow \infty$. Expressing all the equations using $N' \equiv N - 1$ allows us to write $R_0 = aN'^{1/2}$, but this policy does not help one to reduce the error in the radius of gyration expression.

This observation leads me to consider another model which may look unnatural at first glance for those who are not accustomed to it. When combining monomers to form segments, the process starts by creating a half-segment as shown in figure 6-2 (b) and label it as the 0th segment for convenience. All the subsequent segments are full-segments except the last (N th) one which is again a half-segment. The total number of points is now $N + 1$, but because two of them are half-segments, I formally counts N segments. If the segment number is large, both models converge to the standard Gaussian chain model, and they do not make a noticeable difference in predicting the statistical behavior of polymers. For the case of low molecular weight polymers, however, N is small and the difference can be significant. Because of the presence of the two half-segments, now the number of bonds is N and the natural end-to-end distance is $R_0 = aN^{1/2}$. In addition, calculation of R_g assuming that the mass is discretely concentrated at the segment position results in a value $R_g^2 = a^2(N/6 + 1/12N)$. It is much closer to $a^2N/6$ compared to the old model, and the correction term is $O(1/N)$.

For future distinction, I will use the term “ $N - 1$ bond model” and “ N bond model” for figures 6-2 (a) and 6-2 (b), respectively. The statistical mechanical description of the two models are very similar, and thus the next section starts from the discrete chain SCFT formalism of the N bond model. Its application to the $N - 1$ bond model will be explained at the end of the next section.

6.3 Algebraic Formulation

This section presents the discrete chain SCFT formulation of a sample system with an incompressible melt of AB block copolymers. The system is composed of n_p symmetric AB block copolymer chains with A fraction $f = 0.5$ and total segment number N . Even though the $N - 1$ bond model seems to be more natural, let's start the algebraic formulation from the N bond model. It is partially because the equations become simpler in this model, and its modification to the $N - 1$ bond model is a trivial task as explained at the end of this section. For the recursive equation of the N bond model, calculation of the partial partition function becomes multiple applications of a single evolution step without any exception, because any chain fragment in the intermediate step has two half-segment ends unlike the $N - 1$ bond model.

The segment positions of the α th polymer chain can be represented by the function $\mathbf{r}_\alpha(s)$ as shown in figure 6-1 (b). In the standard SCFT, $\mathbf{r}_\alpha(s)$ is a continuous function, but for the discrete chain, its values at $N + 1$ discrete points of $s = n\Delta s$ ($n \in \{0, 1, \dots, N\}$ and $\Delta s \equiv 1/N$) are only meaningful, and it is assumed that the polymer mass is concentrated at these positions. Even though each segment has a volume ρ_0^{-1} , it can be treated as a point-like object for the density calculation.

Considering that the 0th and N th segments are half-segments, the spatial densities of A and B type segments in the α th chain are given as

$$\hat{\phi}_{\alpha,A}(\mathbf{r}) = \frac{1}{\rho_0} \sum'_{s \in \{0, \dots, f\}} \delta(\mathbf{r} - \mathbf{r}_\alpha(s)) , \quad (6.3a)$$

$$\hat{\phi}_{\alpha,B}(\mathbf{r}) = \frac{1}{\rho_0} \sum'_{s \in \{f, \dots, 1\}} \delta(\mathbf{r} - \mathbf{r}_\alpha(s)) , \quad (6.3b)$$

$$\sum'_{s \in \{t, \dots, u\}} f(s) \equiv \frac{f(t)}{2} + f(t + \Delta s) + \dots + f(u - \Delta s) + \frac{f(u)}{2} , \quad (6.3c)$$

where it is assumed that the chain is properly discretized so that a half-A and half-B segment shown in figure 6-2 (b) is present at the position f , and $u - t$ is always an integer multiple of Δs . The half contributions coming from both ends are represented by the primed summation. The meaning and effect of the half-A and half-B segment will be discussed later.

For the time being, let us use the bead-spring (BS) model, which is a very common choice in polymer physics. In the BS model, neighboring segments are connected by one spring bond whose length a represents the root-mean-square (RMS) average of a random step. The free

energy of the chain segments $[s_1, s_2]$ in an external field $w(\mathbf{r})$ is given as

$$\Delta \mathbf{r}_\alpha(s) \equiv \mathbf{r}_\alpha(s) - \mathbf{r}_\alpha(s - \Delta s) , \quad (6.4a)$$

$$\begin{aligned} \frac{E(\mathbf{r}_\alpha; s_1, s_2)}{k_B T} &= \frac{1}{N} \sum_{s \in \{s_1 + \Delta s, \dots, s_2\}} \frac{3}{2a^2 N} \left[\frac{\Delta \mathbf{r}_\alpha(s)}{\Delta s} \right]^2 \\ &+ \frac{1}{N} \sum'_{s \in \{s_1, \dots, s_2\}} w_\kappa(\mathbf{r}_\alpha(s)) . \end{aligned} \quad (6.4b)$$

The prefactor $3/2a^2N$ represents the strength of the spring, and it is properly chosen to make the RMS end-to-end distance R_0 of a non-interacting chain to be $aN^{1/2}$. The field is defined in a way that one κ -type of segment ($\kappa = A$ or B) at position \mathbf{r} experiences $w_\kappa(\mathbf{r})/N$ of energy penalty. The subscript will be often omitted with the implicit understanding that $w(\mathbf{r})$ is properly chosen according to the s value. In the limit $N \rightarrow \infty$, this definition converges to the field in the standard SCFT, where $E[\mathbf{r}_\alpha; s_1, s_2]$ is a functional depending on the function $\mathbf{r}_\alpha(s)$. In the discrete chain SCFT, it becomes a multivariable function with $N + 1$ position variables $\mathbf{r}_\alpha(s)$ ($s \in \{0, \Delta s, \dots, 1\}$).

For the full understanding of the partition functions in this SCFT formulation, let us start from the two-point partial partition function for a chain segment of length sN starting from A end whose $s = 0$ segment position is fixed at \mathbf{r}_0 ,

$$\begin{aligned} q(\mathbf{r}, \mathbf{r}_0, s) &= \left(\frac{2\pi}{3N} \right)^{3/2} \prod_{u \in \{0, \dots, s\}} \left(\frac{3}{2\pi a^2} \right)^{3/2} \int d\mathbf{r}_\alpha(u) \\ &\times \exp \left(-\frac{E(\mathbf{r}_\alpha; 0, s)}{k_B T} \right) (a^2 N)^3 \\ &\times \delta(\mathbf{r}_\alpha(0) - \mathbf{r}_0) \delta(\mathbf{r}_\alpha(s) - \mathbf{r}) , \end{aligned} \quad (6.5)$$

and the complementary two-point partial partition function for a chain segment of length $(1 - s)N$ starting from B end whose $s = 1$ segment position is fixed at \mathbf{r}_1 ,

$$\begin{aligned} q^\dagger(\mathbf{r}, \mathbf{r}_1, s) &= \left(\frac{2\pi}{3N} \right)^{3/2} \prod_{u \in \{s, \dots, 1\}} \left(\frac{3}{2\pi a^2} \right)^{3/2} \int d\mathbf{r}_\alpha(u) \\ &\times \exp \left(-\frac{E(\mathbf{r}_\alpha; s, 1)}{k_B T} \right) (a^2 N)^3 \\ &\times \delta(\mathbf{r}_\alpha(s) - \mathbf{r}) \delta(\mathbf{r}_\alpha(1) - \mathbf{r}_1) . \end{aligned} \quad (6.6)$$

In the standard SCFT, it is required to perform a path integral following all the possible paths of a polymer chain [64, 93]. In the current SCFT formalism, however, the partition functions are products of many normal integrals over the space. Such a change allows us to identify the exact prefactors of the partition functions which are often ambiguously written in the functional integral version. In a formal language, the continuous limit of this product of discrete integrals corresponds to the functional integral of the standard SCFT.

After some algebraic derivation found in appendix D, the recursive integral equation of the partition function can be obtained as

$$g(\mathbf{r}) \equiv \left(\frac{3}{2\pi a^2} \right)^{3/2} \exp\left(-\frac{3\mathbf{r}^2}{2a^2}\right), \quad (6.7a)$$

$$\begin{aligned} q(\mathbf{r}, \mathbf{r}_0, s + \Delta s) &= \exp\left(-\frac{w(\mathbf{r})}{2N}\right) \int d\mathbf{R} g(\mathbf{R}) \\ &\times \exp\left(-\frac{w(\mathbf{r} - \mathbf{R})}{2N}\right) q(\mathbf{r} - \mathbf{R}, \mathbf{r}_0, s), \end{aligned} \quad (6.7b)$$

where the bond function $g(\mathbf{r})$ naturally emerges to specify the one-step distribution. It is currently a simple Gaussian function because the BS model is adopted. The complementary function $q^\dagger(\mathbf{r}, \mathbf{r}_1, s)$ satisfies essentially the same equation except that $s + \Delta s$ on the left-hand side is replaced by $s - \Delta s$.

The two-point partial partition functions are rarely used in the actual SCFT calculation [117], and it is customary to use the following one-point partial partition functions,

$$q(\mathbf{r}, s) \equiv \frac{1}{(a^2 N)^{3/2}} \int d\mathbf{r}_0 q(\mathbf{r}, \mathbf{r}_0, s), \quad (6.8a)$$

$$q^\dagger(\mathbf{r}, s) \equiv \frac{1}{(a^2 N)^{3/2}} \int d\mathbf{r}_1 q^\dagger(\mathbf{r}, \mathbf{r}_1, s), \quad (6.8b)$$

with the naturally determined initial conditions $q(\mathbf{r}, 0) = q^\dagger(\mathbf{r}, 1) = 1$. One can directly confirm that these functions satisfy the same evolution equation as the two-point partial partition functions. Here is a summary of the process of calculating the unknown $q(\mathbf{r}, s + \Delta s)$ from the known $q(\mathbf{r}, s)$,

$$q^*(\mathbf{r}) = \exp\left(-\frac{w(\mathbf{r})}{2N}\right) q(\mathbf{r}, s), \quad (6.9a)$$

$$q^{**}(\mathbf{r}) = \int d\mathbf{R} g(\mathbf{R}) q^*(\mathbf{r} - \mathbf{R}), \quad (6.9b)$$

$$q(\mathbf{r}, s + \Delta s) = \exp\left(-\frac{w(\mathbf{r})}{2N}\right) q^{**}(\mathbf{r}). \quad (6.9c)$$

The evolution of $q^\dagger(\mathbf{r}, s)$ follows the same equations except that now s is decreasing.

Eq. (6.9) looks slightly different from the familiar form found in the discrete chain SCFT literature [93,101,112,114,116], but it produces the same results because the physical description is the same as explained below. As have been followed, the formal derivation of the integral equation (6.9) requires some algebra, but once it is established, its physical meaning is not so difficult to understand. Lets assume that the sN th segment is shown at the left end of the chain in figure 6-3 (a) marked by the first purple line, and its unnormalized probability is given by the partition function $q(\mathbf{r}, s)$. One half-segment is positioned at \mathbf{r} , and the exponential function in Eq. (6.9a) is the proper Boltzmann factor accounting for the probability increase or decrease due to the half-segment. Then, the propagation of one random step is calculated by the integral

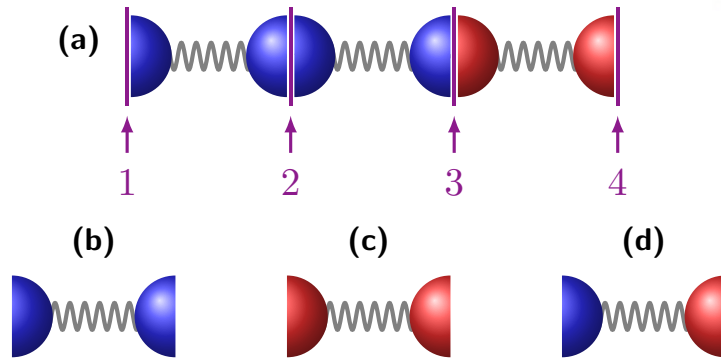


Figure 6-3: (a) Schematic description of the partition function calculation for the positions $1 \rightarrow 2 \rightarrow 3 \rightarrow 4$. At position 3, $s = f$ and the segment type switches from A (blue) to B (red). Description of (b) A evolution and (c) B evolution required for the process of (a). (d) A possible alternative choice, half-A and half-B evolution.

of Eq. (6.9b), where the step distribution is given by the function $g(\mathbf{r})$. Now we are at the $(s + \Delta s)N$ th segment marked by the second purple line in figure 6-3 (a), and \mathbf{r} represents its current position. The Boltzmann factor for the new half-segment is multiplied in Eq. (6.9c). In this way, the three equations calculate the partial partition function evolution from the midpoint of sN th segment to the midpoint of $(s + \Delta s)N$ th segment.

In this process, by using $w_A(\mathbf{r})$ in both Eqs. (6.9a) and (6.9c), the “A evolution” shown in figure 6-3 (b) is applied. After s crosses f , $w_B(\mathbf{r})$ must be used in both Eqs. (6.9a) and (6.9c) which makes the “B evolution” shown in figure 6-3 (c). Later, when the $N - 1$ bond model is adopted, there is no a half-A and half-B segment in the modeling process. In this case, one bond inevitably connects an A segment to a B segment, and a special building block shown in figure 6-3 (d) becomes necessary. For this step, $w_A(\mathbf{r})$ and $w_B(\mathbf{r})$ must be used alternatively in Eqs. (6.9a) and (6.9c), depending on the s evolution direction.

In previous SCFT researches using the discrete chain mode [101,112,114,116], they calculate the evolution of partial partition function from one full-segment to the next full-segment by accounting Boltzmann weight for the field acting on a full-segment, and this causes the shape difference of the recursive integral. In this algebraic formulation, the use of half-segments makes the implementation of both real space and pseudo-spectral methods simpler and the resulting equations are similar to the standard SCFT as shown later.

One of the primary advantages of the discrete chain SCFT is that after the derivation of the three-step integral equations, various types of bonds can be implemented without repeating all the algebraic derivations. As long as each step is independent of the previous step, the entire properties of the bond are contained in the shape of $g(\mathbf{r})$, and it is all needed to vary. For example, when using the freely-jointed bond instead of the spring bond, the proper bond function is

$$g(\mathbf{r}) = \frac{\delta(|\mathbf{r}| - a)}{4\pi a^2} . \quad (6.10)$$

After the calculation of the partial partition functions, the densities of A and B type segments can be calculated, which are defined by the formal ensemble average of Eq. (6.3). Fortunately, it does not required to perform the complicated multivariable integrals for the ensemble average, because the following simple summations and integral provide efficient density calculation. The A and B segment densities in the system are

$$\phi_A(\mathbf{r}) = \sum_{\alpha} \langle \hat{\phi}_{\alpha,A}(\mathbf{r}) \rangle = \frac{V}{NQ} \sum'_{s \in \{0, \dots, f\}} q(\mathbf{r}, s) q^{\dagger}(\mathbf{r}, s) , \quad (6.11a)$$

$$\phi_B(\mathbf{r}) = \sum_{\alpha} \langle \hat{\phi}_{\alpha,B}(\mathbf{r}) \rangle = \frac{V}{NQ} \sum'_{s \in \{f, \dots, 1\}} q(\mathbf{r}, s) q^{\dagger}(\mathbf{r}, s) , \quad (6.11b)$$

where $V = n_p N \rho_0^{-1}$ is the system volume, and the total partition function Q is evaluated from the partial partition functions as follows:

$$Q[w] = \int d\mathbf{r} q(\mathbf{r}, s) q^{\dagger}(\mathbf{r}, s) . \quad (6.12)$$

For more detailed proof of Eqs. (6.11) and (6.12), see appendix E.

Regarding the SCFT formulation of the $N - 1$ bond model which is another major tool in this study, it requires only a few modifications to the above equations. For simplicity, consider the situation of figure 6-2 (a) with N segments and $N - 1$ bonds without any color split segments by choosing an integer fN . Fortunately, switch between the models does not require any complicated modification, and the idea of figure 6-3, calculating the evolution from the midpoint of one segment to the midpoint of the next segment, can be still utilized regardless of the chain model. When the $N - 1$ bond model is used, the main difference is the initial conditions of the partial partition functions,

$$q(\mathbf{r}, 0) = \exp\left(-\frac{w_A(\mathbf{r})}{2N}\right) , \quad (6.13a)$$

$$q^{\dagger}(\mathbf{r}, 1) = \exp\left(-\frac{w_B(\mathbf{r})}{2N}\right) . \quad (6.13b)$$

With these initial conditions, Eq. (6.9) can be used for the evolution of $q(\mathbf{r}, s)$. Note that at the moment s is crossing f , the evolution of figure 6-3 (d) must be applied which requires an alternative use of $w_A(\mathbf{r})$ and $w_B(\mathbf{r})$ inside the exponential functions. After the partial partition functions are calculated, the A and B segment densities can be obtained by the following equation in which non-primed summations are now adopted,

$$\phi_A(\mathbf{r}) = \frac{V}{NQ} \sum_{s \in \{0, \dots, f - (1-f)\Delta s\}} q(\mathbf{r}, s) q^{\dagger}(\mathbf{r}, s) , \quad (6.14a)$$

$$\phi_B(\mathbf{r}) = \frac{V}{NQ} \sum_{s \in \{f + f\Delta s, \dots, 1\}} q(\mathbf{r}, s) q^{\dagger}(\mathbf{r}, s) , \quad (6.14b)$$

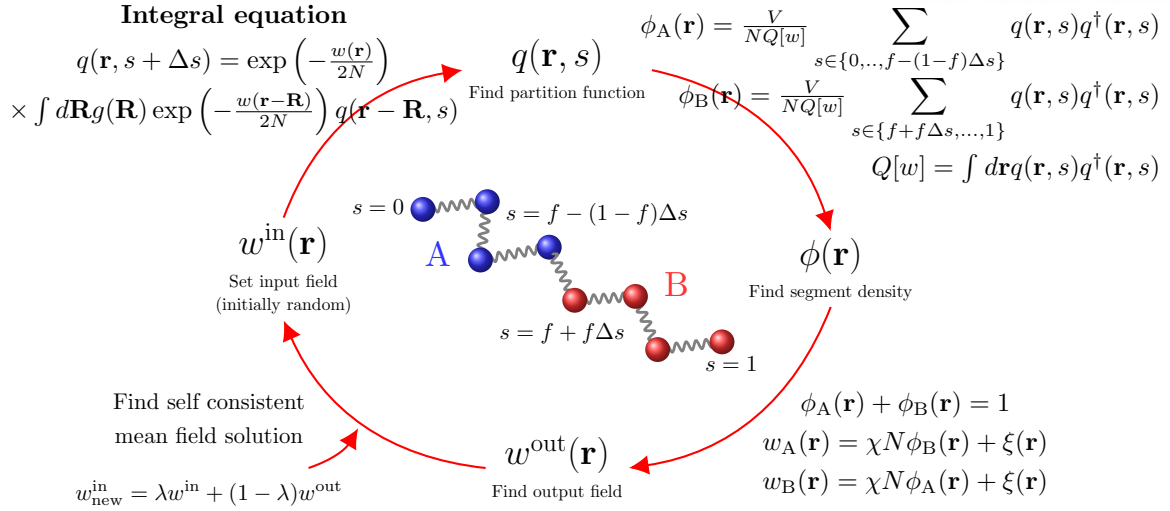


Figure 6-4: Problem solving strategy of the discrete chain SCFT adopting $N - 1$ bond model.

where $f - (1 - f)\Delta s$ indicates the point of A segment just before the junction of the chain, and the point $f + f\Delta s$ corresponds to the B segment just after the junction.

Now all the partition function related equations of the discrete chain SCFT are presented, and the remaining task is to find the self-consistently determined potential fields. By applying the field transformation and the saddle point approximation which remains essentially the same as those of the standard SCFT [64, 93], the self-consistent fields are given as

$$w_A(\mathbf{r}) = \chi N \phi_B(\mathbf{r}) + \xi(\mathbf{r}) , \quad (6.15a)$$

$$w_B(\mathbf{r}) = \chi N \phi_A(\mathbf{r}) + \xi(\mathbf{r}) , \quad (6.15b)$$

where χ is the interaction parameter, and $\xi(\mathbf{r})$ is the pressure field enforcing incompressibility which acts equivalently on both A and B segments.

To find the self-consistent solution to these equations, it is common to use an iterative method as summarized in figure 6-4 for the $N - 1$ bond model. Starting from the input fields $w_A^{\text{in}}(\mathbf{r})$ and $w_B^{\text{in}}(\mathbf{r})$, iteration continues until the output fields essentially become the same as the input fields. After the final self-consistent mean field solution is obtained, the free energy of the system is calculated by the following equation,

$$\frac{F}{n_p k_B T} = - \ln \left(\frac{Q}{V} \right) + \frac{1}{V} \int d\mathbf{r} \left(\chi N \phi_A(\mathbf{r}) \phi_B(\mathbf{r}) - w_A(\mathbf{r}) \phi_A(\mathbf{r}) - w_B(\mathbf{r}) \phi_B(\mathbf{r}) \right) . \quad (6.16)$$

The last subject of this section is the finite-range interaction between the nonbonded segments. The standard SCFT formulation assumes that a segment is point-like and the interaction between A and B type segments is counted only when they make direct contact. One advantage of the discrete chain SCFT is that it can naturally adopt an interaction potential which has a

finite-range related to the bond length [116]. With this modification, the self-consistent field is determined as

$$w_A(\mathbf{r}) = \xi(\mathbf{r}) + \chi N \int d\mathbf{R} u(\mathbf{R}) \phi_B(\mathbf{r} - \mathbf{R}) , \quad (6.17a)$$

$$w_B(\mathbf{r}) = \xi(\mathbf{r}) + \chi N \int d\mathbf{R} u(\mathbf{R}) \phi_A(\mathbf{r} - \mathbf{R}) . \quad (6.17b)$$

The function $u(\mathbf{r})$ represents the strength of the interaction between A and B segments separated by \mathbf{r} , and it naturally emerges from the interaction energy adopting finite-ranged AB interaction [118] as follows

$$\frac{U}{n_p k_B T} = \frac{\chi N}{V} \int d\mathbf{r} d\mathbf{r}' u(\mathbf{r} - \mathbf{r}') \phi_A(\mathbf{r}) \phi_B(\mathbf{r}') , \quad (6.18a)$$

$$\int d\mathbf{r} u(\mathbf{r}) = 1 . \quad (6.18b)$$

It is natural to assume that $u(\mathbf{r})$ is a simple Gaussian function which only depends on the magnitude of \mathbf{r} . To recover the contact interaction model, all we need to do is to set $u(\mathbf{r}) = \delta(\mathbf{r})$. With the presence of the finite-range interaction, the free energy is now obtained by simply replacing $\phi_A(\mathbf{r})$ in the first term inside the integration of Eq. (6.16) by $\phi'_A(\mathbf{r}) \equiv \int d\mathbf{R} u(\mathbf{R}) \phi_A(\mathbf{r} - \mathbf{R})$.

7

Pseudo-spectral Method

In this chapter, I will briefly introduce the pseudo-spectral method which is commonly used in the research using the standard SCFT. Then, I will discuss applicability of the pseudo-spectral method for the discrete chain SCFT calculation. More detailed issues concerning its numerical implementation follow in the next chapter.

7.1 Introduction

In the standard SCFT, the solutions of most polymer problems are obtained by applying some numerical approximations to the modified diffusion equation (6.1). The numerical methods developed so far can be categorized into three groups: i) real space method [66, 72, 73, 94, 119–126], ii) spectral method [64, 95], and iii) pseudo-spectral method [66, 72, 127–132]. Nowadays, real space and pseudo-spectral methods are mainly used to find the nanoscale morphology of a given polymeric system.

To obtain a numerical solution using the real space method, it is common to divide the system volume with M_1 , M_2 , and M_3 grids in each direction, and the Laplacian is approximated by the finite difference method (FDM) or finite volume method (FVM) incorporated with Crank-Nicolson method [66, 133] or its approximation, alternating direction implicit (ADI) method [66, 72, 125, 133]. In the real space method, the unknown function $q(\mathbf{r}, s + \Delta s)$ is calculated from the known function $q(\mathbf{r}, s)$ where Δs is the discretized step size in s direction. The Crank-Nicolson method is known to be slow, but when the ADI method is adopted, a fast calculation is possible with $O(M)$ time where $M = M_1 M_2 M_3$ is the spatial grid number.

In the pseudo-spectral method of the standard SCFT, the spatial discretization is essentially the same as the above description. The one-step advance of the partial partition function $q(\mathbf{r}, s)$ in s direction is now calculated by the following three-step operator splitting method [66, 127,

128],

$$q^*(\mathbf{r}) = \exp\left(-\frac{\Delta s}{2}w(\mathbf{r})\right) q(\mathbf{r}, s), \quad (7.1a)$$

$$q^{**}(\mathbf{r}) = \exp\left(-\frac{\Delta s}{6}\nabla^2\right) q^*(\mathbf{r}), \quad (7.1b)$$

$$q(\mathbf{r}, s + \Delta s) = \exp\left(-\frac{\Delta s}{2}w(\mathbf{r})\right) q^{**}(\mathbf{r}). \quad (7.1c)$$

Note that it is implicitly assumed that $w(\mathbf{r})$ is properly chosen according to the s value. The nontrivial step is Eq. (7.1b) where a rescaled Laplacian operator appears in the exponential function.

Instead of calculating this in the real space, the pseudo-spectral method performs Fourier and inverse Fourier transforms before and after this step, respectively. As a consequence, the differentiation in the real space is converted to a simple multiplication in the Fourier space. For the pseudo-spectral method, the most time-consuming operation is the Fourier and inverse Fourier transforms, and the required time for the one-step advance in s direction is $O(M \log M)$ when fast Fourier transform (FFT) is used. With the help of modern FFT packages such as FFTW [134], the actual calculation speed of the pseudo-spectral method can be as fast as that of the real space calculation adopting the ADI method.

7.2 Implementation in Discrete Chain SCFT

Before examining the applicability of the pseudo-spectral method in the discrete chain SCFT, it is the proper time to discuss the speed of real space calculation of the recursive integral equation (6.9b). The shape of the integral implies that one three-dimensional integral is necessary for every point \mathbf{r} , and the one-step evolution requires $O(M^2)$ operations where M is the spatial grid number; thus, the real space calculation of discrete chain SCFT is inevitably slower than the standard SCFT whose time complexity can reduce to $O(M)$ or $O(M \log M)$ with the adoption of the fastest algorithms. If an appropriate cutoff is applied to the bond function $g(\mathbf{r})$, the performance can be greatly enhanced because only a small part of the total volume for each \mathbf{R} integral is now used. Nevertheless, the real space calculation of discrete chain SCFT cannot compete with the standard SCFT in terms of speed, and it is not a practical tool for the simulation of three-dimensional polymeric systems.

One suggestion to overcome this problem is the use of pseudo-spectral method as verified in the standard SCFT research. Even though it is natural to conceive the adoption of the pseudo-spectral method for the evaluation of the recursive equations [93, 116], the practicality of the algorithm has not been verified in that no known research has implemented this technique for the study of real polymer systems. The idea of the pseudo-spectral calculation of the integral

7.2 Implementation in Discrete Chain SCFT

seems to be straightforward, but there are some troublesome issues found in the implementation of the pseudo-spectral method, and the details will be discussed in the next section.

The formulation developed so far is carefully designed for the future adoption of the numerical algorithms; the evolution of the partition function calculated by the three steps displayed in Eq. (6.9) has a very similar structure to that of the pseudo-spectral or the operator splitting real space methods [66, 135] of the standard SCFT. The most time-consuming step of the real space calculation is the integral of Eq. (6.9b), and because it has the shape of a convolution integral, one natural suggestion is to perform this calculation in the Fourier space where the convolution integral becomes a simple multiplication,

$$\tilde{q}^{**}(\boldsymbol{\xi}) = \tilde{g}(\boldsymbol{\xi})\tilde{q}^*(\boldsymbol{\xi}) . \quad (7.2)$$

In this study, I use the notation that the tilde on a variable denotes its Fourier transform or Fourier cosine transform. The Fourier transform is defined in the following way,

$$\tilde{f}(\boldsymbol{\xi}) \equiv \int d\mathbf{r} f(\mathbf{r}) \exp(-2\pi i \boldsymbol{\xi} \cdot \mathbf{r}) . \quad (7.3)$$

For the BS model, the Fourier transform of the Gaussian distribution function is another Gaussian in the $\boldsymbol{\xi}$ space,

$$\tilde{g}(\boldsymbol{\xi}) = \exp\left(-\frac{2}{3}\pi^2 a^2 |\boldsymbol{\xi}|^2\right) . \quad (7.4)$$

In its numerical implementation using M spatial grids, I use the discrete Fourier transform (DFT) which can be performed by $O(M \log M)$ operations, and this is essentially the time complexity of the single evolution step. Considering that the Fourier and inverse Fourier transforms are performed just before and after Eq. (6.9b), researchers accustomed to the standard SCFT would recall the pseudo-spectral method of it. Indeed, with a special combination of the N bond model and BS model, the discrete chain SCFT calculation becomes equivalent to the calculation of the standard SCFT using the standard pseudo-spectral method with $\Delta s = 1/N$.

8

Numerical Implementation

8.1 Bond Function Discretization

Since space must be discretized in the numerical calculation, all the real space functions are represented by a set of discrete points. In this approach, Fourier transform must be replaced by its discrete version, DFT. However, this conversion is not a trivial task because naïve discretization of the bond function $g(\mathbf{r})$ is prone to amplify errors in the calculation of the partition function, and material conservation is known to be an important issue [66].

I start implementing the numerical scheme using a simple three-dimensional box of size L_x , L_y , and L_z , and each direction is discretized by Δx , Δy , and Δz so that an integer vector $\mathbf{i} = (i, j, k)$ represents the grid point on the position $\mathbf{r}_i \equiv (i\Delta x, j\Delta y, k\Delta z)$. The discretized partition function value at each point is $q_i \equiv q_{i,j,k}$ where each index starts from 0, and the maximum values of i , j , and k are $I \equiv L_x/\Delta x$, $J \equiv L_y/\Delta y$, and $K \equiv L_z/\Delta z$, respectively, when the periodic or Neumann boundary conditions are applied in all directions.

The spatial integral is now evaluated by a weighted summation,

$$\int d\mathbf{r} f(\mathbf{r}) \rightarrow \sum_{\mathbf{r}_i} f(\mathbf{r}_i) \Delta V_i, \quad (8.1)$$

where ΔV_i is the volume of the i th cell. For equally spaced Cartesian grids, most of ΔV_i are $\Delta V \equiv \Delta x \Delta y \Delta z$, but factors 1/2, 1/4, and 1/8 are multiplied when the point (i, j, k) is at the planar, line, and vertex boundaries, respectively.

Lets make a careful thought about the discretization of the bond function $g(\mathbf{r})$ using the one-dimensional BS model as an example. For the one-dimensional problem, I will always consider a system with z dependent functions, assuming symmetry in x and y directions. Now the required job is to discretize the Gaussian distribution function $g(z) = (3/2\pi a^2)^{1/2} \exp(-3z^2/2a^2)$. Because the space is discretized by Δz , one is tempted to directly use $g_k \equiv g(k\Delta z)$ as the discrete distribution function, and try to perform DFT of them. With this choice, however, the weighted summation $\sum g_k \Delta V_k$ is not exactly equal to 1, which means that the total probability of one step is not equal to 1. Another issue is the tail of the distribution function. In principle, $g(z)$

8.1 Bond Function Discretization

is defined at $z \in (-\infty, \infty)$, but it is needed to set $g(z) = 0$ for large enough $|z|$ to provide appropriate cutoffs for the integral of Eq. (6.9b). Let us accept a very loose condition for the time being, $g(z) = 0$ for $|z| > L_z$. For the three-dimensional distribution function, x and y directional cutoffs are given accordingly.

Here is a simple solution to both issues, regardless of the dimensionality of the system. In the previous report of Yong et al. [66], it was shown that the probability or material conservation and the constant RMS step size are two important rules one must keep in the numerical SCFT calculation. Such a consideration suggests us to adopt a discrete distribution function g_i satisfying the following two equations,

$$\sum g_i \Delta V_i = 1 , \tag{8.2a}$$

$$\sum \mathbf{r}_i^2 g_i \Delta V_i = a^2 . \tag{8.2b}$$

The first equation guarantees the probability conservation, while the second equation is for the fixation of the RMS step size in the discrete calculation. It is a relatively easy task to slightly modify the height and width of the Gaussian function of the BS model to satisfy these two equations, and it has been shown that such a slight deviation does not create any noticeably undesirable side effect. Thus, I always use Eq. (8.2) regardless of the choice of the bond model and the distribution function. After obtaining the discretized values of the modified distribution function in real space, DFT is applied, and simple multiplication of Eq. (7.2) is performed in the Fourier space without violating the mass conservation condition.

The implementation of the FJC model is a more challenging task because of the delta function shaped $g(\mathbf{r})$. At least its one-dimensional version is easier to construct to satisfy Eq. (8.2) because the bond function $g(z)$ reduces to a step function [101],

$$g(z) = \begin{cases} 1/2a & \text{if } |z| \leq a \\ 0 & \text{otherwise} \end{cases} . \tag{8.3}$$

Because of its finite range, this model is easier to implement compared to the one-dimensional BS model, and relatively faster calculation of Eq. (6.9b) is possible by making cutoffs at $z = \pm a$. However, the probability conservation error may be significant if a naïve discretization of the step function, $g_k \equiv g(k\Delta z)$, is chosen. As suggested earlier for the Gaussian function, by making a slight modification to the step height and width, Eq. (8.2) can be easily matched, and this is the recommendable way to implement the pseudo-spectral method in the discrete chain SCFT.

The true challenge is the full three-dimensional calculation of the FJC model. In this case, the Dirac delta function in $g(\mathbf{r})$ makes the spatial discretization in real space rather difficult. Its direct implementation in real space is not recommendable, and this issue will be discussed in the next section.

8.2 Three-dimensional FJC Model

In the previous section, the implementation of the Dirac delta function shaped $g(\mathbf{r})$ was a difficult task for the three-dimensional spatial grid. At practically no grid point $(i\Delta x, j\Delta y, k\Delta z)$, the function value is nonzero, but it is required to assign some values on the grids to represent the delta function while satisfying Eq. (8.2), and do not forget that its Fourier transform is needed for the pseudo-spectral calculation. Fortunately, at least part of these issues disappear when starting the discretization in the discrete Fourier space because the three-dimensional Fourier transform of the FJC bond function is analytically calculated as [93, 116]

$$\tilde{g}(\boldsymbol{\xi}) = \text{sinc}(2|\boldsymbol{\xi}|a) \equiv \frac{\sin(2\pi|\boldsymbol{\xi}|a)}{2\pi|\boldsymbol{\xi}|a}, \quad (8.4)$$

This is a smooth function in the Fourier space, and it can be easily discretized in the discrete Fourier space. For example, when Neumann boundary condition is used, discrete cosine transform (DCT) is naturally adopted, and the $\tilde{g}_{\mathbf{i}}$ can be taken by sampling of $\tilde{g}(i/2L_x, j/2L_y, k/2L_z)$, which becomes

$$\tilde{g}_{\mathbf{i}} = \frac{1}{8\Delta V} \text{sinc} \left(a \sqrt{\left(\frac{i}{L_x}\right)^2 + \left(\frac{j}{L_y}\right)^2 + \left(\frac{k}{L_z}\right)^2} \right), \quad (8.5)$$

where the range of each index is from 0 to its maximum value, I , J , or K . When the boundary conditions are periodic, DFT is now adopted, and the $\tilde{g}_{\mathbf{i}}$ can be obtained by sampling of $\tilde{g}(i/L_x, j/L_y, k/L_z)$, with the additional consideration on its periodic property. Thus,

$$\tilde{g}_{\mathbf{i}} = \frac{1}{\Delta V} \text{sinc} \left(2a \sqrt{\left(\frac{i'}{L_x}\right)^2 + \left(\frac{j'}{L_y}\right)^2 + \left(\frac{k'}{L_z}\right)^2} \right), \quad (8.6)$$

where $i' = i$ if $i < I/2$, and $i' = i - I$ otherwise. j' and k' are defined similarly. In this paper, we show our calculations using DCT adopting Neumann boundary conditions.

When the entire calculations are performed in the Fourier space, it is an attractive idea to use this $\tilde{g}_{\mathbf{i}}$ function. For example, in a low molecular weight diblock copolymer research using spectral method, Matsen has used the sinc function for the evaluation of the convolution integral in the Fourier space for the purpose of obtaining the phase diagram [116].

However, the real space function obtained by performing inverse DCT of Eq. (8.5) is somewhat unsatisfactory in terms of the reproducibility of the original function and non-negativity of the probability. Figures 8-1 (a) and 8-1 (b) exhibit the reconstructed delta function distribution of Eq. (6.10) on the two planes, $z = 0$ and $z = 4a/5$, for the case of $\Delta x = \Delta y = \Delta z = a/10$. As expected, figure 8-1 (a) shows that $g_{\mathbf{i}}$ is highly peaked at the grid cells where the circle $x^2 + y^2 = a^2$ passes. The non-trivial feature is that the probability is also distributed to the cells which do not contain the circle. What makes things worse is that cells far from the circle exhibit finite amplitudes and sometimes $g_{\mathbf{i}}$ even becomes slightly negative. The amplitude plot for

the plane $z = 4a/5$ (figure 8-1 (b)) shows a similar behavior except that now $x^2 + y^2 = (3a/5)^2$ is the circle of peak amplitudes. One may worry that the negative g_i or negative probability may cause a catastrophe when using the FJC model, but the aforementioned research suggests that this local probability anomaly does not cause a serious problem [116]. The strong peak averages out all the negative variables in the long run, and the final segment density always becomes positive for reasonable choices of parameters.

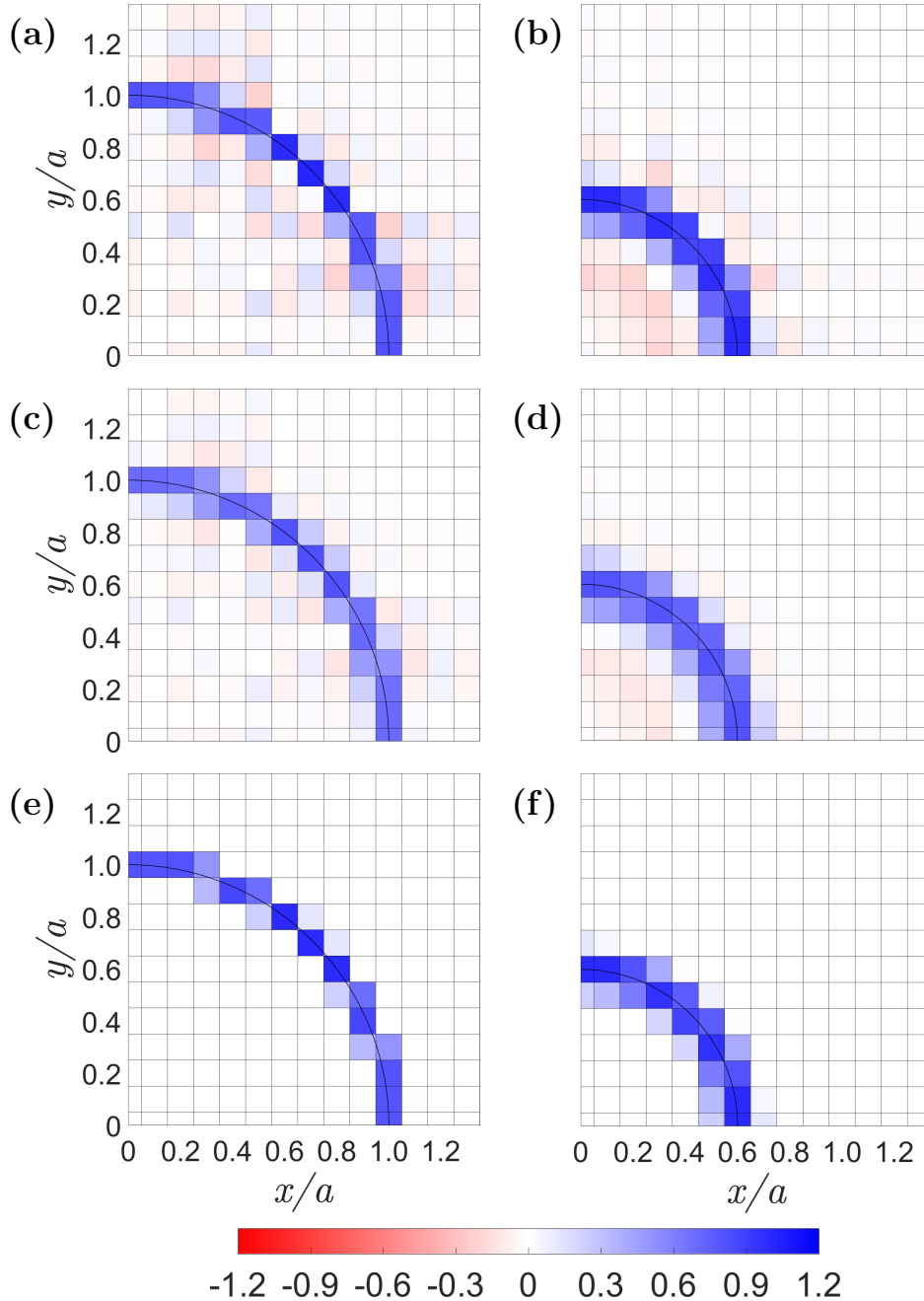


Figure 8-1: (a) $g_{i,j,0}$ and (b) $g_{i,j,8}$ of the FJC model obtained by Eq. (8.5) for the case of $\Delta x = \Delta y = \Delta z = a/10$. (c) $g_{i,j,0}$ and (d) $g_{i,j,8}$ obtained by Eq. (8.8) after using only $n_x = n_y = n_z = 0$. (e) and (f) are the results with the summation up to $n_x = n_y = n_z = \pm 5$.

8.2 Three-dimensional FJC Model

I may instead suggest an alternative method which is based on an intuitive idea. It is obvious that $g(i\Delta x, j\Delta y, k\Delta z)$ cannot be a good candidate of $g_{\mathbf{i}}$ for the FJC model, but the average of $g(\mathbf{r})$ within the cell can be a valid candidate,

$$g_{\mathbf{i}} \equiv \frac{1}{\Delta V} \int_{-\Delta z/2}^{\Delta z/2} \int_{-\Delta y/2}^{\Delta y/2} \int_{-\Delta x/2}^{\Delta x/2} g(i\Delta x - x', j\Delta y - y', k\Delta z - z') dx' dy' dz'. \quad (8.7)$$

Applying this idea to Eq. (6.10), $g_{\mathbf{i}}$ of Eq. (8.7) now becomes the surface area of a sphere of radius a contained within the \mathbf{i} th cell divided by $4\pi a^2$. Even though this definition is conceptually clear, the actual calculation of the integral is not a trivial task.

Fortunately, the sampling theory of the discrete time Fourier transform (DTFT) provides an efficient method to calculate the DCT of Eq. (8.7) (see appendix F for the detail). Using this method, the $\tilde{g}_{\mathbf{i}}$ of the FJC bond function becomes

$$\tilde{g}_{\mathbf{i}} = \frac{1}{8\Delta V} \sum_{n_x, n_y, n_z} \text{sinc} \left(a \sqrt{\left(\frac{i - 2n_x I}{L_x} \right)^2 + \left(\frac{j - 2n_y J}{L_y} \right)^2 + \left(\frac{k - 2n_z K}{L_z} \right)^2} \right) \times \text{sinc} \left(\frac{i - 2n_x I}{2I} \right) \text{sinc} \left(\frac{j - 2n_y J}{2J} \right) \text{sinc} \left(\frac{k - 2n_z K}{2K} \right), \quad (8.8)$$

where each of the n_x , n_y , and n_z summation range is from $-\infty$ to ∞ , and the inverse DCT of this expression provides us a valid $g_{\mathbf{i}}$. The convergence of this summation is surprisingly good. Figures 8-1 (c) and 8-1 (d) exhibit $g_{\mathbf{i}}$ obtained only by using $n_x = n_y = n_z = 0$ term, and they already look better than figures 8-1 (a) and 8-1 (b). The results with the summation up to $n_x = n_y = n_z = \pm 5$ are shown in figures 8-1 (e) and 8-1 (f). Cells with negative $g_{\mathbf{i}}$ practically disappear, and the results are almost the same as the spherical surface fraction within the cell. One last note is that the transformed $g_{\mathbf{i}}$ in the real space does not exactly satisfy Eq. (8.2), and thus slight adjustments are recommended for its practical implementation. The easy way is to make a small modification to the function $\tilde{g}_{\mathbf{i}}$ in Eq. (8.8) to satisfy Eq. (8.2).

Discretization of a quickly varying function results in a significant loss of high frequency modes. Averaging within the cell using Eq. (8.7) can be viewed as a filtering process eliminating high frequency mode of bond function, and it is the reason why the approach has been successful for the FJC bond function. This filtering approach can be easily applied to other bond functions whose analytic Fourier transforms are known, and it is expected that a better spatial discretization is achievable especially when the bond function is a quickly varying function. All we need to do is to replace the first sinc function of Eq. (8.8) with the known Fourier transform of the bond function while leaving the last three sinc functions.

In the development stage of discrete chain SCFT, the real space method [101] was naturally used, and the full spectral method [116] was adopted later for the purpose of creating the block copolymer phase diagram. Slow speed was not a crucial issue in the development stage, but for a

new theoretical framework to be widely accepted, it is important to show that a fast calculation is possible, and the pseudo-spectral method provides the perfect solution.

I perform a speed test of the three-dimensional discrete chain SCFT pseudo-spectral method using a single core of Xeon Gold 6132 CPU, and the DCTs are performed with the FFTW package [134]. For the test system, I take the diblock copolymers with parameters $N = 50$, $\chi N = 25$, and $f = 0.2$, which is expected to create a body-centered-cubic phase. When the FJC bond function and $32 \times 32 \times 32$ grid box are used, it takes 0.2 seconds per 1 iteration, and 11 seconds is enough to obtain the final morphology. For a larger system with $256 \times 256 \times 256$ grid box, it takes 112 seconds per 1 iteration, and 93 minutes is required for the whole calculation. In short, the pseudo-spectral method of discrete chain SCFT is as fast as any known real space or pseudo-spectral method implementations of the standard SCFT.

8.3 Boundary Condition Issues

For the actual implementation of the pseudo-spectral method in the discretized world, certain boundary conditions must be chosen, and there are a few subtle physical and numerical issues that must be cleared for their proper implementation. When the boundary condition of the $g_{\mathbf{i}}$ family is periodic with period L_x , L_y , and L_z in each direction, to apply the convolution theorem, it can be assumed that the discrete bond function $g_{\mathbf{i}}$ has the same periodicity even though $g(\mathbf{r})$ is in principle a non-periodic function. One can easily check that such a modification does not do any harm for the integral of Eq. (6.9b), as long as one period of convolution integral is performed in all directions. To make $g_{\mathbf{i}}$ periodic and for the accuracy of the calculation, it must slightly deviate from $g(i\Delta x, j\Delta y, k\Delta z)$ while satisfying Eq. (8.2).

The case with the Neumann boundary is somewhat more complicated. Under the condition that $g(\mathbf{r})$ has the reflection symmetry with respect to $x = 0$, $y = 0$, and $z = 0$ planes, which is usually true, the discrete version of Eq. (7.2), $\tilde{q}_{\mathbf{i}}^{**} = \tilde{g}_{\mathbf{i}}\tilde{q}_{\mathbf{i}}^*$, is valid with the interpretation that the tilde on a variable now represents its DCT. In other words, all we need to do is to define $g_{\mathbf{i}}$ in the region $0 \leq i \leq I$, $0 \leq j \leq J$, and $0 \leq k \leq K$, and perform its DCT.

One can easily imagine another common situation, the Dirichlet boundary condition, and it is sometimes adopted in the standard SCFT calculation for the modeling of the polymer-air or polymer-substrate interface. However, it is not a trivial task to model these boundaries in the discrete chain SCFT calculation. When using a Dirichlet boundary condition in solving a differential equation, it is expected that the function values are zero at the boundary. In the pseudo-spectral method, the natural strategy is to use a discrete sine transform (DST) for the $q(\mathbf{r})$ family. Even though such a calculation is numerically possible, it is not a recommendable strategy for the modeling of interfaces in the discrete chain SCFT as explained below.

Let us consider a situation that there exists a wall at $z = 0$ so that no polymers exist at $z < 0$. When no additional interaction is imposed, it is naturally called as a neutral wall. However, one must be careful that the presence of the wall reduces the entropy of polymer chains near the wall, which creates an effective repulsion [100, 101]. In the discrete chain model, the correct way to represent the non-existence of segments beyond the wall is to let the partition function vanish whenever a segment crosses the wall. It can be achieved by setting the function value to be zero beyond the boundary wall after each integration of Eq. (6.9b). Earlier researches show that when the field acting on the polymers vanishes, the polymer density at $z = 0$ is exactly $1/N$ of the bulk density [100, 101], which means that only the $N \rightarrow \infty$ limit can be legitimately called the Dirichlet boundary case. In this way, the discrete chain SCFT opens up possibility of a new interesting boundary condition, the neutral boundary, which was not available for the standard SCFT calculation with the Gaussian chain model.

When the neutral boundary condition is chosen, performing the integral of Eq. (6.9b) in the real space is not a particularly complicated process. However, as explained in chapter 7, the

real space calculation in three dimension is very slow, and the pseudo-spectral method is the preferable choice for the discrete chain SCFT. The fact that the DST is not applicable for this problem is a slight disappointment, but the pseudo-spectral method is still a valid approach because all we need to do is to perform the convolution integral after enforcing $q(\mathbf{r}) = 0$ beyond the neutral walls.

To achieve this, the system boundary can be extended beyond the wall by the practical range of the bond function $g(\mathbf{r})$, and $q(\mathbf{r})$ is set to zero in the newly added space. Now the convolution integral of the total system can be performed using DFT or DCT without a problem. After the integral is finished, the extended region is removed and the original system size is restored. Such an algorithm requires an additional computational resource for the extended space, but the whole process of the one-step evolution is guaranteed to be finished in $O(M \log M)$ time, and this is certainly the best strategy of discrete chain SCFT for the two- or three-dimensional system when the neutral boundary condition is chosen. In section 9.2, I will use this method for the analysis of the block copolymer thin film system.

9

Result

9.1 Discrete Chain Behavior in Lamellar Morphology

In this section, I make a few tests of the discrete chain SCFT using lamellar forming symmetric ($f = 0.5$) diblock copolymers adopting various chain models, and the results are compared with those of the standard SCFT. It is important to note that $R_0 \equiv a(N - 1)^{1/2}$ is used for $N - 1$ bond model, and $R_0 \equiv aN^{1/2}$ for the N bond model.

In the standard SCFT, it is known that fine discretization in the s direction is important at high χN , and similar behavior is found in this simulation. Figure 9-1 displays the block copolymer period D and the interfacial width w_I for various chain models [64] at $\chi N = 50$ and 100. For the calculation in this section, 2000 grid points are utilized for the simulation box. The spatial discretization Δz varies according to the box size, and it ranges from $0.0004R_0$ to $0.0008R_0$. Thus, for all the parameters utilized here, there exist enough grid numbers to accurately analyze the behavior of the interfacial width. As expected, all curves converge to the standard SCFT results in the limit $N \rightarrow \infty$, but deviations are not negligible at intermediate N values and there are a few noticeable differences between the models. For the FJC model at $\chi N = 50$, $N = 50$ is enough for D and w_I to reach to the standard SCFT results, but the BS model seems to converge slower so that somewhat higher N is required to see the convergence.

The cases with $\chi N = 100$ exhibit similar trends. For the FJC and SB models, $N = 100$ and 400 are required to confirm the convergence, respectively. Comparing between the segment models, the N bond model shows a slightly better convergence compared to the $N - 1$ bond model, which has the mismatch of the bond number ($N - 1$) and the segment number (N). The observation that the convergence is faster for the FJC model might be a surprise for those who think that the spring-like bond of the BS model makes it closer to the Gaussian chain model.

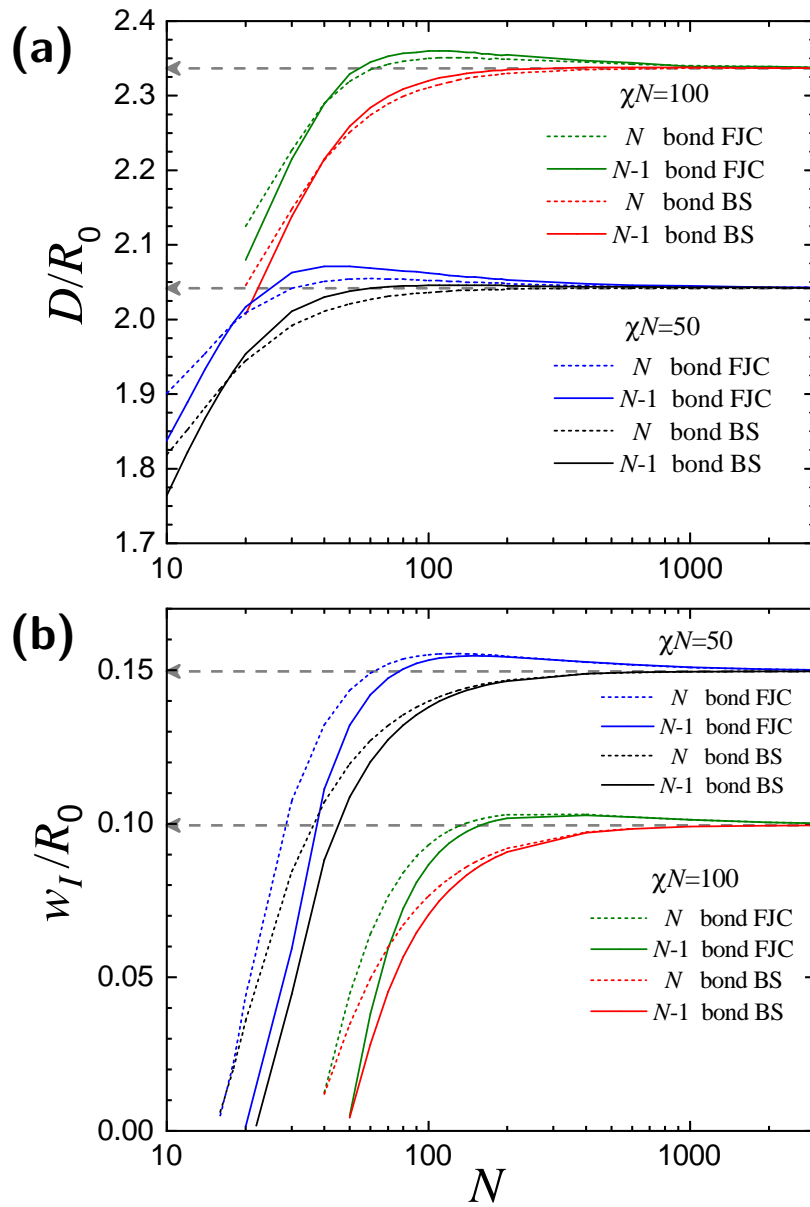


Figure 9-1: (a) Lamellar period D and (b) interfacial width w_I for the discrete chain SCFT of symmetric ($f=0.5$) AB block copolymers with $\chi N = 50$ and 100, as functions of N . The dashed lines are the standard SCFT results using the Gaussian chain model.

9.1 Discrete Chain Behavior in Lamellar Morphology

This issue can be investigated further by analyzing figure 9-2 which extends Matsen's analysis on the $N - 1$ bond FJC model [116] to the other possible models. In this figure, D and w_I for the various chain models are plotted as functions of χN at fixed N . For the lamellar period of $N = 160$ case, the $N - 1$ bond model and N bond model are nearly indistinguishable for both BS and FJC models. The case with $N = 160$ shows that the lamellar period of the FJC models follows the standard SCFT result (dashed line) for χN up to 300, while that of the BS models deviates slightly from the standard SCFT result at such a large χN .

The interfacial width shown in figure 9-2 (b) provides an important hint to understand this behavior. Due to the finite bond size and strong stretching near the AB interface, the A and B segments are essentially segregated at very large χN , and they form a sharp interface. Near this one-dimensional interface, one step of the bond has the Gaussian function shape in the BS model. On the other hand, the step has the shape of Eq. (8.3) in the FJC model, and there is a higher chance for an A segment near the interface to send its random-walking A neighbor beyond the interface and increase the degree of mixing. This residual mixing effect makes the FJC model behave more like the standard SCFT in which infinitely flexible chains easily mix. Because the lamellar period increases at increasing χN to achieve better segregation between A and B blocks, the decrease of the interfacial width works in the direction to shrink the period, which can be confirmed by figure 9-2 (a).

The idea that decrease of the interfacial width for highly stretched chains leads to the period reduction is consistent with the observation of figure 9-1. Surface energy plot in appendix G confirms that the interfacial energy actually decreases with decreasing N at fixed χN , and thus decrease of the interfacial width is the cause of the interfacial energy and the block copolymer period reduction.

The stronger mixing effect of the FJC model also provides an explanation to the observation of a slight overshoot of D and w_I in figure 9-1 at intermediate values of N . In this regime, due to the extra mixing of A and B segments near the interface, the interfacial width of the FJC model (figure 9-1(b)) is slightly wider than the standard SCFT case, which in turn increases the period D slightly to create the overshoot.

Figure 9-2 also shows that, for the shorter chains with $N = 40$, the general behaviors of the models are similar to the $N = 160$ cases except that now D and w_I deviate from the standard SCFT results at a smaller χN . At this N value, let us compare the two choices, the $N - 1$ bond and N bond models. At large enough χN , the width w_I is notably narrower for the $N - 1$ bond model. The shape of the segments displayed in figures 6-2 (a) and 6-2 (b) provides a convincing argument explaining this behavior. Because of the presence of the half-A and half-B segment, mixing of blocks are more significant in the N bond model. The lack of such a segment makes a sharper boundary and a shorter period for the $N - 1$ bond model.

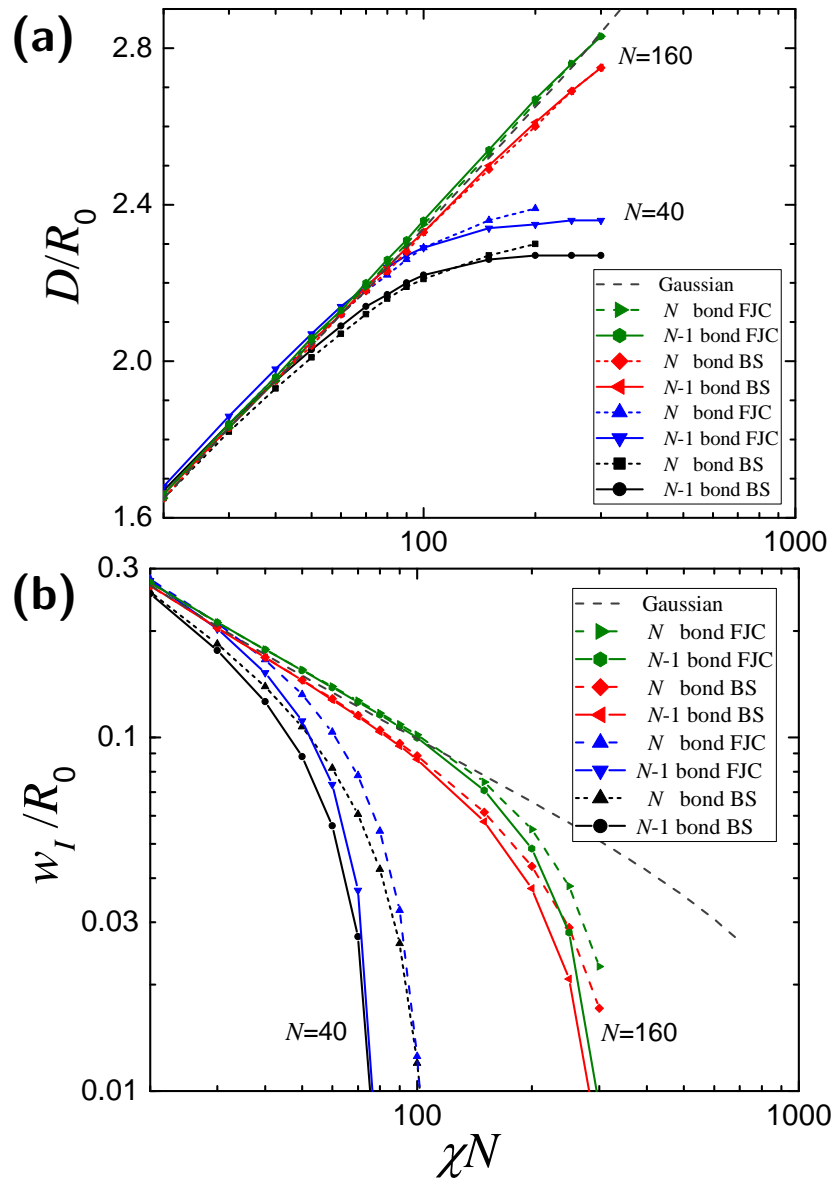


Figure 9-2: Discrete chain SCFT (a) lamellar period D and (b) interfacial width w_I as functions of χN . The dashed lines are the standard SCFT results using the Gaussian chain model.

9.2 Diblock Copolymers in Thin Film

When lamellar forming AB block copolymers are confined in a thin film morphology, the lamellar domains may align parallel or perpendicular to the substrate. In general, when the polymer-substrate or polymer-air surface interaction is preferential to a specific block, surface-parallel lamellae are naturally chosen [136, 137]. For those who wish to create surface-perpendicular lamellae, it is necessary to make a special tuning of the surface property. For example, the surface tensions of PS and poly(methyl methacrylate) (PMMA) are very similar, and PS-*b*-PMMA block copolymers are commonly used for the creation of surface-perpendicular lamellae [138, 139]. The substrate must also be neutralized for the effective control of the lamellar orientation. PS-*r*-PMMA layer [140], self-assembled monolayer [141], and chemically modified graphene layer [142] are often used for the neutralized substrate of PS-*b*-PMMA block copolymers.

There are a few issues concerning the theoretical treatment of the neutralized surface, especially when considering the boundary as a hard impenetrable wall. It is well known that a polymer chain loses its conformational entropy near the wall, but the degree of entropy loss strongly depends on the bond step size and shape [100, 101, 112, 143, 144]. Because of this, the standard SCFT using infinitely flexible Gaussian chains can capture the physics near the hard wall only after adding some extra features such as a gradual density variation [102, 144–147]. Another interesting approach to this problem is the lattice SCFT [103, 104] which has been a branch of the SCFT family since its development stage. By introducing interaction potential which depends on the density at the nearest lattice sites, the preference of the surface-perpendicular morphology over the surface-parallel one has been successfully demonstrated using the lattice SCFT [106, 148].

In this section, I analyze the behavior of freely-jointed block copolymers confined by the neutral walls using two-dimensional discrete chain SCFT adopting finite-range interaction. Let us consider a symmetric ($f = 0.5$) AB block copolymers confined between two neutral walls at $z = 0$ and $z = L_z$ (see figure 9-3 (a)). For the calculation of the surface-perpendicular lamellar morphology, at least two-dimensional calculation must be used. For the following calculation, the x directional size L_x is chosen to be 1/2 times of the bulk period, and the Neumann boundary conditions are adopted in the x direction. The shape of the finite-range interaction function $u(\mathbf{r})$ is chosen as a Gaussian function,

$$u(\mathbf{r}) = \left(\frac{3}{2\pi a^2}\right)^{3/2} \exp\left(-\frac{3\mathbf{r}^2}{2a^2}\right). \quad (9.1)$$

This choice assumes that the effective interaction range is the bond size a , which is a reasonable assumption. For the convenience of the pseudo-spectral method, the actual discrete function has a cutoff at $|\mathbf{r}| = 2a$, beyond which $u_{\mathbf{i}} = 0$, and it is normalized to satisfy Eq. (8.2) with $g_{\mathbf{i}}$ being replaced by $u_{\mathbf{i}}$. For the bond distribution function $g_{\mathbf{i}}$, two-dimensional Fourier transform of the FJC bond function is required. I adopt the DCT expression, Eq. (8.8), after

dropping the terms for y direction, and n_x and n_z summation is made from -5 to 5 . Afterwards, a slight modification is made to the normalization factor for the inverse DCT of this expression to satisfy Eq. (8.2).

As suggested in section 8.3, the system boundary is extended beyond the neutral wall by $2a$ in both $+z$ and $-z$ directions, and the pseudo-spectral method with DCT is used for the partition function calculation through the convolution integral. With this method, it is possible to keep the time complexity of the one-step evolution to be $O(M \log M)$. For the field calculation, it is also required to perform a convolution integral given by Eq. (6.17), and the aforementioned boundary extension technique is also applicable to this calculation.

Figure 9-3(b) exhibits the excess free energy comparison between the surface-perpendicular and surface-parallel lamellar morphologies at $N = 20$ by using the $N - 1$ bond (solid lines) and N bond (dashed lines) FJC models. The excess free energy per chain is normalized by the dimensionless film thickness $L_z/aN^{1/2}$ so that the effective interfacial energy can be compared [64, 149]. With the adoption of the finite-range interaction, the vertical lamellar morphology can reduce the energy penalty of the A-B interaction near the polymer-air or polymer-substrate interface, and thus a clear energy gap exists even when L_z is an integer multiple of $L_0/2$ which is the commensurate film thickness. The gap turns out to be independent of the layer number n_l , which is consistent with the idea that this gap corresponds to the surface tension difference of the two morphologies.

The free energy behaviors of the two morphologies at $N = 100$ and $N = 500$ are also plotted in figures 9-3 (c) and 9-3 (d), respectively. One can observe a clear reduction of the free energy gap as N increases. It is because the difference between the discrete chain SCFT and standard SCFT reduces as N increases, and they become identical at $N \rightarrow \infty$. In this limit, the interaction model employed with range a reduces to the contact interaction model, and thus it recovers the result of the standard SCFT in which the free energy gap is known to vanish.

Some standard SCFT studies [144–146] reported finite size of free energy gaps and predicted that the surface-perpendicular morphologies become favorable due to the surface-induced compatibilization. Those SCFT researches use incompressible block copolymer melts, and the hard neutral walls are represented by gradually decreasing density profiles near the surfaces. Due to the gradual reduction of the density in the surface region, the interaction between A and B segments is reduced near the neutral wall. This energetic effect promotes the perpendicular morphology in which more A-B contacts exist near the surface compared to the parallel one, and this phenomenon is referred to as the negative line tension [144–146]. For the theory in this study, a similar effect is found due to the finite-range interaction despite that a step function shaped density profile is adopted.

9.2 Diblock Copolymers in Thin Film

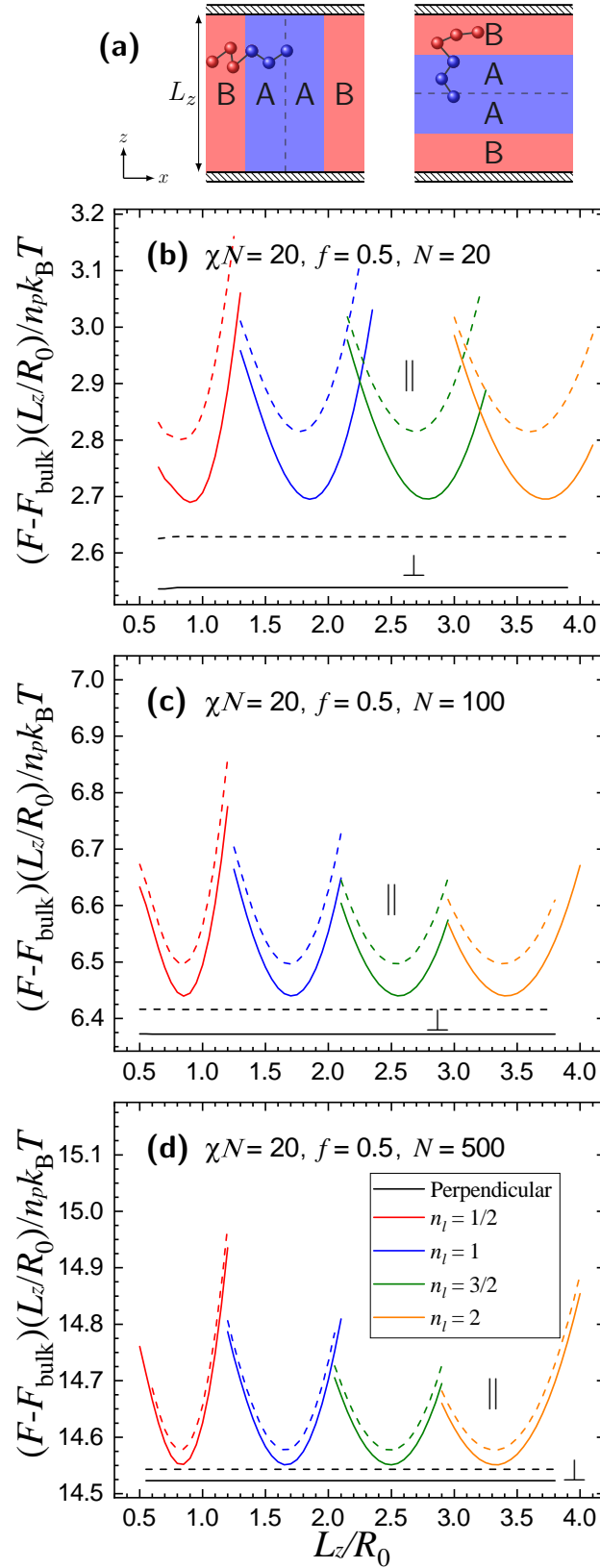


Figure 9-3: (a) Schematic diagram of freely jointed AB block copolymers confined by the two neutral walls. (b) The free energy comparison between the surface-perpendicular (black lines, \perp) and surface-parallel (colored lines, \parallel) morphologies with n_l periods at $\chi N = 20$, $f = 0.5$, and $N = 20$. Dashed lines are for the N bond model, and real lines are for the $N - 1$ bond model. (c) and (d) are the free energy comparison plot at $N = 100$ and $N = 500$, respectively.

9.2 Diblock Copolymers in Thin Film

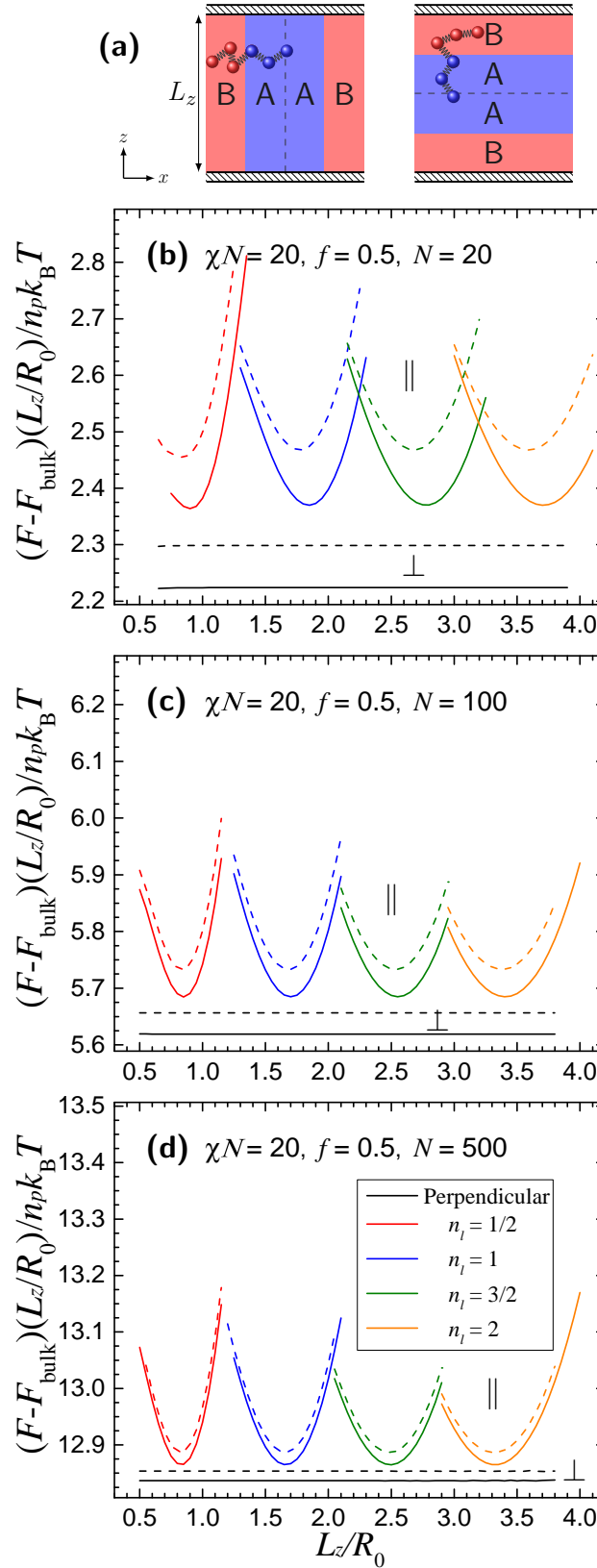


Figure 9-4: (a) Schematic diagram of AB block copolymers with BS model. (b) The free energy comparison between the surface-perpendicular (black lines, \perp) and surface-parallel (colored lines, \parallel) morphologies with n_l periods at $\chi N = 20$, $f = 0.5$, and $N = 20$. Dashed lines are for the N bond model, and real lines are for the $N - 1$ bond model. (c) and (d) are the free energy comparison plot at $N = 100$ and $N = 500$, respectively.

For the value of the free energy, it must be carefully interpreted. One may think that as N increases, the chain has more segments, and thus it has more entropy due to the increase of flexibility. As observed in figures 9-3 (b)–(d), however, the absolute value of the excess free energy increases as N increases. It is because the freely gyrating chain provides the reference point of the entropy or free energy, and the loss of entropy is only measured with respect to this state, which actually diverges as $N \rightarrow \infty$. It does not create any problem because the free energy difference is all that matters, and figure 9-3 clearly shows that the free energy gap actually converges to 0 in this limit.

The aforementioned surface energy behavior is not a special feature of the FJC model. As shown in figures 9-4 (b)–(d), the BS model exhibits similar behavior, and a minor difference is observed at small N . Regarding the difference between the $N - 1$ bond and N bond models, the absolute value of the excess free energy is higher for the N bond model because it has one more bond and each bond contributes a certain amount of entropy loss by the neutral wall. Even though the difference is not so noticeable, the size of the gap was also slightly bigger for the N bond model, and this is more difficult to explain. I speculate that the $N - 1$ bond model's tendency of the chain end density increase near the wall reported by Matsen and coworkers [112,113] may provide a slight advantage to the surface parallel phase which naturally accumulates more chain ends at both walls.

Before ending this section, I will briefly discuss the advantage of the pseudo-spectral method over the full spectral method. Full spectral method was originally developed to obtain the phase diagram of the inhomogeneous polymer system, and it is extremely powerful when the symmetry of the morphology and the corresponding basis functions are well known. However, when the domain or boundary shape is complicated, the basis functions are practically impossible to predict, and the adoption of the pseudo-spectral method becomes necessary. Also, for the extremely highly stretched systems I tested in the previous section, it is known that the full spectral method eventually becomes inefficient because of the fast increase of required basis functions.

10

Conclusion

The discrete chain self-consistent field theory can be a useful tool for the study of the short polymer systems. In this part of thesis, its full algebraic formulation is presented and the issues of numerical implementation are discussed. Since the high computational demands of the real space method limit its applicability to the higher dimensional system, I propose the efficient numerical techniques utilizing the pseudo-spectral method for solving the recursive equations of the partial partition function.

For the purpose of efficient adaptation of the pseudo-spectral method, I presented a new algebraic description of the discrete chain SCFT adopting half-segment propagation in the calculation of the partial partition function. The pseudo-spectral strategy is examined for the three-dimensional FJC model whose discrete version has a limitation in representing the Dirac delta shaped bond function. To overcome this troublesome issue, sampling theory of the DTFT is employed which provides an efficient method to calculate DCT of cell-averaged FJC bond function. The successful implementation of pseudo-spectral method for both FJC and BS models was verified, and it was confirmed that the discrete chain SCFT can be an efficient numerical tool performing calculations as fast as the standard SCFT.

As a model system, the discrete chain SCFT is applied to the analysis of symmetric block copolymers, and the chain behavior in the lamellar morphology was investigated. By calculating lamellar periods and interfacial widths for various chain models, it is found that FJC model behaves more like the standard SCFT due to residual mixing effect resulting from step-shaped bond function.

In the standard SCFT calculation, Dirichlet and Neumann boundary conditions are the natural choices to model the physical boundary, but the discrete chain SCFT opens up a new possibility of adopting the neutral boundary condition. Unlike the other boundary conditions, neutral wall boundary requires a subtle consideration since DST is not applicable in its pseudo-spectral implementation. For this special case, I proposed a very simple technique which extends the system boundary beyond the neutral wall to allow the convolution integral calculation using DCT. By combining the neutral boundary with the finite-range interaction model, I studied the

block copolymer thin film system confined by hard walls and successfully demonstrated how the surface-perpendicular block copolymer lamellar phase becomes preferable to the surface-parallel one when both the top and bottom surfaces are neutralized.

One special advantage of the discrete chain SCFT is that infinitely many possible polymer chain models can be adopted by replacing the bond function $g(\mathbf{r})$. For example, lattice SCFT [103,104] has been one branch of the SCFT, and the standard lattice SCFT can be reproduced in the Cartesian coordinates by adopting $N - 1$ bond model and using the following bond function,

$$g(0, 0, \pm a) = g(0, \pm a, 0) = g(\pm a, 0, 0) = \frac{1}{6}, \quad (10.1a)$$

$$g(x, y, z) = 0 \quad \text{otherwise}, \quad (10.1b)$$

in a spatial grid discretized by a .

This versatility of discrete chain SCFT mentioned above comes from the fact that any practical random step without directional memory can be implemented just by changing $g(\mathbf{r})$. The condition that the distribution of a polymer segment must be independent of the previous segment distribution may become invalid for more realistic bond models such as the semi-flexible worm like chain model. For such cases, the discrete chain SCFT formalism may be generalized by introducing a two-point distribution function, $g(\mathbf{R}_1, \mathbf{R}_2)$, where \mathbf{R}_1 is the vector for the current step and \mathbf{R}_2 is the vector for the previous step. The partition function now becomes a two-point function which can be calculated by

$$\begin{aligned} & q(\mathbf{r}, \mathbf{r} - \mathbf{R}_1, s + \Delta s) \\ &= \int d\mathbf{R}_2 g(\mathbf{R}_1, \mathbf{R}_2) q(\mathbf{r} - \mathbf{R}_1, \mathbf{r} - \mathbf{R}_1 - \mathbf{R}_2, s), \end{aligned} \quad (10.2)$$

where $q(\mathbf{r}, \mathbf{x}, s)$ is the partition function of a segment with its sN 'th and $(s - \Delta s)N$ 'th segments are positioned at \mathbf{r} and \mathbf{x} , respectively, and I omitted the field term which can be added according to the physical situation. For model systems of surfactants or lipid molecules, semi-flexible discrete polymer chain model is more realistic than the standard Gaussian chain model without any stiffness. For example, hydrocarbon tails in phospholipids of biological membrane can be modeled by short discrete chains with bending energy. The use of semi-flexible worm like chain requires additional dimension for the SCFT calculation and the pseudo-spectral method can be a good choice for reducing the computational cost.

It is well known that mean-field theory becomes inaccurate for systems of polymers with low molecular weight, and thus the discrete chain SCFT has its limitation for the analysis of short polymer candidates for high χ material. However, it at least incorporates the effect of finite segment size and number in the mean field theory, which is difficult to distinguish from the pure fluctuation effect. This approach is also useful when comparing results of SCFT to other particle-based simulations which include the full fluctuation effect. A recently emerging polymer

simulation method is the single chain in mean field (SCMF) simulation [150–152] which attempts to incorporate the fluctuation effect in the field theoretical calculation by performing explicit MC simulation of polymer chains under the quasi-instantaneously updated self-consistent field. Because of this, the SCMF simulation is usually considered as an intermediate approach between the field-based simulation and particle-based simulation. The SCMF simulation inevitably employs polymer chains with a finite number of segments, and its density calculation method using discrete grids is reminiscent of the finite-range interaction of the discrete chain SCFT. These facts imply that the discrete chain SCFT is an intermediate theoretical tool residing in between the standard SCFT and SCMF simulation. i.e. in the limit of infinitely many chains, the fluctuation effect becomes negligible, and the SCMF simulation result should converge to that of the discrete chain SCFT with the same chain model. If $N \rightarrow \infty$ limit is additionally taken, the discrete chain SCFT finally converges to the standard SCFT. This relation implies that discrete chain SCFT can provide insight to distinguish the effect of finite segment from the effect of fluctuation.

In addition, there is the potential pedagogical advantage of the discrete chain SCFT. The formulation of the standard SCFT involves functional integrals over all the possible polymer paths. Proportionality constants are often floating in the functional integral, and many students and researchers who first learn this theoretical tool have trouble following all the algebraic steps. On the other hand, the discrete chain SCFT formalism is very clear and neat, and it does not involve any functional integrals over the chain paths. Because of this, it is conceptually easier and all the partition function calculations can be done rigorously without any hidden proportionality constants. In summary, the discrete chain SCFT can provide a good starting point for those who are eager to learn the statistical mechanical method in polymer physics, and the use of the pseudo-spectral method makes it a promising tool for the research of various polymeric systems.

Appendix A

Mean Field Density and Free Energy of the Two Particle System

In this appendix, I discuss the detailed derivation of the mean field segment density and the free energy expression for the homopolymers and brush chains grafted to two particles. I begin with the expression of the formal partition function of the system, shown as Eq. (2.2). A functional integral $\int \mathcal{D}\Phi_f \delta[\Phi_f - \hat{\phi}_f]$ is inserted to replace the chain conformation dependent density function $\hat{\phi}_f$ with the ordinary function Φ_f [64],

$$Z \propto \frac{1}{n_g!n_f!} \int \mathcal{D}\Phi_f \prod_{i=1}^{n_g} \mathcal{D}\mathbf{r}_{g,i} P[\mathbf{r}_{g,i}] \prod_{j=1}^{n_f} \mathcal{D}\mathbf{r}_{f,j} P[\mathbf{r}_{f,j}] \times (\delta(r_{g,i}(1) - R) + \delta(\bar{r}_{g,i}(1) - R)) \delta[1 - \hat{\phi}_g - \Phi_f] \delta[\Phi_f - \hat{\phi}_f] \quad (\text{A.1})$$

The two delta functionals are now replaced with integral representations by using

$$\delta[f] \propto \int \mathcal{D}W \exp\left(\frac{\rho_0}{N} \int d\mathbf{r} W(\mathbf{r})f(\mathbf{r})\right) \quad (\text{A.2})$$

where W_g and W_f are used for the first and second delta functions, respectively, and the W integrations are along the imaginary axis. The density functions $\hat{\phi}_g$ and $\hat{\phi}_f$ are substituted with their definitions in Eqs. (2.3) and (2.4), respectively, and the result of the algebraic transform is

$$Z \propto \frac{1}{n_g!n_f!} \int \mathcal{D}\Phi_f \prod_{i=1}^{n_g} \mathcal{D}\mathbf{r}_{g,i} P[\mathbf{r}_{g,i}] \prod_{j=1}^{n_f} \mathcal{D}\mathbf{r}_{f,j} P[\mathbf{r}_{f,j}] (\delta(r_{g,i}(1) - R) + \delta(\bar{r}_{g,i}(1) - R)) \times \int \mathcal{D}W_g \exp\left[\frac{\rho_0}{N} \int d\mathbf{r} W_g(1 - \Phi_f)\right] \exp\left[-\sum_{i=1}^{n_g} \int_0^1 ds W_g(\mathbf{r}_{g,i}(s))\right] \times \int \mathcal{D}W_f \exp\left[\frac{\rho_0}{N} \int d\mathbf{r} W_f \Phi_f\right] \exp\left[-\sum_{j=1}^{n_f} \int_0^\alpha ds W_f(\mathbf{r}_{f,j}(s))\right] \quad (\text{A.3})$$

The above equation can be rewritten as

$$Z \propto \frac{1}{n_g!n_f!} \int \mathcal{D}W_g \mathcal{D}W_f \mathcal{D}\Phi_f \left(\frac{\rho_0}{N} Q_g[W_g] \right)^{n_g} \left(\frac{\rho_0}{\alpha N} Q_f[W_f] \right)^{n_f} \times \exp \left(\frac{\rho_0}{N} \int d\mathbf{r} W_g (1 - \Phi_f) + \frac{\rho_0}{N} \int d\mathbf{r} W_f \Phi_f \right) \quad (\text{A.4})$$

where $Q_\kappa[W_\kappa]$ are the single chain partition functions for both grafted chain ($\kappa = g$) and free chain ($\kappa = f$) subjected to the external fields, $W_\kappa(\mathbf{r})$, as follows:

$$Q_g[W_g] \propto \int \mathcal{D}\mathbf{r} (\delta(r(1) - R) + \delta(\bar{r}(1) - R)) \times \exp \left[-\frac{3}{2a^2N} \int_0^1 ds |\mathbf{r}'(s)|^2 - \int_0^1 ds W_g(\mathbf{r}(s)) \right] \quad (\text{A.5})$$

$$Q_f[W_f] \propto \int \mathcal{D}\mathbf{r} \exp \left[-\frac{3}{2a^2N} \int_0^\alpha ds |\mathbf{r}'(s)|^2 - \int_0^\alpha ds W_f(\mathbf{r}(s)) \right] \quad (\text{A.6})$$

It is customary to extract factors $(\rho_0/N)^{n_g}$ and $(\rho_0/\alpha N)^{n_f}$ from the unspecified proportionality constant in eq (A.4) for future simplification [64]. After applying Stirling approximation ($\ln(n_\kappa!) \approx n_\kappa \ln n_\kappa - n_\kappa$) on the factorials, the partition function of the system can be reexpressed as

$$Z \propto \int \mathcal{D}W_g \mathcal{D}W_f \mathcal{D}\Phi_f \exp \left(-\frac{F[W_g, W_f, \Phi_f]}{k_B T} \right) \quad (\text{A.7})$$

$$\frac{F}{k_B T} = n_g \left(\ln \left(\frac{V_g}{Q_g[W_g]} \right) - 1 \right) + n_f \left(\ln \left(\frac{V_f}{Q_f[W_f]} \right) - 1 \right) - \frac{\rho_0}{N} \int d\mathbf{r} [W_g(1 - \Phi_f)] - \frac{\rho_0}{N} \int d\mathbf{r} [W_f \Phi_f] \quad (\text{A.8})$$

where $V_g \equiv n_g N / \rho_0$ and $V_f \equiv \alpha n_f N / \rho_0$.

In the standard self-consistent field theory (SCFT) formulation, mean field solutions are obtained by applying the saddle point approximation which is asymptotically exact in the limit of very long chains. In this approach, the exponent in eq (A.7) is minimized by functional derivative with respect to the three field variables, W_g , W_f and Φ_f as follows:

$$\frac{\mathcal{D}F(W_g, W_f, \Phi_f)}{\mathcal{D}W_f} = 0 \quad (\text{A.9})$$

$$\frac{\mathcal{D}F(W_g, W_f, \Phi_f)}{\mathcal{D}W_g} = 0 \quad (\text{A.10})$$

$$\frac{\mathcal{D}F(W_g, W_f, \Phi_f)}{\mathcal{D}\Phi_f} = 0 \quad (\text{A.11})$$

From now on, I will use lowercase functions w_g , w_f and ϕ_f for the saddle point solution of the above equations. The first functional derivative, eq (A.9), reduces to

$$\phi_f(\mathbf{r}) = -\frac{V_f}{\alpha} \frac{\mathcal{D} \ln(Q_f[w_f])}{\mathcal{D}w_f(\mathbf{r})} = \langle \hat{\phi}_f(\mathbf{r}) \rangle \quad (\text{A.12})$$

which identifies the mean field function $\phi_f(\mathbf{r})$ as the ensemble average segment density of $\hat{\phi}_f(\mathbf{r})$ at the mean field $w_f(\mathbf{r})$. The second functional derivative, eq (A.10), leads to

$$1 - \phi_f(\mathbf{r}) = -V_g \frac{\mathcal{D} \ln(Q_g[w_g])}{\mathcal{D} w_g(\mathbf{r})} = \langle \hat{\phi}_g(\mathbf{r}) \rangle \quad (\text{A.13})$$

which implies the incompressibility condition

$$\phi_g(\mathbf{r}) + \phi_f(\mathbf{r}) = 1 \quad (\text{A.14})$$

where ϕ_g is the ensemble average segment density of $\hat{\phi}_g(\mathbf{r})$ at the mean field $w_g(\mathbf{r})$. The third functional derivative, eq (A.11), produces

$$w_g(\mathbf{r}) = w_f(\mathbf{r}) \quad (\text{A.15})$$

This relation is not as trivial as one might think at first glance. It is true only when the continuous parameter s of the free chain goes from 0 to α . There is another approach of using the parameter range $[0,1]$, which results in $w_f(\mathbf{r})$ larger than $w_g(\mathbf{r})$ by a factor α .

After all the segment densities and mean potential fields are obtained, the mean field free energy for the system is,

$$\frac{F}{k_B T} = n_g \left(\ln \left(\frac{V_g}{Q_g[w]} \right) - 1 \right) + n_f \left(\ln \left(\frac{V_f}{Q_f[w]} \right) - 1 \right) - \frac{\rho_0}{N} \int d\mathbf{r} w(\mathbf{r}) (\phi_g(\mathbf{r}) + \phi_f(\mathbf{r})) \quad (\text{A.16})$$

where the subscripts for the fields are omitted. With the current expression, when I take larger system size by adding more free homopolymer chains, the free energy varies due to the increase of the free chain numbers as implied by the term -1 in the second parenthesis. When considering effective interaction between two particles, the system size varies with the interparticle distance D , and the system size dependent free energy expression is inappropriate. For this reason, I adopt the following free energy expression which is independent of the system size,

$$\frac{F}{k_B T} = n_g \ln \left(\frac{V_g}{Q_g[w]} \right) + n_f \ln \left(\frac{V_f}{Q_f[w]} \right) - \frac{\rho_0}{N} \int d\mathbf{r} w(\mathbf{r}) (\phi_g(\mathbf{r}) + \phi_f(\mathbf{r})) \quad (\text{A.17})$$

With this form, the free energy value converges to a finite value as the system size diverges by adding infinitely many free chains, thus this excess free energy expression provides the proper interparticle interaction potential in the homopolymer background.

Appendix B

SCFT of End-fixed Brushes

The SCFT formulation in appendix A assumes that the grafted chain ends can float on the particle surface. Even when the chain ends are attached to the particle surface with strong chemical bonds, most procedures for deriving SCFT equations remain the same and only a few modifications to the SCFT equations are required [22, 60].

The segment density of chains grafted to particle one, $\phi_{g1}(\mathbf{r})$, is still obtained by calculating Eq. (2.20), but there exists one exception that the initial condition of q_{g1}^\dagger is modified to

$$q_{g1}^\dagger(\mathbf{r}, 1) = \frac{V_{g1}\delta(r - R)}{4\pi R^2 q_{g1}(\mathbf{r}, 1)} \quad (\text{B.1})$$

With this initial condition, brush chains are now uniformly grafted over the particle surface with surface density $\sigma_0 \equiv n_g/8\pi R^2$. After obtaining all the segment densities and mean potential fields, the free energy for the end-fixed brush case becomes

$$\frac{F}{k_B T} = n_f \ln \left(\frac{V_f}{Q_f[w]} \right) - 2\sigma_0 \int d\mathbf{r} \delta(r - R) \ln(q_g(\mathbf{r}, 1)) - \frac{\rho_0}{N} \int d\mathbf{r} w(\mathbf{r}) (\phi_g(\mathbf{r}) + \phi_f(\mathbf{r})) \quad (\text{B.2})$$

Appendix C

Contour Plots for Chain End Types

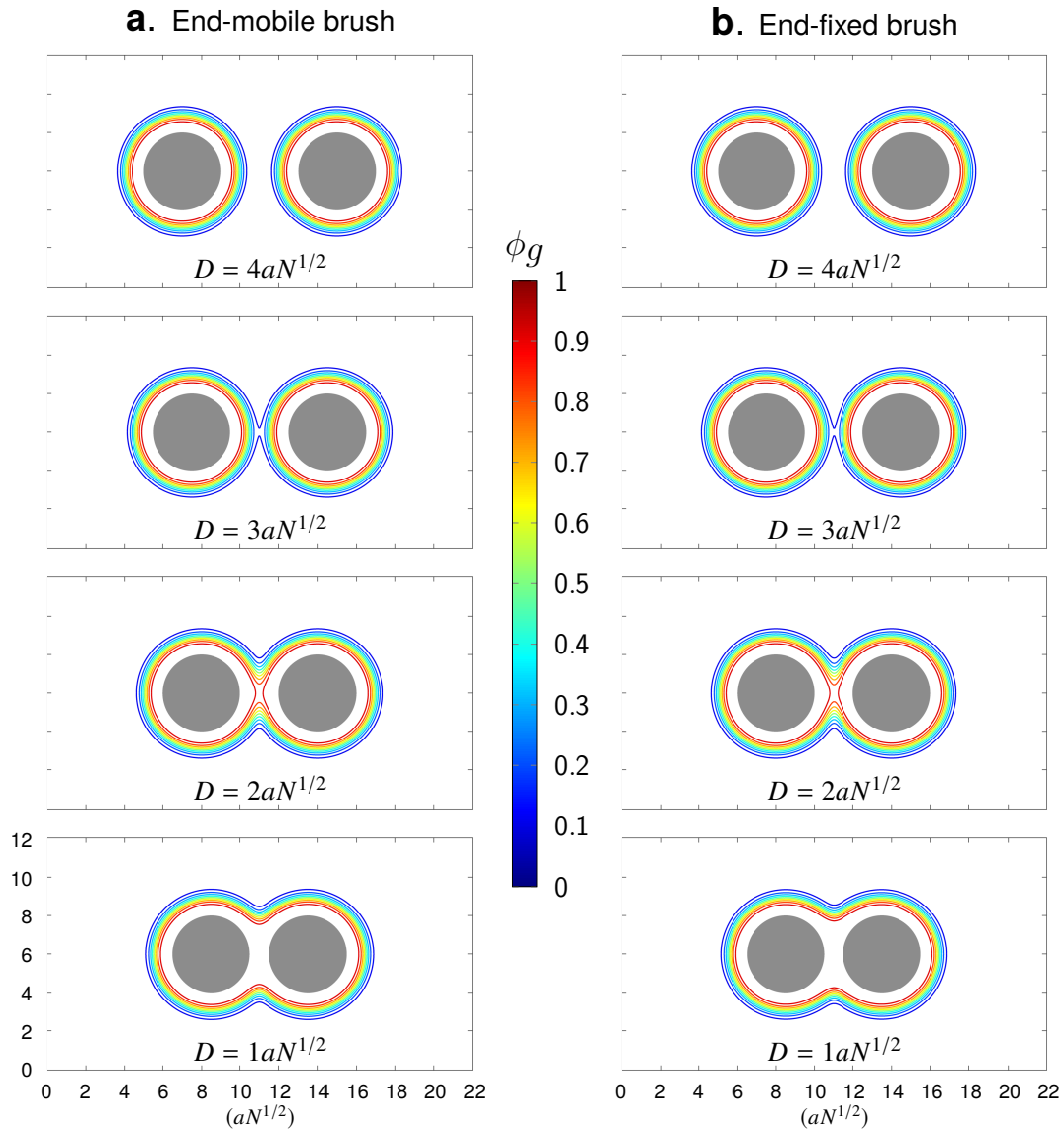


Figure A.1: Contour plots of grafted polymer segment density, ϕ_g , of (a) end-mobile and (b) end-fixed brushes at various interparticle distances D with the system geometry $R = 2aN^{1/2}$, $H_{\text{brush}} = aN^{1/2}$ and $\alpha = 10$ which corresponds to the green line in figure 3-11 (b).

Appendix D

Recursive Integral Equation of Partition Function

The two-point partial partition function $q(\mathbf{r}, \mathbf{r}_0, s)$ can be expressed in terms of the partition functions of two shorter fragments as follows,

$$q(\mathbf{r}, \mathbf{r}_0, s + t) = \frac{1}{(a^2 N)^{3/2}} \int d\mathbf{R} q(\mathbf{r}, \mathbf{r} - \mathbf{R}, t) q(\mathbf{r} - \mathbf{R}, \mathbf{r}_0, s). \quad (\text{D.1})$$

This recurrence relation is equivalent to that of the standard self-consistent field theory (SCFT). For the discrete chain SCFT, it can be proven directly from the partition function definition, Eq. (6.5), and the property of the Dirac delta function. From Eqs. (6.4) and (6.5), the distribution function of a small segment in the bead-spring (BS) model is obtained as

$$q(\mathbf{r}, \mathbf{r}_0, \Delta s) = \left(\frac{3N}{2\pi}\right)^{3/2} \exp\left(-\frac{3(\mathbf{r} - \mathbf{r}_0)^2}{2a^2} - \frac{w(\mathbf{r}_0) + w(\mathbf{r})}{2N}\right), \quad (\text{D.2})$$

where $\Delta s = 1/N$. By setting $t = \Delta s$ in Eq. (D.1), we can directly use Eq. (D.2) for the evaluation of the recursive integral. The resulting evolution equation of the partition function is

$$g(\mathbf{r}) \equiv \left(\frac{3}{2\pi a^2}\right)^{3/2} \exp\left(-\frac{3\mathbf{r}^2}{2a^2}\right), \quad (\text{D.3a})$$

$$q(\mathbf{r}, \mathbf{r}_0, s + \Delta s) = \exp\left(-\frac{w(\mathbf{r})}{2N}\right) \int d\mathbf{R} g(\mathbf{R}) \exp\left(-\frac{w(\mathbf{r} - \mathbf{R})}{2N}\right) q(\mathbf{r} - \mathbf{R}, \mathbf{r}_0, s). \quad (\text{D.3b})$$

Appendix E

Total Partition Function and Segment Density in Discrete Chain SCFT

The densities of A and B type segments are defined by the formal ensemble averages of Eq. (6.3). For example, the A segment density is

$$\begin{aligned} \phi_{\alpha,A}(\mathbf{r}) &= \frac{1}{\rho_0 Q[w]} \left(\frac{2\pi a^2}{3} \right)^{3/2} \prod_{u=\{0,\dots,1\}} \left(\frac{3}{2\pi a^2} \right)^{3/2} \\ &\quad \times \int d\mathbf{r}_\alpha(u) \sum'_{s \in \{0,\dots,f\}} \delta(\mathbf{r} - \mathbf{r}_\alpha(s)) \exp\left(-\frac{E(\mathbf{r}_\alpha; 0, 1)}{k_B T}\right), \end{aligned} \quad (\text{E.1})$$

where the total partition function of the diblock copolymer is defined as

$$Q[w] \equiv \left(\frac{2\pi a^2}{3} \right)^{3/2} \prod_{u=\{0,\dots,1\}} \left(\frac{3}{2\pi a^2} \right)^{3/2} \int d\mathbf{r}_\alpha(u) \exp\left(-\frac{E(\mathbf{r}_\alpha; 0, 1)}{k_B T}\right). \quad (\text{E.2})$$

Here follows a short proof that the total partition function can be written in terms of the one-point partial partition functions as follows,

$$Q[w] = \int d\mathbf{r} q(\mathbf{r}, s) q^\dagger(\mathbf{r}, s), \quad (\text{E.3})$$

where one-point partial partition functions are expressed as

$$q(\mathbf{r}, s) = \left(\frac{2\pi}{3N} \right)^{3/2} \prod_{u \in \{0,\dots,s\}} \left(\frac{3}{2\pi a^2} \right)^{3/2} \int d\mathbf{r}_\alpha(u) \exp\left(-\frac{E(\mathbf{r}_\alpha; 0, s)}{k_B T}\right) (a^2 N)^{3/2} \delta(\mathbf{r}_\alpha(s) - \mathbf{r}), \quad (\text{E.4a})$$

$$q^\dagger(\mathbf{r}, s) = \left(\frac{2\pi}{3N} \right)^{3/2} \prod_{u \in \{s,\dots,1\}} \left(\frac{3}{2\pi a^2} \right)^{3/2} \int d\mathbf{r}_\alpha(u) \exp\left(-\frac{E(\mathbf{r}_\alpha; s, 1)}{k_B T}\right) (a^2 N)^{3/2} \delta(\mathbf{r}_\alpha(s) - \mathbf{r}), \quad (\text{E.4b})$$

from Eqs. (6.5), (6.6), and (6.8).

By substituting Eq. (E.4) into Eq. (E.3), the total partition function becomes multiple integrals of the position variables $\mathbf{r}_\alpha(u)$ ($u \in \{0, \Delta s, \dots, 1\}$) where the variable $\mathbf{r}_\alpha(s)$ appears twice, because the point s exists in both one-point partial partition functions. By integrating one of the overlapping variable $\mathbf{r}_\alpha(s)$, one of the delta functions is removed, and integration of the position variables \mathbf{r} in Eq. (E.3) removes the remaining delta function. As a result, the direct evaluation of the right hand side of Eq. (E.3) becomes equivalent to the definition given in Eq. (E.2).

The ensemble average densities of A and B type segments can also be evaluated by using the one-point partial partition functions as follows,

$$\phi_A(\mathbf{r}) = \frac{V}{NQ} \sum'_{s \in \{0, \dots, f\}} q(\mathbf{r}, s) q^\dagger(\mathbf{r}, s) , \quad (\text{E.5a})$$

$$\phi_B(\mathbf{r}) = \frac{V}{NQ} \sum'_{s \in \{f, \dots, 1\}} q(\mathbf{r}, s) q^\dagger(\mathbf{r}, s) . \quad (\text{E.5b})$$

These relations can be proven in a way similar to the total partition function case by substituting Eq. (E.4) into the right hand side of Eq. (E.5). After simple integration, the resulting expression becomes exactly the same as the ensemble average definition of the segment density, Eq. (E.1).

Appendix F

Calculation of FJC \tilde{g}_i using Sampling Theory of DTFT

In this appendix, I explain how the cell-averaged g_i of the FJC model defined by Eq. (8.7) can be calculated using a few equations in the DTFT and the sampling theory. For simplicity, I demonstrate the one-dimensional version of the calculation in which the aim is to calculate

$$g_k \equiv \frac{1}{\Delta z} \int_{-\Delta z/2}^{\Delta z/2} g(k\Delta z - z') dz' . \quad (\text{F.1})$$

I start by defining a continuous average function,

$$\bar{g}(z) \equiv \frac{1}{\Delta z} \int_{-\Delta z/2}^{\Delta z/2} g(z - z') dz' , \quad (\text{F.2})$$

which makes $\bar{g}(k\Delta z)$ as the target array g_k . Because $\bar{g}(z)$ is a convolution of $g(z)$ and a rectangular function which is defined as $\Pi(x) \equiv 1$ only when $|x| \leq 1/2$,

$$\bar{g}(z) = \frac{1}{\Delta z} \int_{-\infty}^{\infty} g(z - z') \Pi\left(\frac{z'}{\Delta z}\right) dz' . \quad (\text{F.3})$$

Using the convolution theorem, the Fourier transform of $\bar{g}(z)$ is calculated as

$$\tilde{\bar{g}}(\xi) = \tilde{g}(\xi) \text{sinc}(\xi\Delta z) = \text{sinc}(2\xi a) \text{sinc}(\xi\Delta z) , \quad (\text{F.4})$$

where the last equation uses the Fourier transform of the one-dimensional FJC bond function.

The DTFT of a generic function $f(z)$ sampled at interval Δz is

$$F(\xi) \equiv \Delta z \sum_{n=-\infty}^{\infty} f(n\Delta z) e^{-i2\pi\xi\Delta zn} , \quad (\text{F.5})$$

and it is a periodic summation of $\tilde{f}(\xi)$ which is a Fourier transform of $f(z)$ [153],

$$F(\xi) = \sum_{n=-\infty}^{\infty} \tilde{f}\left(\xi - \frac{n}{\Delta z}\right). \quad (\text{F.6})$$

When an even function $f(z)$ is defined at $-L_z < z < L_z$ and zero outside this region, I can relate the DTFT with the DCT by setting $\xi = k/2L_z$ where $L_z = K\Delta z$,

$$\begin{aligned} \frac{1}{2\Delta z} F\left(\frac{k}{2K\Delta z}\right) &= \frac{1}{2} \sum_{n=-\infty}^{\infty} f(n\Delta z) e^{-i\pi nk/K} \\ &= \sum_{n=0}^{K'} f(n\Delta z) \cos\left(\frac{\pi nk}{K}\right) = \tilde{f}_k. \end{aligned} \quad (\text{F.7})$$

Applying this relation to $\bar{g}(z)$, and using Eqs. (F.4) and (F.6),

$$\begin{aligned} \tilde{g}_k &= \frac{1}{2\Delta z} \bar{G}\left(\frac{k}{2L_z}\right) = \frac{1}{2\Delta z} \sum_{n=-\infty}^{\infty} \tilde{g}\left(\frac{k}{2L_z} - \frac{n}{\Delta z}\right) \\ &= \frac{1}{2\Delta z} \sum_{n=-\infty}^{\infty} \text{sinc}\left(a \frac{k - 2n_z K}{L_z}\right) \text{sinc}\left(\frac{k - 2n_z K}{2K}\right). \end{aligned} \quad (\text{F.8})$$

It is straightforward to extend this result to the three-dimensional system to obtain Eq. (8.8).

Appendix G

Interfacial Energy Analysis

$$\gamma_{\text{total}} \equiv \frac{(F - F^{\text{disorder}})/k_{\text{B}}T}{\text{Area}/a^2} = \left(\frac{F - F^{\text{disorder}}}{nk_{\text{B}}T} \right) \left(\frac{L_z}{aN^{1/2}} \right) \rho_0 a^3 N^{-1/2} \quad (\text{G.1})$$

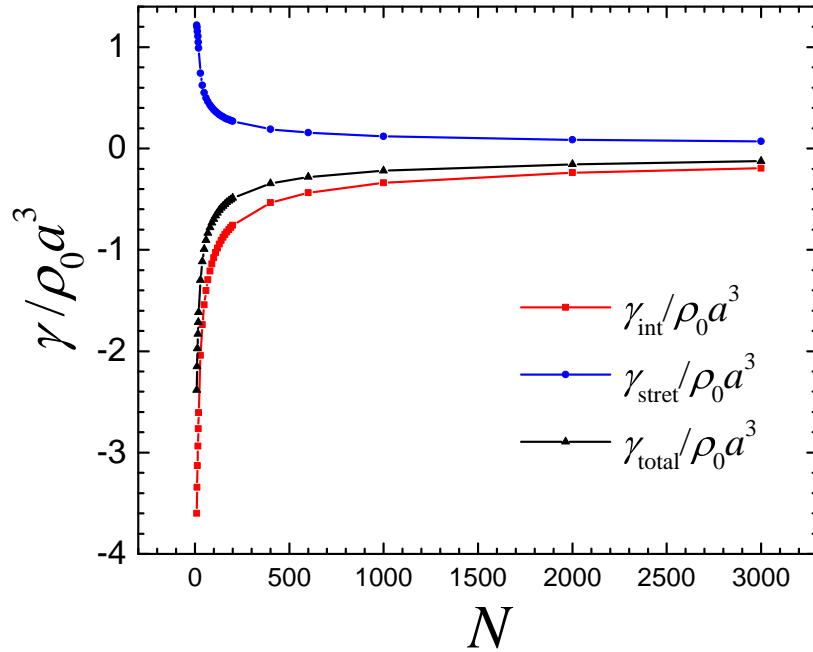


Figure A.2: Interfacial energy plot as a function of segment number N with $N - 1$ bond freely-jointed chain (FJC) model at $\chi N = 50$ (blue solid line in figure 9-1). For a fair comparison between systems with different N , dimensionless interfacial energies per unit area a^2 are plotted. The black line shows the total interfacial tension γ_{total} . The blue line represents γ_{stret} coming from the stretching free energy, and the red line represents γ_{int} coming from the interaction free energy.

References

- [1] S. J. Park, S. Kim, D. Yong, Y. Choe, J. Bang, and J. U. Kim, Interactions between brush-grafted nanoparticles within chemically identical homopolymers: the effect of brush polydispersity, *Soft Matter* 2018, **14**, 1026-1042.
- [2] S. J. Park, D. Yong, Y. Kim, and J. U. Kim, Numerical implementation of pseudo-spectral method in self-consistent mean field theory for discrete polymer chains, *J. Chem. Phys.* 2019, **150**, 234901.
- [3] G. Kickelbick, Concepts for the incorporation of inorganic building blocks into organic polymers on a nanoscale, *Prog. Polym. Sci.* 2003, **28**, 83-114. [2](#)
- [4] M. R. Bockstaller and E. L. Thomas, Proximity Effects in Self-Organized Binary Particle-Block Copolymer Blends, *Phys. Rev. Lett.* 2004, **93**, 166106. [2](#)
- [5] J. Bae, E. Glogowski, S. Gupta, W. Chen, T. Emrick, and T. P. Russell, Effect of Nanoparticles on the Electrohydrodynamic Instabilities of Polymer/Nanoparticle Thin Films, *Macromolecules* 2008, **41**, 2722-2726. [2](#)
- [6] D. R. Paul and L. M. Robeson, Polymer nanotechnology: Nanocomposites, *Polymer* 2008, **49**, 3187-3204. [2](#)
- [7] B. A. Rozenberg and R. Tenne, Polymer-assisted fabrication of nanoparticles and nanocomposites, *Prog. Polym. Sci.* 2008, **33**, 40-112. [2](#)
- [8] B. Natarajan, T. Neely, A. Rungta, B. C. Benicewicz, and L. S. Schadler, Thermomechanical Properties of Bimodal Brush Modified Nanoparticle Composites, *Macromolecules* 2013, **46**, 4909-4918. [2](#), [3](#)
- [9] S. Lee, B. Lee, B. J. Kim, J. Park, M. Yoo, W. K. Bae, K. Char, C. J. Hawker, J. Bang, and J. Cho, Free-Standing Nanocomposite Multilayers with Various Length Scales, Adjustable Internal Structures, and Functionalities, *J. Am. Chem. Soc.* 2009, **131**, 2579-2587. [2](#)
- [10] Y. Kim, C. Lee, I. Shim, D. Wang, and J. Cho, Nucleophilic Substitution Reaction Based Layer-by-Layer Growth of Superparamagnetic Nanocomposite Films with High Nonvolatile Memory Performance, *Adv. Mater.* 2010, **22**, 5140-5144. [2](#)

- [11] J. Gu, Y. Yan, Y. S. Zhao, and J. Yao, Controlled Synthesis of Bulk Polymer Nanocomposites with Tunable Second Order Nonlinear Optical Properties, *Adv. Mater.* 2012, **24**, 2249-2253. [2](#)
- [12] A. C. Balazs, T. Emrick, and T. P. Russell, Nanoparticle Polymer Composites: Where Two Small Worlds Meet, *Science* 2006, **314**, 1107-1110. [2](#)
- [13] V. Ganesan, and A. Jayaraman, Theory and simulation studies of effective interactions, phase behavior and morphology in polymer nanocomposites, *Soft Matter* 2014, **10**, 13-38. [2](#)
- [14] A. Hashemi, N. Jouault, G. A. Williams, D. Zhao, K. J. Cheng, J. W. Kysar, Z. Guan, and S. K. Kumar, Enhanced Glassy State Mechanical Properties of Polymer Nanocomposites via Supramolecular Interactions, *Nano Lett.* 2015, **15**, 5465-5471. [2](#)
- [15] C. Chevigny, N. Jouault, F. Dalmas, F. Boué, and J. Jestin, Tuning the Mechanical Properties in Model Nanocomposites: Influence of the Polymer-Filler Interfacial Interactions, *J. Polym. Sci. B Polym. Phys.* 2011, **49**, 781-791. [2](#)
- [16] H. S. Wang, A. Khan, Y. Choe, J. Huh, and J. Bang, Architectural Effects of Organic Nanoparticles on Block Copolymer Orientation, *Macromolecules* 2017, **50**, 5025-5032. [2](#)
- [17] P. Akcora, H. Liu, S. K. Kumar, J. Moll, Y. Li, B. C. Benicewicz, L. S. Schadler, D. Acehan, A. Z. Panagiotopoulos, V. Pryamitsyn, V. Ganesan, J. Ilavsky, P. Thiyagarajan, R. H. Colby, and J. F. Douglas, Anisotropic self-assembly of spherical polymer-grafted nanoparticles, *Nat. Mater.* 2009, **8**, 354-359. [2](#), [29](#)
- [18] X. Dou, X. Liu, Y. Zhang, H. Feng, J.-F. Chen, and S. Du, Improved dielectric strength of barium titanate-polyvinylidene fluoride nanocomposite, *Appl. Phys. Lett.* 2009, **95**, 132904. [2](#)
- [19] P. Akcora, S. K. Kumar, J. Moll, S. Lewis, L. S. Schadler, Y. Li, B. C. Benicewicz, A. Sandy, S. Narayanan, J. Ilavsky, P. Thiyagarajan, R. H. Colby, and J. F. Douglas, "Gel-like" Mechanical Reinforcement in Polymer Nanocomposite Melts, *Macromolecules* 2010, **43**, 1003-1010. [2](#), [29](#)
- [20] J. F. Moll, P. Akcora, A. Rungta, S. Gong, R. H. Colby, B. C. Benicewicz, and S. K. Kumar, Mechanical Reinforcement in Polymer Melts Filled with Polymer Grafted Nanoparticles, *Macromolecules* 2011, **44**, 7473-7477. [2](#), [29](#)
- [21] S. K. Kumar, V. Ganesan, and R. A. Riggleman, Perspective: Outstanding theoretical questions in polymer-nanoparticle hybrids, *J. Chem. Phys.* 2017, **147**, 020901. [2](#)

- [22] J. U. Kim and M. W. Matsen, Positioning Janus Nanoparticles in Block Copolymer Scaffolds, *Phys. Rev. Lett.* 2009, **102**, 078303. [2](#), [6](#), [9](#), [33](#), [34](#), [81](#)
- [23] S. Kim, M. Yoo, N. Kang, B. Moon, B. J. Kim, S.-H. Choi, J. U. Kim, and J. Bang, Nanoporous Bicontinuous Structures via Addition of Thermally-Stable Amphiphilic Nanoparticles within Block Copolymer Templates, *ACS Appl. Mater. Interfaces* 2013, **5**, 5659-5666. [2](#)
- [24] Y. Li, T. M. Krentz, L. Wang, B. C. Benicewicz, and L. S. Schadler, Ligand Engineering of Polymer Nanocomposites: From the Simple to the Complex, *ACS Appl. Mater. Interfaces* 2014, **6**, 6005-6021. [2](#), [29](#)
- [25] T. B. Martin, K. I. S. Mongcopa, R. Ashkar, P. Butler, R. Krishnamoorti, and A. Jayaraman, Wetting-Dewetting and Dispersion-Aggregation Transitions Are Distinct for Polymer Grafted Nanoparticles in Chemically Dissimilar Polymer Matrix, *J. Am. Chem. Soc.* 2015, **137**, 10624-10631. [2](#)
- [26] M. R. Bockstaller, R. A. Mickiewicz, and E. L. Thomas, Block Copolymer Nanocomposites: Perspectives for Tailored Functional Materials, *Adv. Mater.* 2005, **17**, 1331-1349. [2](#)
- [27] V. Pryamtsyn, V. Ganesan, A. Z. Panagiotopoulos, H. Liu, and S. K. Kumar, Modeling the anisotropic self-assembly of spherical polymer-grafted nanoparticles, *J. Chem. Phys.* 2009, **131**, 221102. [2](#)
- [28] Y. Jiao and P. Akcora, Assembly of Polymer-Grafted Magnetic Nanoparticles in Polymer Melts, *Macromolecules* 2012, **45**, 3463-3470. [2](#)
- [29] S. K. Kumar, N. Jouault, B. Benicewicz, and T. Neely, Nanocomposites with Polymer Grafted Nanoparticles, *Macromolecules* 2013, **46**, 3199-3214. [2](#), [4](#), [33](#)
- [30] N. Jouault, D. Zhao, and S. K. Kumar, Role of Casting Solvent on Nanoparticle Dispersion in Polymer Nanocomposites, *Macromolecules* 2014, **47**, 5246-5255. [2](#)
- [31] N. Jouault, M. K. Crawford, C. Chi, R. J. Smalley, B. Wood, J. Jestin, Y. B. Melnichenko, L. He, W. E. Guise, and S. K. Kumar, Polymer Chain Behavior in Polymer Nanocomposites with Attractive Interactions, *ACS Macro Lett.* 2016, **5**, 523-527. [2](#)
- [32] D. Zhao, M. D. Nicola, M. M. Khani, J. Jestin, B. C. Benicewicz, and S. K. Kumar, Self-Assembly of Monodisperse versus Bidisperse Polymer-Grafted Nanoparticles, *ACS Macro Lett.* 2016, **5**, 790-795. [2](#)
- [33] R. Shi, H.-J., Qian and Z.-Y. Lu, Computer simulation study on the self-assembly of unimodal and bimodal polymer-grafted nanoparticles in a polymer melt, *Phys.Chem.Chem.Phys.* 2017, **19**, 16524-16532. [2](#), [3](#)

- [34] N. Bachhar, Y. Jiao, M. Asai, P. Akcora, R. Bandyopadhyaya, and S. K. Kumar, Impact of the Distributions of Core Size and Grafting Density on the Self-Assembly of Polymer Grafted Nanoparticles, *Macromolecules* 2017, **50**, 7730-7738. [2](#)
- [35] J. H. Maas, G. J. Fleer, F. A. M. Leermakers, and M. A. Cohen Stuart, Enthalpic Stabilization of Brush-Coated Particles in a Polymer Melt, *Langmuir* 2002, **18**, 8871-8880. [3](#)
- [36] F. A. M. Leermakers, J. H. Maas, and M. A. Cohen Stuart, First-order wetting transition at finite contact angle, *Phys. Rev. E* 2002, **66**, 051801. [3](#)
- [37] D. L. Green and J. Mewis, Connecting the Wetting and Rheological Behaviors of Poly(dimethylsiloxane)-Grafted Silica Spheres in Poly(dimethylsiloxane) Melts, *Langmuir* 2006, **22**, 9546-9553. [3](#)
- [38] D. Sunday, J. Ilavsky, and D. L. Green, A Phase Diagram for Polymer-Grafted Nanoparticles in Homopolymer Matrices, *Macromolecules* 2012, **45**, 4007-4011. [3](#)
- [39] D. F. Sunday and D. L. Green, Thermal and Rheological Behavior of Polymer Grafted Nanoparticles, *Macromolecules* 2015, **48**, 8651-8659. [3](#)
- [40] Y. Li, P. Tao, A. Viswanath, B. C. Benicewicz, and L. S. Schadler, Bimodal Surface Ligand Engineering: The Key to Tunable Nanocomposites, *Langmuir* 2013, **29**, 1211-1220. [3](#)
- [41] A. Rungta, B. Natarajan, T. Neely, D. Dukes, L. S. Schadler, and B. C. Benicewicz, Grafting Bimodal Polymer Brushes on Nanoparticles Using Controlled Radical Polymerization, *Macromolecules* 2012, **45**, 9303-9311. [3](#)
- [42] P. G. Ferreira, A. Ajdari, and L. Leibler, Scaling Law for Entropic Effects at Interfaces between Grafted Layers and Polymer Melts, *Macromolecules* 1998, **31**, 3994-4003. [3](#), [4](#)
- [43] M. W. Matsen and J. M. Gardiner, Autophobic dewetting of homopolymer on a brush and entropic attraction between opposing brushes in a homopolymer matrix, *J. Chem. Phys.* 2001, **115**, 2794-2804. [3](#), [4](#), [20](#)
- [44] D. Meng, S. K. Kumar, J. M. D. Lane, and G. S. Grest, Effective interactions between grafted nanoparticles in a polymer matrix, *Soft Matter* 2012, **8**, 5002-5010. [3](#), [24](#)
- [45] H. Lee, W. Lee, Y. S. Han, E. Kim, and D. Y. Ryu, Autophobic dewetting of polystyrenes on the substrates grafted with chemically identical polymers, *Polym. J.* 2016, **48**, 503-507. [3](#)
- [46] J. Xu, F. Qui, H. Zhang, and Y. Yang, Morphology and Interactions of Polymer Brush-Coated Spheres in a Polymer Matrix, *J. Polym. Sci. B* 2006, **44**, 2811-2820. [4](#), [6](#), [33](#)

- [47] D. M. Trombly and V. Ganesan, Curvature effects upon interactions of polymer-grafted nanoparticles in chemically identical polymer matrices, *J. Chem. Phys.* 2010, **133**, 154904. [4](#), [6](#), [9](#), [24](#)
- [48] S. Srivastava, P. Agarwal, and L. A. Archer, Tethered Nanoparticle-Polymer Composites: Phase Stability and Curvature, *Langmuir* 2011, **28**, 6276-6281. [4](#)
- [49] J. Kim and P. F. Green, Phase Behavior of Thin Film Brush-Coated Nanoparticles/Homopolymer Mixtures, *Macromolecules* 2010, **43**, 1524-1529. [4](#)
- [50] C. Chevigny, F. Dalmas, E. D. Cola, D. Gigmes, D. Bertin, F. Boué, and J. Jestin, Polymer-Grafted-Nanoparticles Nanocomposites: Dispersion, Grafted Chain Conformation, and Rheological Behavior, *Macromolecules* 2011, **44**, 122-133. [4](#)
- [51] Amalie L. Frischknecht, Forces between nanorods with end-adsorbed chains in a homopolymer melt, *J. Chem. Phys.* 2008, **128**, 224902. [4](#)
- [52] M. J. A. Hore, A. L. Frischknecht, and R. J. Composto, Nanorod Assemblies in Polymer Films and Their Dispersion-Dependent Optical Properties, *ACS Macro Lett.* 2012, **1**, 115-121. [4](#)
- [53] A. L. Frischknecht, M. J. A. Hore, J. Ford, and R. J. Composto, Dispersion of Polymer-Grafted Nanorods in Homopolymer Films: Theory and Experiment, *Macromolecules* 2013, **46**, 2856-2869. [4](#)
- [54] S. E. Harton and S. K. Kumar, Mean-Field Theoretical Analysis of Brush-Coated Nanoparticle Dispersion in Polymer Matrices, *J. Polym. Sci., Part B: Polym. Phys.* 2008, **46**, 351-358. [4](#), [6](#)
- [55] T. V. M. Nodoro, E. Voyiatzis, A. Ghanbari, D. N. Theodorou, M. C. Böhm, and F. Müller-Plathe, Interface of Grafted and Ungrafted Silica Nanoparticles with a Polystyrene Matrix: Atomistic Molecular Dynamics Simulations, *Macromolecules* 2011, **44**, 2316-2327. [4](#)
- [56] S. R. Edgecombe, J. M. Gardiner, and M. W. Matsen, Suppressing Autophobic Dewetting by Using a Bimodal Brush, *Macromolecules* 2002, **35**, 6475-6477. [5](#), [29](#), [36](#)
- [57] T. B. Martin, P. M. Dodd, and A. Jayaraman, Polydispersity for Tuning the Potential of Mean Force between Polymer Grafted Nanoparticles in a Polymer Matrix, *Phys. Rev. Lett.* 2013, **110**, 018301. [5](#)
- [58] T. B. Martin and A. Jayaraman, Polydisperse homopolymer grafts stabilize dispersions of nanoparticles in a chemically identical homopolymer matrix: an integrated theory and simulation study, *Soft Matter* 2013, **9**, 6876-6889. [5](#)

- [59] J. U. Kim and M. W. Matsen, Repulsion Exerted on a Spherical Particle by a Polymer Brush, *Macromolecules* 2008, **41**, 246-252. [6](#)
- [60] J. U. Kim and M. W. Matsen, Interaction between Polymer-Grafted Particles, *Macromolecules* 2008, **41**, 4435-4443. [6](#), [9](#), [13](#), [14](#), [16](#), [33](#), [34](#), [81](#)
- [61] V. V. Ginzburg, Polymer-Grafted Nanoparticles in Polymer Melts: Modeling Using the Combined SCFT-DFT Approach, *Macromolecules* 2013, **46**, 9798-9805. [6](#)
- [62] J. U. Kim and M. W. Matsen, Finite-stretching corrections to the Milner-Witten-Cates theory for polymer brushes, *Eur. Phys. J. E* 2007, **23**, 135-144. [6](#)
- [63] J.-R. Roan, Attraction between Nanoparticles Induced by End-Grafted Homopolymers in Good Solvent, *Phys. Rev. Lett.* 2001, **86**, 1027-1030. [6](#), [9](#)
- [64] G. Gompper and M. Schick, Soft Matter, Volume 1: Polymer Melts and Mixtures, *Wiley-VCH*, Weinheim, 2006. [6](#), [16](#), [40](#), [45](#), [49](#), [53](#), [55](#), [66](#), [71](#), [78](#), [79](#)
- [65] J. U. Kim, Y.-B. Yang, and W. B. Lee, Self-Consistent Field Theory of Gaussian Ring Polymers, *Macromolecules* 2012, **45**, 3263-3269. [6](#), [16](#)
- [66] D. Yong and J. U. Kim, Finite volume method for self-consistent field theory of polymers: Material conservation and application, *Phys. Rev. E* 2017, **96**, 063312. [7](#), [14](#), [55](#), [56](#), [57](#), [58](#), [59](#)
- [67] R. B. Thomson, K. Ø. Rasmussen, and T. Lookman, Improved convergence in block copolymer self-consistent field theory by Anderson mixing, *J. Chem. Phys.* 2004, **120**, 31-34. [12](#)
- [68] P. Stasiak and M. W. Matsen, Efficiency of pseudo-spectral algorithms with Anderson mixing for the SCFT of periodic block-copolymer phases, *Eur. Phys. J. E: Soft Matter Biol. Phys.* 2011, **34**, 110. [12](#)
- [69] Y.-B. Yang, S. J. Park, P. Kim, and J. U. Kim, Roles of Chemical Pattern Period and Film Thickness in Directed Self Assembly of Diblock Copolymers, *Soft Matter* 2013, **9**, 5624-5633. [12](#), [14](#)
- [70] M. Sun, P. Wang, F. Qiu, P. Tang, H. Zhang, and Y. Yang, Morphology and phase diagram of ABC linear triblock copolymers: Parallel real-space self-consistent-field-theory simulation, *Phys. Rev. E* 2008, **77**, 016701. [14](#)
- [71] D.-W. Sun, Z.-Y. Sun, H.-F. Li, and L.-J. An, Study of morphology and phase diagram of the H-shaped (AC)B(CA) ternary block copolymers using self-consistent field theory, *Polymer* 2009, **50**, 4270-4280. [14](#)

- [72] Y.-B. Yang, Y. M. Jeon, J. U. Kim, and J. Cho, Diblock and triblock copolymer thin films on a substrate with controlled selectivity, *Eur. Phys. J. E* 2012, **35**, 86. [14](#), [55](#)
- [73] B. Vorselaars, J. U. Kim, T. L. Chantawansri, G. H. Fredrickson, and M. W. Matsen, Self-consistent field theory for diblock copolymers grafted to a sphere, *Soft Matter* 2011, **7**, 5128-5137. [14](#), [40](#), [55](#)
- [74] D. M. Trombly and V. Ganesan, Curvature effects upon interactions of polymer-grafted nanoparticles in chemically identical polymer matrices, *J. Chem. Phys* 2010 **133**, 154904. [16](#), [20](#)
- [75] I. Borukhov and L. Leibler, Enthalpic Stabilization of Brush-Coated Particles in a Polymer Melt, *Macromolecules* 2002, **35**, 5171-5182. [20](#)
- [76] G. G. Vogiatzis and D. N. Theodorou, Structure of Polymer Layers Grafted to Nanoparticles in Silica-Polystyrene Nanocomposites, *Macromolecules* 2013, **46**, 4670-4683. [24](#)
- [77] B. J. Kim, J. Bang, C. J. Hawker, and E. J. Kramer, Effect of Areal Chain Density on the Location of Polymer-Modified Gold Nanoparticles in a Block Copolymer Template, *Macromolecules* 2006, **39**, 4108-4114. [29](#)
- [78] S.-I. Imabayashi, D. Hobara, and T. Kakiuchi, Voltammetric Detection of the Surface Diffusion of Adsorbed Thiolate Molecules in Artificially Phase-Separated Binary Self-Assembled Monolayers on a Au(111) Surface, *Langmuir* 2001, **17**, 2560-2563. [33](#)
- [79] D. Trombly and V. Ganesan, Interactions between Polymer-Grafted Particles and Bare Particles for Biocompatibility Applications, *J. Polym. Sci. B Polym. Phys.* 2009, **47**, 2566-2577. [34](#)
- [80] P. G. de Gennes, Scaling concepts in polymer physics, *Cornell University Press*, Ithaca and London, 1979. [40](#)
- [81] J.-L. Brédas, D. Beljonne, V. Coropceanu, and J. Cornil, Charge-Transfer and Energy-Transfer Processes in π -Conjugated Oligomers and Polymers: A Molecular Picture, *Chem. Rev.* 2004, **104**, 4971-5003. [40](#)
- [82] B. K. Rao and M. L. Verma, First principle study of PEO-AgI polymer systems, *Chem. Phys. Lett.* 2017, **679**, 176-180. [40](#)
- [83] R. O. Agbaoye, P. O. Adebambo, J. O. Akinlami, T. A. Afolabi, S. Zh. Karazhanov, D. Ceresoli, and G. A. Adebayo, Elastic constants and mechanical properties of PEDOT from first principles calculations, *Comput. Mater. Sci.* 2017, **139**, 234-242. [40](#)
- [84] F. W. Starr, T. B. Schröder, and S. C. Glotzer, Molecular Dynamics Simulation of a Polymer Melt with a Nanoscopic Particle, *Macromolecules* 2002, **35**, 4481-4492. [40](#)

- [85] Y. Han and J. Elliott, Molecular dynamics simulations of the elastic properties of polymer/carbon nanotube composites, *Comput. Mater. Sci.* 2007, **39**, 315-323. [40](#)
- [86] Q. Wei, Y. Wang, W. Chai, Y. Zhang, and X. Chen, Molecular dynamics simulation and experimental study of the bonding properties of polymer binders in 3D powder printed hydroxyapatite bioceramic bone scaffolds, *Ceram. Int.* 2017, **43**, 13702-13709. [40](#)
- [87] W. Peng, R. Ranganathan, P. Keblinski, and R. Ozisik, Viscoelastic and Dynamic Properties of Well-Mixed and Phase-Separated Binary Polymer Blends: A Molecular Dynamics Simulation Study, *Macromolecules* 2017, **50**, 6293-6302. [40](#)
- [88] A. C. F. Mendonça, F. Goujon, P. Malfreyt, and D. J. Tildesley, Monte Carlo simulations of the static friction between two grafted polymer brushes, *Phys. Chem. Chem. Phys.* 2016, **18**, 6164-6174. [40](#)
- [89] C. Greco, Y. Jiang, J. Z. Y. Chen, K. Kremer, and K. C. Daoulas, Maier-Saupe model of polymer nematics: Comparing free energies calculated with Self Consistent Field theory and Monte Carlo simulations, *J. Chem. Phys.* 2016, **145**, 184901. [40](#)
- [90] F. S. Bates and G. H. Fredrickson, Block Copolymers—Designer Soft Materials, *Phys. Today* 1999, **52**, 32-38. [40](#)
- [91] M. W. Matsen, The standard Gaussian model for block copolymer melts, *J. Phys.: Condens. Matter* 2002, **14**, R21-R47. [40](#)
- [92] S. F. Edwards, The statistical mechanics of polymers with excluded volume, *Proc. Phys. Soc. London* 1965, **85**, 613-624. [40](#)
- [93] G. H. Fredrickson, The Equilibrium Theory of Inhomogeneous Polymers, *Oxford University Press*, New York, 2006. [40](#), [42](#), [43](#), [45](#), [49](#), [50](#), [53](#), [56](#), [60](#)
- [94] J. U. Kim and M. W. Matsen, Positioning Janus Nanoparticles in Block Copolymer Scaffolds, *Phys. Rev. Lett.* 2009, **102**, 078303. [40](#), [55](#)
- [95] M. W. Matsen and M. Schick, Stable and Unstable of a Diblock Copolymer Melt, *Phys. Rev. Lett.* 1994, **72**, 2660-2663. [40](#), [55](#)
- [96] M. W. Matsen, Effect of Architecture on the Phase Behavior of AB-Type Block Copolymer Melts, *Macromolecules* 2012, **45**, 2161-2165. [40](#)
- [97] S.-M. Park, X. Liang, B. D. Harteneck, T. E. Pick, N. Hiroshiba, Y. Wu, B. A. Helms, and D. L. Olynick, Sub-10 nm Nanofabrication via Nanoimprint Directed Self-Assembly of Block Copolymers, *ACS Nano* 2011, **5**, 8523-8531. [41](#)

- [98] J. W. Jeong, W. I. Park, L.-M. Do, J.-H. Park, T.-H. Kim, G. Chae, and Y. S. Jung, Nanotransfer Printing with sub-10 nm Resolution Realized using Directed Self-Assembl, *Adv. Mater.* 2012, **24**, 3526-3531. [41](#)
- [99] J. G. Son, M. Son, K.-J. Moon, B. H. Lee, J.-M. Myoung, M. S. Strano, M.-H. Ham, and C. A. Ross, Sub-10 nm Graphene Nanoribbon Array Field-Effect Transistors Fabricated by Block Copolymer Lithography, *Adv. Mater.* 2013, **25**, 4723-4728. [41](#)
- [100] I. Y. Erukhimovich, A. Johner, and J. F. Joanny, The ideal polymer chain near planar hard wall beyond the Dirichlet boundary conditions, *Eur. Phys. J. E* 2008, **27**, 435-445. [41](#), [64](#), [70](#)
- [101] M. W. Matsen, J. U. Kim, and A. E. Likhtman, Finite-N effects for ideal polymer chains near a flat impenetrable wall, *Eur. Phys. J. E* 2009, **29**, 107-115. [41](#), [42](#), [45](#), [50](#), [51](#), [59](#), [62](#), [64](#), [70](#)
- [102] S. Blaber, P. Mahmoudi, R. K. W. Spencer, and M. W. Matsen, Effect of chain stiffness on the entropic segregation of chain ends to the surface of a polymer melt, *J. Chem. Phys.* 2019, **150**, 014904. [41](#), [70](#)
- [103] J. M. H. M. Scheutjens and G. J. Fleer, Statistical Theory of the Adsorption of Interacting Chain Molecules. 1. Partition Function, Segment Density Distribution, and Adsorption Isotherms, *J. Phys. Chem.* 1979, **83**, 1619-1635. [41](#), [70](#), [76](#)
- [104] J. M. H. M. Scheutjens and G. J. Fleer, *J. Phys. Chem.* 1980, **84**, 178-190. [41](#), [70](#), [76](#)
- [105] T. Cosgrove, T. Heath, B. van Lent, F. Leermakers, and J. Scheutjens, Configuration of Terminally Attached Chains at the Solid/Solvent Interface: Self-consistent Field Theory and a Monte Carlo Model, *Macromolecules* 1987, **20**, 1692-1696. [41](#)
- [106] G. T. Pickett and A. C. Balazs, Equilibrium Orientation of Confined Diblock Copolymer Films, *Macromolecules* 1997, **30**, 3097-3103. [41](#), [70](#)
- [107] M. Deng, Y. Jiang, H. Liang, and J. Z. Y. Chen, Wormlike Polymer Brush: A Self-Consistent Field Treatment, *Macromolecules* 2010, **43**, 3455-3464. [41](#)
- [108] Y. Jiang and J. Z. Y. Chen, Influence of Chain Rigidity on the Phase Behavior of Wormlike Diblock Copolymers, *Phys. Rev. Lett.* 2013, **110**, 138305. [41](#)
- [109] S. M. Ross, Introduction to Probability Models, *Academic Press*, Amsterdam, 2010. [42](#), [45](#)
- [110] H. Yamakawa, Modern Theory of Polymer Solutions, *Harper & Row*, New York, 1971. [42](#), [45](#)

- [111] A. Y. Grosberg and A. R. Khokhlov, *Statistical Physics of Macromolecules*, AIP Press, New York, 1994. [42](#), [45](#)
- [112] M. W. Matsen and P. Mahmoudi, Segregation of chain ends to the surface of a polymer melt, *Eur. Phys. J. E* 2014, **37**, 78. [42](#), [50](#), [51](#), [70](#), [74](#)
- [113] P. Mahmoudi and M.W. Matsen, Segregation of chain ends to the surface of a polymer melt: Effect of surface profile versus chain discreteness, *Eur. Phys. J. E* 2016, **39**, 78. [42](#), [74](#)
- [114] P. Mahmoudi and M. W. Matsen, Entropic segregation of short polymers to the surface of a polydisperse melt, *Eur. Phys. J. E* 2017, **40**, 85. [42](#), [50](#), [51](#)
- [115] D. Romeis, H. Merlitz, and J.-U Sommer, A new numerical approach to dense polymer brushes and surface instabilities, *J. Chem. Phys.* 2012, **136**, 044903. [42](#)
- [116] M. W. Matsen, Self-Consistent Field Theory for Melts of Low-Molecular-Weight Diblock Copolymer, *Macromolecules* 2012, **45**, 8502-8509. [42](#), [43](#), [50](#), [51](#), [54](#), [56](#), [60](#), [61](#), [62](#), [68](#)
- [117] J. U. Kim, Y.-B Yang, and W. B. Lee, Self-Consistent Field Theory of Gaussian Ring Polymers, *Macromolecules* 2012, **45**, 3263-3269. [50](#)
- [118] E. Helfand, Theory of inhomogeneous polymers: Fundamentals of the Gaussian random-walk model, *J. Chem. Phys.* 1975, **62**, 999-1005. [54](#)
- [119] F. Drolet and G. H. Fredrickson, Combinatorial Screening of Complex Block Copolymer Assembly with Self-Consistent Field Theory, *Phys. Rev. Lett.* 1999, **83**, 4317-4320. [55](#)
- [120] F. Drolet and G. H. Fredrickson, Optimizing Chain Bridging in Complex Block Copolymers, *Macromolecules* 2001, **34**, 5317-5324. [55](#)
- [121] G. H. Fredrickson, V. Ganesan, and F. Drolet, Field-Theoretic Computer Simulation Methods for Polymers and Complex Fluid, *Macromolecules* 2002, **35**, 16-39. [55](#)
- [122] P. Tang, F. Qiu, H. Zhang, and Y. Yang, Phase separation patterns for diblock copolymers on spherical surfaces: A finite volume method, *Phys. Rev. E* 2005, **72**, 016710. [55](#)
- [123] J. F. Li, J. Fan, H. D. Zhang, F. Qiu, P. Tang, and Y. L. Yang, Self-assembled pattern formation of block copolymers on the surface of the sphere using self-consistent field theory, *Eur. Phys. J. E* 2006, **20**, 449-457. [55](#)
- [124] J. U. Kim and M. W. Matsen, Repulsion Exerted on a Spherical Particle by a Polymer Brush, *Macromolecules* 2008, **41**, 246-252. [55](#)
- [125] J. U. Kim and M. W. Matsen, Droplets of structured fluid on a flat substrate, *Soft Matter* 2009, **5**, 2889-2895. [55](#)

- [126] J. Li, H. Zhang, and F. Qiu, Self-consistent field theory of block copolymers on a general curved surface, *Eur. Phys. J. E* 2014, **37**, 18. [55](#)
- [127] K. Ø. Rasmussen and G. Kalosakas, Improved Numerical Algorithm for Exploring Block Copolymer Mesophases, *J. Polym. Sci. B Polym. Phys.* 2002, **40**, 1777-1783. [55](#), [56](#)
- [128] H. D. Ceniceros and G. H. Fredrickson, NUMERICAL SOLUTION OF POLYMER SELF-CONSISTENT FIELD THEORY, *Multiscale Model. Simul.* 2004, **2**, 452-474. [55](#), [56](#)
- [129] E. W. Cochran, C. J. Garcia-Cervera, and G. H. Fredrickson, Stability of the Gyroid Phase in Diblock Copolymers at Strong Segregation, *Macromolecules* 2006, **39**, 2449-2451. [55](#)
- [130] A. Ranjan, J. Qin, and D. C. Morse, Linear Response and Stability of Ordered Phases of Block Copolymer Melts, *Macromolecules* 2008, **41**, 942-954. [55](#)
- [131] P. Stasiak and M. W. Matsen, Efficiency of pseudo-spectral algorithms with Anderson mixing for the SCFT of periodic block-copolymer phases, *Eur. Phys. J. E* 2011, **34**, 110-118. [55](#)
- [132] D. Lee, M.-H. Kim, D. Bae, G. Jeon, M. Kim, J. Kwak, S. J. Park, J. U. Kim, and J. K. Kim, Arrangement of Lamellar Microdomains of Block Copolymer Confined in Hemispherical Cavities Having Two Controlled Interfaces, *Macromolecules* 2014, **47**, 3997-4003. [55](#)
- [133] W. H. Press, B. P. Flannery, S. A. Teukolsky, and W. T. Vetterling, Numerical Recipes: The Art of Scientific Computing, *Cambridge University Press*, Cambridge, 2007. [55](#)
- [134] M. Frigo and S. G. Johnson, The Design and Implementation of FFTW3, *Proceedings of the IEEE* 2005, **93**, 216-231. [56](#), [63](#)
- [135] Y.-B. Yang, S. J. Park, P. Kim, and J. U. Kim, Roles of chemical pattern period and film thickness in directed self-assembly of diblock copolymers, *Soft Matter* 2013, **9**, 5624-5633. [57](#)
- [136] S. Wu, Polymer Interface and Adhesion, *CRC Press*, New York, 1982. [70](#)
- [137] Y. Kim, D. Yong, W. Lee, S. Jo, H. Ahn, J. U. Kim, and D. Y. Ryu, Preferential Wetting Effects on Order-to-Disorder Transition in Polystyrene-b-poly(2-vinylpyridine) Films: A Reconsideration on Thickness Dependence, *Macromolecules* 2018, **51**, 8550-8560. [70](#)
- [138] P. Mansky, T. P. Russell, C. J. Hawker, J. Mays, D. C. Cook, and S. K. Satija, Interfacial Segregation in Disordered Block Copolymers: Effect of Tunable Surface Potentials, *Phys. Rev. Lett.* 1997, **79**, 237-240. [70](#)

- [139] E. Han, K. O. Stuen, M. Leolukman, C.-C. Liu, P. F. Nealey, and P. Gopalan, Perpendicular Orientation of Domains in Cylinder-Forming Block Copolymer Thick Films by Controlled Interfacial Interactions, *Macromolecules* 2009, **42**, 4896-4901. [70](#)
- [140] P. Mansky, Y. Liu, E. Huang, T. P. Russell, and C. Hawker, Controlling Polymer-Surface Interactions with Random Copolymer Brushes, *Science* 1997, **275**, 1458-460. [70](#)
- [141] R. D. Peters, X. M. Yang, T. K. Kim, B. H. Sohn, and P. F. Nealey, Using Self-Assembled Monolayers Exposed to X-rays To Control the Wetting Behavior of Thin Films of Diblock Copolymers, *Langmuir* 2000, **16**, 4625-4631. [70](#)
- [142] J. Y. Kim, B. H. Kim, J. O. Hwang, S.-J. Jeong, D. O. Shin, J. H. Mun, Y. J. Choi, H. M. Jin, and S. O. Kim, Flexible and Transferrable Self-Assembled Nanopatterning on Chemically Modified Graphene, *Adv. Mater.* 2013 **25**, 1331-1335. [70](#)
- [143] G. T. Pickett, T. A. Witten, and S. R. Nagel, Equilibrium Surface Orientation of Lamellae, *Macromolecules* 1993, **26**, 3194-3199. [70](#)
- [144] D. Meng and Q. Wang, Hard-surface effects in polymer self-consistent field calculations, *J. Chem. Phys.* 2007, **126**, 234902. [70](#), [71](#)
- [145] M. W. Matsen, Thin films of block copolymer, *J. Chem. Phys.* 1997, **106**, 7781-7791. [70](#), [71](#)
- [146] T. Geisinger, M. Müller, and K. Binder, Symmetric diblock copolymers in thin films. I. Phase stability in self-consistent field calculations and Monte Carlo simulations, *J. Chem. Phys.* 1999, **111**, 5241-5250. [70](#), [71](#)
- [147] H.-Y. Chen and G. Fredrickson, Morphologies of ABC triblock copolymer thin films, *J. Chem. Phys.* 2002, **116**, 1137-1146. [70](#)
- [148] W. H. Tang, Confinement of Symmetric Diblock Copolymer Thin Films, *Macromolecules* 2000, **33**, 1370-1384. [70](#)
- [149] S.-J. Jeong, H.-S. Moon, J. Shin, B. H. Kim, D. O. Shin, J. Y. Kim, Y.-H. Lee, J. U. Kim, and S. O. Kim, One-Dimensional Metal Nanowire Assembly via Block Copolymer Soft Graphoepitaxy, *Nano Lett.* 2010, **10**, 3500-3505. [71](#)
- [150] K. C. Daoulas, M. Müller, J. J. de Pablo, P. F. Nealey, and G. D. Smith, Morphology of multi-component polymer systems: single chain in mean field simulation studies, *Soft Matter* 2006, **2**, 573-583. [77](#)

-
- [151] B. Steinmüller, M. Müller, K. R. Hambrecht, G. D. Smith, and D. Bedrov, Properties of Random Block Copolymer Morphologies: Molecular Dynamics and Single-Chain-in-Mean-Field Simulations, *Macromolecules* 2012, **45**, 1107-1117. [77](#)
- [152] L. Schneider and M. Müller, Multi-architecture Monte-Carlo (MC) simulation of soft coarse-grained polymeric materials: SOft coarse grained Monte-Carlo Acceleration (SOMA), *Comput. Phys. Commun.* 2019, **235**, 463-476. [77](#)
- [153] A. V. Oppenheim, A. S. Willsky, and S. Hamid, Signals and Systems, *Prentice Hall*, New York, 1996. [87](#)

ACKNOWLEDGEMENTS

[표준새번역] 시 142:5

주님, 내가 주님께 부르짖습니다. “주님은 나의 피난처, 사람 사는 세상에서 내가 받은
분깃은 주님뿐”이라고 하였습니다.

하나님께 감사합니다. 주님이 아니었다면 제힘으로 졸업할 수 없었을 것입니다. 제게
능력 주시는 분 안에서 제가 이 모든 것을 할 수 있었음을 고백합니다.

은혜생수교회 이봉재 목사님, 사모님께 감사드립니다. 박사과정 중 가장 힘들었던 시기
에 은혜생수교회를 찾아가서 그분들을 만난 것은 저의 큰 행운이라 생각합니다. 그분
들은 절망적인 상황 속에서도 늘 하나님만 의지하고 찬양하시는 분들이셨습니다. 함께
했던 시간 동안 그분들을 통해 얼마나 많은 힘과 위로를 얻었는지 모릅니다. 목회자로서
최선을 다해 저를 돌봐주신 덕분에 제가 학업을 포기하지 않을 수 있었습니다. 그 당시
그분들이 보여주신 헌신의 시간들은 절대 헛되지 않다고 생각합니다.

7년간의 박사과정 동안 많은 것을 배울 수 있게 해주신 김재업 교수님께 감사드립니다.
유니스트에서 스승과 제자로 만나 최선을 다해 가르쳐 주셔서 감사드리며 앞으로 더
발전하는 제자가 되겠습니다.

컴퓨터와 관련된 일뿐만 아니라 여러 가지 업무에 많은 도움을 준 용대성 오빠에게
감사합니다. 유능한 연구실 동료 대성 오빠가 없었으면 혼자 많은 시간을 고생했을
것입니다.

저를 낳아주시고 키워주신 어머니, 아버지, 그리고 재정적으로 지원해주시고 기도로
헌신해 주신 시어머니, 시아버지께 감사드립니다.

항상 격려해 주시고 기도로 용기를 주시는 한세로교회 최종인 목사님, 옥명순 사모님
께도 감사합니다.

마지막으로 세상에 하나밖에 없는 나의 남편 고재우에게 감사합니다. 나를 위해 그 누
구보다도 많이 기도해주고 헌신해 주었습니다. 남편이 사랑으로 희생한 일들은 여기에
열거할 수 없을 정도로 많습니다. 하나님께서 짝지어 주신 최고의 동반자와 함께 앞으로
걸어갈 날들이 너무나 기대됩니다. (여보! 여보가 있어서 해낼 수 있었어 사랑해 ♡)

지금까지 저를 인도해 주셨고 앞으로도 인도해 주실 하나님을 영원히 찬양합니다.